

國立交通大學
材料科學及工程學系
博士論文

零維暨一維奈米材料之光電磁特性及結構研究

**Structure Development, Optoelectronic and Magnetic
Characteristics of Zero- and One-Dimensional
Nanoscaled Materials**



研究生: 林士欽

指導教授: 陳三元教授

中華民國九十六年十月

Structure Development, Optoelectronic and Magnetic Characteristics of Zero- and One-Dimensional Nanoscaled Materials

Student: Shihchin Lin

Advisor: Prof. Dr. San-Yuan Chen

Department of Material Science and Engineering

National Chiao Tung University

Abstract

Material with nanometer-scale size have large ratio of surface to bulk atoms. Large surface always gives high active behavior and changes in both physical and chemical properties. Nanomaterials such as nanoparticles, nanotubes, nanorods and nanowires having size generally smaller than 100nm exhibit superior photoelectronic and magnetic properties in various applications. Therefore, in this thesis, the studies will be focused on the synthesis, structure analysis and property characterization of zero-/one dimensional nanoscaled materials.

In chapter 2, ZrO_2 , TiO_2 , ZnO and Al_2O_3 , were chosen as raw materials to synthesize a target for laser ablation. The formed nanoparticles exhibit two kinds of particle size distribution with 7~15 nm (70~90%) and 40~100 nm (10~30%). Nanoparticles synthesized at lower fluence laser ablation are rich in Zn composition and show more narrow distribution. While increasing laser fluence, the composition of the collected nanoparticles is primarily composed of Zr. A model based on composition and morphology of both nanoparticles and target with changing laser fluence was proposed to explain the phase evolution of nanoparticles. The average far-infrared emissivity of the nanoparticles based on $ZrTiO_4$ -- $ZnAl_2O_4$ system is measured to be more than 80 % (wavelength range from 4 to 12 μm) and varies with crystal phase ratio.

In chapter 3, a highly dispersed nano- TiO_2/Ag catalyst is synthesized in an

alkaline solution. Nearly all of the dimethy-blue target pollutant at high concentration was removed when the photoreaction was performed in a short period. This novel nano TiO₂ photocatalyst exhibits excellent photocatalytic activity because it is well dispersed. Since no dispersant or organic binder was used, this synthetic process has the advantages of low cost and convenience.

In chapter 4, One-dimensional nanotube arrays of nickel-phosphate have been developed by electroless deposition into sub-micro to nanometer sized pores of the porous alumina templates. The dimension of the formed nanotubes has 1 μm in length, 200~300nm in diameter and 80~150nm in thickness of tube walls. Transmission electron microscopy examination of the nanotubes clearly show amorphous hallow structure with a average grain size of ~5 nm. The hysteresis loops of the nanotube arrays show a coercive field of about 200Oe under treatment in 95%N₂/5%H₂ atmosphere at 500 °C as the magnetic field was applied along parallel and perpendicular to tube axis. The nanotube arrays also exhibit an anisotropic magnetic property with easier saturation along the perpendicular direction. However, both coercive field and saturation of remanent magnetization of the nanotube arrays become lower while continually increasing heat treatment temperature up to 900°C.

In chapter 5, ordered silver- nickel core-shell nanowire arrays were successfully fabricated by electrodeposition. The ordered silver nanowire arrays embedded in a porous alumina template were first fabricated from an aqueous solution of Ag(NO₃)₂ and Ac(NH₃). After removing out the template, the obtained silver nanowire arrays were subsequently electrodeposited with nickel at 1.6~2.6V and 60°C using the electrolyte composed of NiSO₄, NiCl₂ and H₃BO₃. Transmission electron microscopy (TEM) observation reveals that a 15 nm thick nickel film was coated on the surface of the silver nanowires with about 200 nm in diameter. It was found that the silver nanowires with nickel coating showed enhanced magnetic properties in comparison to

that of pure silver nanowires. The Magnetic Force Microscope (MFM) image of silver-nickel core-shell nanowires exhibits magnetic domain state. In addition, the hysteresis loops of the silver-nickel nanowire arrays show a coercive field of 180Oe, almost independent of the applied magnetic field parallel and perpendicular to nanowires. However, it was observed that a larger magnetic domain was found in parallel direction than that in perpendicular direction.

In chapter 6, a single bath electrodeposition method was developed to integrate nanowires of Ag/Co with multi-layer structures within a commercial AAO (anodic alumina oxide) template, with a pore diameter 100~200 nm. An electrolyte system containing silver nitrate and cobalt sulfate was explored by using cyclic-voltammetry and electrodeposition rate to optimize electrodeposition conditions. A designed step-wise potential and different cations ratio $[Co^{2+}] / [Ag^+]$ were adopted for the electrodeposition. After dissolution by NaOH, Ag/Co multilayered nanowires were obtained with a composition $\{[Co]/[Ag_{80}Co_{20}]\}_{30}$ identified by XRD and TEM when $[Co^{2+}] / [Ag^+] = 150$. By annealing at 200°C for 1hr, the uniformly structured $\{Co_{99.57}/Ag_{100}\}_{30}$ nanowires were obtained. Compared with pure Co nanowire, the magnetic hysteresis loops showed manifest magnetic anisotropy for $\{Co_{99.57}/Ag_{100}\}_{30}$ nanowires than that of pure Co nanowires corresponding to a change of easy axis upon magnetization.

In chapter 7, The heterojunction photovoltaic devices consist of hybrid p-type organic Cu-phthalocyanine and inorganic n-type semiconductor ZnO nanostructures which include vertically aligned nanorods, randomly oriented nanorods and nanoparticles. The strong absorption of ZnO appears in 250~460nm wavelength and Cu-phthalocyanine exhibits broad absorption in 440-700nm with an absorption maximum at 630nm. The incorporation of partial Al into ZnO leads to the shift of

absorb light from UV region to visible light and subsequently causes more charge generation. Charge recombination from hybrid devices of vertically aligned ZnO nanorods was more efficient than that fabricated from the other types. The maximum incident photon to electron conversion and energy conversion efficiencies under simulated sunlight AM1.5 ($10\text{mW}/\text{cm}^2$) in aligned ZnO are 0.036mA and 1.32% , respectively.

In chapter 8, a new 1 and 2 dimension nano structure for making solar cell or TFT module have been researched by adopting low cost coated glass substrate with polysilicon instead of silicon wafer. Meanwhile, laser annealing is used as the unique method to melt primal amorphous silicon thin film and promote it recrystallize under low temperature. Particularly, the new thermal conducting layers are patterned under the silicon layer to enhance the lateral giant grain growth. The important processes are represented as follows: 1. A electrical conducting layer are formed on the glass substrate. 2. Photolithographic process is executed to pattern the thermal conducting layer and form many variable thermal conducting zone. 3. An about 200nm amorphous silicon film is formed on the patterned thermal conductive layer. 4. A thermal isolation layer such as SiO_2 is deposited for keeping laser annealing temperature. 5. While the pulse excimer laser is injected the structure, the amorphous silicon film can absorb laser energy instantaneously and transform it to crystalline type. Moreover, the temperature gradient could be generated on the silicon layer and cause the uniform polysilicon growth of $1\sim 2\mu\text{m}$ giant grains under about $450\text{-}475\text{mJ}/\text{cm}^2$ laser fluence. A unique method of multiple laser fluence have been executed to increase the crystalline orientation of Si(111).

零維暨一維奈米材料之光電磁特性及結構研究

學生:林士欽

指導教授:陳三元教授

國立交通大學 材料科學及工程學系

摘要

奈米所具有之量子尺寸效應、表面界面效應等特殊現象，使奈米之光電材料展現微米顆粒所不及之光電及催化特性，因顆粒尺寸減少時，對於紫外光之吸收產生藍移現象，使能隙擴大，並產生更大之氧化還原電位；此外，而粒徑減少時表面積增大，促進光電轉換，且吸附待分解物之能力增強，使光催化分解之效率亦隨之增加；另外，尺寸減少時，光激發而形成之電子電洞對擴散至表面的時間愈短，電子與電洞分離之效果愈好，進而提升光電效率。在奈米磁性材料之研究方面，高深寬比的奈米磁導線，因為可以磁操控的關係所以可以將高深寬比的銀鈷導線拉直，就因為如此可將此種導線，有高的導電異向性，因此可應用在超細間距異向性導電膜為高密度磁記憶體及覆晶構裝重要材料。本文用bottom-up之方法製作零維奈米結構(如金屬和半導體奈米粒子及自聚核/殼奈米粒子)及一維奈米結構(如奈米管、奈米線、奈米棒)，擁有許多新穎之特性及做為電子、磁性、光學及化學性質之應用。一方面研究其製程之穩定性及發展性，另一方面也發展其奈米特性進一步發展組裝新穎功能奈米材料的能力。進一步考量各重要材料介面(如金屬—半導體，有機—無機等)後衍伸出來各種豐富的功能性，將可能使許多發展中的奈米科學及科技應用產生巨大的改變，主要應用於太陽電池、光觸媒、遠紅外線放射及磁性元件等。

第二章以多組分之 ZrO_2 , TiO_2 , ZnO and Al_2O_3 為起始原料，利用雷射剝離法製作複晶相遠紅外線奈米材料。包括雷射劑量與氣氛等製程參數將影響生成之微粉大小、形態與組成。形成之複晶相奈米材料之粒徑分布成雙峰分布，約7~15 nm (70~80%) and 40~100 nm (20~30%)。於低雷射劑量時有Zn組成富集且粒徑分布窄化之趨勢，而隨雷射劑量增加，Zr組成亦隨之增加。而靶材之結構演變、及劑量為控制奈米材料演化之重要因子。

第三章以液相電位分散及金屬鹽類還原之方法合成 TiO_2 於奈米級貴重金屬樹枝狀結構之微粒上，形成全時效型光觸媒。研究結果顯示以金屬鹽類還原法較光照還原法形成貴重金屬樹枝狀結構之微粒，再利用負電位控制奈米 TiO_2 於奈米級貴重金屬樹枝狀結構之微粒上為佳。針對滅菌能力、空氣及液相污染物的降解能力來評估全時效型光觸媒的去除效能，以結合分散良好之 10 奈米 TiO_2 左右之奈米貴重金屬與光觸媒載體效能最佳，隨奈米金屬粒徑增加而降低其去除效能。而對次甲基藍分解效率亦可分別達到 99% 以上。

第四章使用次微米至奈米級孔洞的氧化鋁模板，以含 NiSO_4 , NaH_2PO_2 , $\text{NaC}_2\text{H}_3\text{O}_2$ and $\text{Na}_3\text{C}_6\text{H}_5\text{O}_7$ 之亞磷酸鹽電解質溶液，在 $80 - 100^\circ\text{C}$ 與 $\text{pH} = 3 - 6$ 條件下合成磷酸鎳奈米管陣列。奈米管具有 $1\mu\text{m}$ 長度、 $200-300\text{nm}$ 直徑與 $80-150\text{nm}$ 管壁厚度。穿透式電子顯微鏡顯示奈米管由約 5nm 的粒子所組成。經 $95\% \text{N}_2 / 5\% \text{H}_2$ 氣氛與 500°C 溫度處理，奈米管陣列有 $2000e$ 的矯頑磁場與垂直奈米管方向易磁化的磁異方性。隨處理溫度升高至 900°C ，矯頑場與飽和磁化呈下降趨勢。

第五、六章以奈米模板(Nano template)陽極處理氧化鋁為基礎，使用電鍍生成奈米銀線陣列的方式，電鍍鈷奈米線後，因鈷金屬可帶有磁效應，利用的此性質即可製做出可以磁操控。在導電性上，可保有部分銀線的導電奈米導線，並且以 AAO 當過模板的作法，可製造出高深寬比的奈米導線，因為可以磁操控的關係所以可以將高深寬比的銀鈷導線拉直，就因為如此可將此種導線，有高的導電異向性，因此可應用在超細間距異向性導電膜，為高密度磁記憶體及覆晶構裝重要材料。規則的銀、銀/鎳、銀/鈷陣列利用脈衝電化學沉積在多孔的氧化鋁模板從一個水溶性 $\text{Ag}(\text{NO}_3)_2$ 和 $\text{Ac}(\text{NH}_3)$ 電鍍液中製作，移出模板，銀、銀/鎳、銀/鈷奈米線陣列在 $1.6-2.6\text{V}$ 和 $40-90^\circ\text{C}$ 之條件使用，將 CoSO_4 , NiSO_4 , NiCl_2 和 H_3BO_3 電鍍液，以形成殼核或多層之結構。 15nm 鎳薄膜匹覆在直徑 200nm 之銀奈米線上，形成殼核結構，依據 TEM 之結果顯示它是被發現已被鎳金屬匹覆之銀奈米線之的磁性性質與傳統的純銀線相互比較其磁性性質能被加強。從磁力顯微鏡影像是被觀察到銀-鎳核殼奈米線之 domain 狀態。另外，銀-鎳奈米線顯示

1800e 之矯頑磁場，施加磁場平行與垂直至奈米線幾乎是獨立的。無論如何，鎳層能產生一個較大磁 domain 是被發現，變成平行方向超越垂直方向。

第七章以 N 型氧化鋅奈米線陣列與 P 型有機光電轉換材料結合，形成混成太陽電池元件，以鋁摻雜之方式，使氧化鋅奈米線陣列對光之吸收峰往可見光部分偏移，增加其對可見光之吸收率，並使元見之光電轉換效率、光電流和填充因子有所提昇。

第八章利用新的一維及二維奈米結構為做太陽能電池或 TFT 模組，通過採取便宜的鍍膜的玻璃基板，研究了於其上成長之多晶矽取代矽基板。同時，利用雷射退火，快速熔融最初玻璃基板的矽薄膜和促進它的獨特的方法在低溫之下再結晶，特別使用熱傳導層使之促進巨晶多晶矽之生長。重要製程如下：1. 電子傳導層在玻璃基體形成。2. 黃光微影過程被形成，造成許多熱導變化的熱傳導區域。3. 200nm 非晶矽薄膜形成熱導層數之上。4. 保溫層如 SiO₂ 為保留雷射退火溫度於矽薄膜之上形成。5. 當雷射脈衝(excimer laser)入射此結構時，非晶矽薄膜可瞬間地吸收激光能和變換成結晶型。而且，利用溫度差及非晶矽對於 234nm 波段對於雷射波段之吸收作用，於 450-475mJ//cm² 雷射脈衝之下，在非晶矽薄膜層能引起和大約導致 1~2 μ m 巨大之多晶矽成長，而利用另一種複合雷射劑量的方法，將可以增加 Si (111) 順向優選排列取向。

Acknowledgments

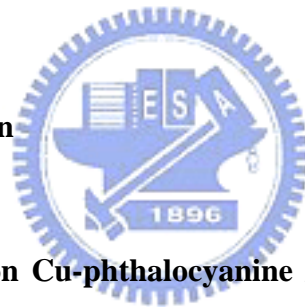
I deeply appreciate to my supervisor professor Dr. San-Yuan Chen for his all-out supports. He is not only a benevolent advisor but also a very erudite philosopher. I also sincerely thank Dr. Syh-Yuh Cheng of the Industry Technology Research Institution for his warmhearted help in my thesis work. Moreover, I am grateful to Prof. Dr. Hong-Wen Wang, Dr. Pang Lin and Dr. Tien-Mo Liu for giving me much suggestion to my thesis content. Therefore, I would like to thank my colleagues in MCL and school. Finally, I want to thank my family and friends for their selfless supports and encouragement during my study period.



Contents

Abstract	I
Abstract(Chinese)	V
Acknowledgments	IX
Contents	X
1 Introduction	1
1.1 Strategies for one dimensional nanostructure growth	3
1.2 Negative template methods	4
1.3 Applications of the nanowires	5
1.4 Reference	15
2 Characterization and Composition Evolution of Multiple-Phase Nanoscaled Ceramic Powder by Laser Ablation	21
2.1 Introduction	21
2.2 Experimental	22
2.3 Results and discussion	22
2.4. Summary	26
3 Nanoscaled TiO₂/Ag catalyst and photodecomposition characteristic	34
3.1 Introduction	34
3.2 Experimental	34
3.3 Results and discussion	36
3.4. Summary	39
4 Synthesis and magnetic properties of highly arrayed nickel-phosphate nanotubes	48
4.1 Introduction	48

4.2 Experimental	49
4.3 Results and discussion	49
4.4. Summary	52
5 Electrochemical fabrication and magnetic properties of highly ordered silver-nickel core-shell nanowires	60
3.1 Introduction	60
3.2 Experimental	61
5.3 Results and discussion	62
5.4. Summary	66
6 Synthesis of Ag/Co magnetic nanowires with multi-layered structure	73
6.1 Introduction	74
6.2 Experimental	75
6.3 Results and discussion	76
6.4. Summary	78
7 Solar cell devices based on Cu-phthalocyanine / nanostructured ZnO hybrid film	91
7.1 Introduction	91
7.2 Experimental	92
7.3 Results and discussion	93
7.4. Summary	96
8.1and 2 Dimention Nano Structure Design and Giant-Grain Orientated Polysilicon Study at Low Temperature.....	102
8.1 Introduction	102
8.2 Experimental	103
8.3 Results and discussion	103
8.4. Summary	106



9 Conclusion

115

10.Publication list

118





Chapter 1

Introduction

Particles with nanometer-scale size have large ratio of surface to bulk atoms. Large surface always gives high active behavior and changes both physical and chemical properties. Inorganic nanoparticles having size generally smaller than 100nm provide superior properties for various applications and become important topic in nanomaterials.

Many methods are developed to prepare inorganic nanoparticles during recent year. Chemical route includes metal-organic compounds the so-called precursors and reaction through hydrolysis, condensation, catalysis, pyrolysis, etc . Evaporation-condensation is mainly the process in physical route and laser ablation is the important method included in this route.[2-5] The far-infrared ray emissivity and photodecomposition characterization of nanoparticles based on oxide system was deeply investigated recently.

Moreover, magnetic film and nanowires have been the most interesting and intensely investigated fields of material in recent year . The fabrication of magnetic metal arrays has not only the fundamental worth in these materials but also their potential utilization in magnetic recording. For high density storage media, one single nanosized pattern, ordered nanodots or nanotubes is a single domain structure and denotes one bit signal. Magnetic period nano-structure arrays as an ultra-high-density magnetic storage can achieve recording densities of more than 100Gbit/in², which is more than the continuous magnetic film of 40Gbit/in². Arrays of ferromagnetic nonodots, nanowires or nanotubes may be fabricated by several methods such as e-beam lithography, imprint technology or template. The porous template can be considered as one quicker and cheaper method to prepare highly perpendicular magnetic anisotropy structure because AAO(anode alumina oxide) has high oriented porous structure with uniform and nearly parallel pores that can be organized the pseudo ordered nanowire or nanotube arrays. Such


structure also shows high magnetic anisotropy phenomena with the shape axis parallel to the nanowire arrays.

On the other hand, it is well known that transition metals such as Fe, Co, Ni and their alloy have higher saturation magnetization as well as Curie temperature, and lower crystalline anisotropy. Furthermore, magnetic properties are strongly influenced by the dimension and crystal properties, which also depend on the physical structure of templates and growth mechanism of wires or tubes. Recently, magnetic properties of nickel nanowires have been investigated by several groups because nickel nanowires show important applications in magnetic recording.

Organic-inorganic hybrids for photovoltaic cell have been receiving attention recently. It has become the major purposes to enhance the conversion efficiency of the photovoltaic devices and at same time to reduce production costs. Semiconductor oxide materials in conjunction with photo sensitive organic dyes have extended hybrid materials sensitivity into the visible regions. ZnO is a semiconductor material and possesses special characteristic including high electron mobility, low temperature synthesis, and the potential for controlling the morphology through simple solution processing. In the past few years, hybrid devices including ZnO/ZnPc, ZnO/merocyanines, ZnO/P3HT and ZnO/CuPcetc, have been constantly investigated. The obtained hybrid ZnO/ dye devices have an overall efficiency of approximately 0.2-2% and fill factor of greater than 0.3-0.6 and 5~16% of the external quantum efficiency that could be attributed to the increased ZnO /dye interfacial area due to recombination behaviors of high surface ZnO structure. However, the conversion efficiency of these devices have been limited because of difficultly controllable particle boundary, inorganic/dye degradation and high production costs. In recent years, ZnO nanorods or nanowires uniformly grown perpendicular to the substrate are particularly investigated because of slow charge recombination between aligned nanowires and dyes that results in significant improvements in device performance.

1.1 Strategies for one dimensional nanostructure growth

One dimensional nanostructure with different levels of control over these parameters. Figure 1 schematically illustrates some of these synthetic strategies that include: (1) use of the intrinsically anisotropic crystallographic structure of a solid to accomplish one dimensional growth (Fig. 1.1.A); (2) introduction of a liquid-solid interface to reduce the symmetry of a seed (Fig. 1.1.B); (3) use of various templates with one dimensional morphologies to direct the information of one dimensional nanostructure (Fig. 1.1.C); (4) use of supersaturation control to modify the growth habit of a seed; (5) use of appropriate capping reagent to kinetically control the growth rates of various facets of a seed (Fig. 1.1.D); (6) self-assembly of zero dimensional nanostructures (Fig. 1.1.E); (7) size reduction of one dimensional microstructure (Fig. 1.1.F). Because many of these methods were not demonstrated until very recently, most of their characteristics are only vaguely known.



One-dimensional nanomaterials based on template synthesis have attracted much research interest. Porous alumina membranes are widely used as templates for fabricating one-dimensional nanostructures, including metals, semiconductors, carbon, and conductive polymers. However, the alumina membrane itself has several disadvantages, such as insufficient chemical stability and low mechanical strength. It is therefore difficult to use alumina membranes for the synthesis of nanowires and nanotubes under severe reaction conditions such as in strong acid and alkali solutions. To overcome these disadvantages, a two-step replication process was developed. Although this has resulted in the successful fabrication of nanoporous replicated films, there are still some disadvantages. Usually, it is very hard to achieve full replication of the alumina membrane, thus resulting in poor aspect ratio (typically less than 100) of the replicated films. Moreover, the methyl methacrylate (MMA) monomer, which is used as the replication medium, is injected into the pores under vacuum conditions. Thus the replication process is complicated and this makes it difficult to be applied widely in industrial

manufacturing processes in Fig. 1.2. A widely used approach to fabricate metal nanowires is based on various templates, which include negative, positive, and surface step templates. We discuss each of the approaches below.

1.2 Negative template methods

Negative template methods use prefabricated cylindrical nanopores in a solid material as templates. By depositing metals into the nanopores, nanowires with a diameter predetermined by the diameter of the nanopores are fabricated. There are several ways to fill the nanopores with metals or other materials to form nanowires, but the electrochemical method is a general and versatile method. If one dissolves away the host solid material, free-standing nanowires are obtained. This method may be regarded as a “brute-force” method because the diameter of the nanowires is determined by the geometrical constraint of the pores rather than by elegant chemical principles. However, it is one of the most successful methods to fabricate various nanowires that are difficult to form by conventional lithographic process. Fabrication of suitable templates is clearly a critical first step. To date, a number of methods have been developed to fabricate various negative templates. Examples include alumina membranes, polycarbonate membranes, mica sheets, and diblock polymer materials. These materials contain a large number of straight cylindrical nanopores with a narrow distribution in the diameters of the nanopores.

Anodic porous alumina is commonly used negative template. The nanopores in the template are formed by anodizing aluminum films in an acidic electrolyte. The individual nanopores in the alumina can be ordered into a close-packed honeycomb structure (Fig. 1.3). The diameter of each pore and the separation between two adjacent pores can be controlled by changing the anodization conditions. The fabrication method of anodic porous alumina can be traced back to the work done in the 1950's, which involves a one-step anodization process. This original one-step anodization method is still used to fabricate most commercial alumina membranes [1.1, 1.2]. The anodic porous alumina has a much higher pore density ($\sim 10^{11}$ pores/cm²), which allows one to fabricate a large number of nanowires at one time. Another interesting feature of the

porous alumina template is that the chemistry of the pore walls can be altered via reaction with silane compounds [1.3]. The distribution of nanopores in anodic porous alumina is usually not as perfect as the one shown in Figure 1.3. To achieve highly ordered pores, high-purity aluminum films (99.999%) are used. In addition, they are first preannealed to remove mechanical stress and enhance the grain size. Subsequently, the films are electropolished in a 4:4:2 (by weight) mixture of H_3PO_4 , H_2SO_4 , and H_2O to create homogeneous surfaces. Without the preannealing and electropolishing steps, it is hard to form well-ordered pores [1.4]. The order of the pores depends also on other anodization conditions, such as anodization voltage and electrolyte. It has been reported that anodization over a long period at an appropriate constant voltage can produce an almost ideal honeycomb structure over an area of several μm [1.4, 1.5]. The optimal voltage depends on the electrolyte used for the anodization. For example, the optimal voltage for long-range ordering is 25 V in sulfuric acid, 40 V in oxalic acid, and 195 V in phosphoric acid electrolyte, respectively [1.4]. The diameter and depth of each pore, as well as the spacing between adjacent pores can be also controlled by the anodizing conditions. Both the pore diameter and the pore spacing are proportional to the anodizing voltage with proportional constants of 1.29 nm V^{-1} and 2.5 nm V^{-1} , respectively. The dependence of the diameter and the spacing on the voltage is not sensitive to the electrolyte, which is quite different from the optimal voltage for ordered distribution of the pores as discussed above [1.6,1.7]. This property has been exploited to make size-selective microfiltration membranes and to control the diameter of nanowires formed in the pores. By properly controlling the anodization voltage and choosing the electrolyte, one can make highly ordered nanopores in alumina with desired pore diameter and spacing. The order of the pores achieved by anodizing an aluminum film over a long period is often limited to a domain of several μm . The individual ordered domains are separated by regions of defects. Recently, a novel approach has been reported to produce a nearly ideal hexagonal nanopore array that can extend over several millimeters [1.8, 1.9]. The approach uses a pretexturing process of Al in which an array of shallow concave features is initially formed on

Al by indentation. These concave features serve as nucleation sites for the formation of pores during the initial stage of anodization. The pore spacing can be controlled by the pretextured pattern and the applied voltage. Another widely used method to create highly ordered nanopore arrays is a two-step anodization method [1.10,1.11]. The first step involves a long-period anodization of high purity aluminum to form a porous alumina layer. Subsequent dissolution of the porous alumina layer leads to a patterned aluminum substrate with an ordered array of concaves formed during the first anodization process. The ordered concaves serve as the initial sites to form a highly ordered nanopore array in a second anodization step. Acidic anodization of Al normally results in a porous alumina structure which is separated from the aluminum substrate with a so-called barrier layer of Al_2O_3 . The barrier layer and aluminum substrate can be removed to form a free-standing porous alumina membrane. The aluminum can be removed with saturated HgCl_2 and the barrier layer of Al_2O_3 with a saturated solution of KOH in ethylene glycol. An alternative strategy to separate the porous alumina from the substrate is to take advantage of the dependence of pore diameter on anodization voltage. By repeatedly decreasing the anodization voltage several times at 5% increments, the barrier layer becomes a tree-root-like network with fine pores. Since the root-like network has a higher exposed surface area than the primary large pores, dissolution occurs there first when immersing the sample in a concentrated acid. The dissolution of the network then results in the separation of the porous oxide film from the aluminum substrate.

Fabrication of Metal Nanowires Using the membrane templates previously described, nanowires of various metals, semiconductors and conducting polymers [1.12], have been fabricated. These nanostructures can be deposited into the pores by either electrochemical deposition or other methods, such as chemical vapor deposition (CVD) [1.13], chemical polymerization, electroless deposition [1.14], or by sol-gel chemistry. Electrodeposition is one of the most widely used methods to fill conducting materials into the nanopores to form continuous nanowires with large aspect ratios. One of the great advantages of the

electrodeposition method is the ability to create highly conductive nanowires. This is because electrodeposition relies on electron transfer, which is the fastest along the highest conductive path. Structural analysis showed that the electrodeposited nanowires tend to be dense, continuous, and highly crystalline in contrast to other deposition methods, such as CVD. Yi and Schwarzacher demonstrated that the crystallinity of superconducting Pb nanowires can be controlled by applying a potential pulse with appropriate parameters [1.15]. The electrodeposition method is not limited to nanowires of pure elements. It can fabricate nanowires of metal alloys with good control over stoichiometry. For example, by adjusting the current density and solution composition, Huang et al. controlled the compositions of CoPt and FePt nanowires to 50:50 in order to obtain the high anisotropic face-centered tetragonal phases [1.16]. Similar strategies have been used in other magnetic nanowires [1.17,1.18] and in thermoelectronic nanowires [1.19]. Another important advantage of the electrodeposition method is the ability to control the aspect ratio of the metal nanowires by monitoring the total amount of passed charge. This is important for many applications. For example, the optical properties of nanowires are critically dependant on the aspect ratio [1.20]. Nanowires with multiple segments of different metals in a controlled sequence can also be fabricated by controlling the potential in a solution containing different metal ions [1.21]. Electrodeposition often requires one to deposit a metal film on one side of the freestanding membrane to serve as a working electrode on which electrodeposition takes place. In the case of large pore sizes, the metal film has to be rather thick to completely seal the pores on one side. The opposite side of the membrane is exposed to an electrodeposition solution, which fills up the pores and allows metal ions to reach the metal film. However, one can avoid using the metal film on the backside by using anodic alumina templates with the natural supporting Al substrate. The use of the supported templates also prevents one from breaking the fragile membrane during handling. However, it requires one to use AC electrodeposition [1.22]. This is because of the rather thick barrier layer between the nanopore membrane and the Al substrate. Detailed studies of the electrochemical fabrication process

nanowires have been carried out by a number of groups [1.23]. The time dependence of the current curves recorded during the electrodeposition process reveal three typical stages. Stage I corresponds to the electrodeposition of metal into the pores until they are filled up to the top surface of the membrane. In this stage, the steady-state current at a fixed potential is directly proportional to the metal film area that is in contact with the solution, as found in the electrodeposition on bulk electrodes. However, the electrodeposition is confined within the narrow pores, which has a profound effect on the diffusion process of the metal ions from the bulk solution into the pores before reaching the metal film. The concentration profiles of Co ions in the nanopores of polycarbonate membranes during electrodeposition of Co have been studied by Valizadeh et al. [1.24]. After the pores are filled up with deposited metal, metal grows out of the pores and forms hemispherical caps on the membrane surface. This region is called stage II. Since the effective electrode area increases rapidly during this stage, the electrochemical current increases rapidly. When the hemispherical caps coalesce into a continuous film, stage III starts, which is characterized by a constant value again. By stopping the electrodeposition process before stage I ends, an array of nanowires filled in the pores is formed. The current-time curves are not always as well behaved as the one described above [1.25]. For example, the current may vary during the first stage, so that stages I, II, and III may merge together and become difficult to separate. One plausible explanation of this observation is that the pores in the membranes are not aligned parallel but have a considerable angular distribution ($\pm 34^\circ$). The angular distribution means a large length distribution of the pores, such that the pores with different lengths fill up with nanowires at different times. Another possible reason is inhomogeneous growth rates in different pores, due to different degrees of wetting of different pores. The wetting problem tends to be more severe for membranes with smaller pores because of the increased difficulty to wet all the pores before electrodeposition. One way to reduce the wetting problem is to treat polycarbonate membranes with polyvinylpyrrolidone (PVP) [1.25]. Adding ethanol or methanol into the electrolyte is also found to reduce the wetting problem

[1.26]. Another method is to perform the electrodeposition in an ultrasound bath to facilitate the mass transport of ions through the pores of the membrane [1.27].

1.3 Applications of the nanowires

Metal nanowires are promising materials for many novel applications, ranging from chemical and biological sensors to optical and electronic devices. This is not only because of their unique geometry, but also because they possess many unique physical properties, including electrical, magnetic, optical, as well as mechanical properties. While most efforts to date have focused on developing better methods to fabricate the nanowires and on characterizing the various properties, applications are becoming an important area of research and development. Some of the applications are discussed below.

1.3.1. Magnetic Materials and Devices

The electrodeposition methods described above have been used to fabricate magnetic nanowires of a single metal [1.28], multiple metals in segments [1.29], as well as alloys [1.30]. Since the pioneering works nearly a decade ago, much progress has been made in understanding the magnetic properties of the nanowires [1.31]. A recent review provides a detailed description of the properties [163]. For magnetic nanowires (Fe, Co, and Ni) with relative large aspect ratios (e.g., >50), they exhibit an easy axis along the wires. An important parameter that describes magnetic properties of materials is the remanence ratio, which measures the remanence magnetization after switching off the external magnetic field. The remanence ratios of the Fe, Co, and Ni nanowires can be larger than 0.9 along the wires and much smaller in the perpendicular direction of the wires. This finding clearly shows that the shape anisotropy plays an important role in the magnetism of the nanowires. Another important parameter that describes the magnetic properties is coercivity, which is the coercive field required to demagnetize the magnet after full magnetization. The magnetic nanowires exhibit greatly enhanced magnetic coercivity [1.32, 1.33]. In addition, the coercivity depends on the wire diameter and the aspect ratio, which shows that it is possible to control the magnetic properties of the nanowires by controlling the

fabrication parameters. The diameter dependence of the coercivity reflects a change of the magnetization reversal mechanism from localized quasi-coherent nucleation for small diameters to a localized curling like nucleation as the diameter exceeds a critical value [1.34]. Another technically important novel property observed in the magnetic nanowires is giant magnetoresistance (GMR) [1.29]. For example, Evans et al. have studied Co-Ni-Cu/Cu multilayered nanowires and found a magnetoresistance ratio of 55% at room temperature and 115% at 77K for current perpendicular to the plane (along the direction of the wires) [1.35]. Giant magnetoresistance has also been observed in semimetallic Bi nanowires fabricated by electrodeposition [1.36]. Hong et al. have studied GMR of Bi with diameters between 200 nm and $2\mu\text{m}$ in magnetic fields up to 55T and found that the magnetoresistance ratio is between 600–800% for magnetic field perpendicular to the wires and ~200% for the field parallel to the wires [1.37]. The novel properties and small dimensions have potential applications in the miniaturization of magnetic sensors and the high-density magnetic storage devices. The alignment of magnetic nanowires in an applied magnetic field can be used to assemble the individual nanowires [1.38]. Tanase et al. studied the response of Ni nanowires in response to magnetic field [1.39]. The nanowires are fabricated by electrodeposition using alumina templates and functionalized with luminescent porphyrins so that they can be visualized with a video microscope. In viscous solvents, magnetic fields can be used to orient the nanowires. In mobile solvents, the nanowires form chains in a head-to-tail configuration when a small magnetic field is applied. In addition, they demonstrated that three-segment Pt-Ni-Pt nanowires can be trapped between lithographically patterned magnetic microelectrodes [1.40]. The technique has a potential application in the fabrication and measurement of nanoscale magnetic devices.

1.3.2. Optical Applications

Dickson and Lyon studied surface plasmon (collective excitation of conduction electrons) propagation along 20 nm diameter Au, Ag, and bimetallic Au-Ag nanowires with a sharp Au/Ag heterojunction over a distance of tens of μm [1.41]. The plasmons are excited by focusing a laser

with a high numerical aperture microscope objective, which propagate along a nanowire and reemerge as light at the other end of the nanowire via plasmon scattering. The propagation depends strongly on the wavelength of the incident laser light and the composition of the nanowire. At the wavelength of 820 nm, the plasmon can propagate in both Au and Ag nanowires, although the efficiency in Ag is much higher than that in Au. In the case of bimetallic nanowire, light emission is clearly observed from the Ag end of the nanowire when the Au end is illuminated at 820 nm. In sharp contrast, if the same bimetallic rod is excited at 820 nm via the Ag end, no light is emitted from the distal Au end. The observation suggests that the plasmon mode excited at 820 nm is able to couple from the Au portion into the Ag portion with high efficiency, but not from the Ag portion into Au. The unidirectional propagation has been explained using a simple two-level potential model. Since surface plasmons propagate much more efficiently in Ag than in Au, the Au→Ag boundary is largely transmissive, thus enabling efficient plasmon propagation in this direction. In the opposite direction, however, propagation from Ag to Au gains a much steeper potential wall, allowing less optical energy to couple through to the distal end. Their experiments suggest that one can initiate and control the flow of optically encoded information with nanometer-scale accuracy over distances of many microns, which may find applications in future high-density optical computing.

1.3.3. Biological Assays

We have mentioned that by sequentially depositing different metals into the nanopores, multisegment or striped metal nanowires can be fabricated [1.27]. The length of each segment can be controlled by the charge passed in each plating step and the sequence of the multiple segments is determined by the sequence of the plating steps. Due to the different chemical reactivities of the “stripe” metals, these stripes can be modified with appropriate molecules. For example, Au binds strongly to thiols and Pt has high affinity to isocyanides. Interactions between complementary molecules on specific strips of the nanowires allow different nanowires to bind to each other and form patterns on planar surfaces. Using this strategy, nanowires could assemble

deterministically into cross- or T-shaped pairs, or into more complex shapes [1.41]. It is also possible to use specific interactions between selectively functionalized segments of these nanowires to direct the assembly of nanowire dimers and oligomers, to prepare two-dimensional assembly of nanowire-substrate epitaxy, and to prepare three-dimensional colloidal crystals from nanowire-shaped objects [1.42]. As an example, single-stranded DNA can be exclusively modified at the tip or any desired location of a nanowire, with the rest of the wire covered by an organic passivation monolayer. This opens the possibility for site specific DNA assembly [1.27]. Nicewarner-Pena et al. showed that the controlled sequence of multisegment nanowires can be used as “barcodes” in biological assays [1.43]. The typical dimension of the nanowire is ~200 nm thick and ~10 μm long. Because the wavelength dependence of reflectance is different for different metals, the individual segments are easily observed as “stripes” under an optical microscope with unpolarized white-light illumination. Different metal stripes within a single nanowire selectively adsorb different molecules, such as DNA oligomers, which can be used to detect different biological molecules simultaneously. These multisegment nanowires have been used like metallic barcodes in DNA and protein bioassays. The optical scattering efficiency of the multisegment nanowires can be significantly enhanced by reducing the dimensions of the segment, such that the excitation of the surface plasmon occurs. Mock et al. [1.44] have studied the optical scattering of multisegment nanowires of Ag, Au, and Ni that have diameters of ~30 nm and length up to ~7 μm . The optical scattering is dominated by the polarization-dependant plasmon resonance of Ag and Au segments. This is different from the case of the thicker nanowires used by Nicewarner-Pena et al., where the reflectance properties of bulk metals determine the contrast of the optical images [1.43]. Because of the large enhancement by the surface plasmon resonance, very narrow (~30 nm diameter) nanowires can be readily observed under white light illumination and the optical spectra of the individual segments are easily distinguishable [1.44]. The multisegment nanowires can host a large number of segment sequences over a rather small spatial range, which promises unique applications.

1.3.4. Nanoelectronic and Nanoelectrochemical Applications

In addition to multisegment metal nanowires, one can also fabricate a metal/organic film/metal junction [1.45] and metal/nanoparticle/metal junctions [1.46] in a single nanowire, which have been used to study electron transport properties of the small amount of molecules and nanoparticles. It has been demonstrated that a Au nanowire containing 4-[2-nitro-4-(phenylethynyl) phenyl ethynyl] benzenethiol molecule junction exhibits negative differential resistance at room temperature [1.47], while a 16-mercaptohexadecanoic acid nanojunction exhibits a coherent nonresonant tunneling [1.48]. If some of the metal segments or “stripes” are being replaced with semiconductor, colloidal, and polymer layers, one can introduce rectifying junctions, electronic switching, and photoconductive elements in the composite nanowires. If selectively modifying the nanowire further, using the distinct surface chemistry of different stripes, the nanowires can be positioned on a patterned surface to fulfill nano-logic and memory circuits by self-assembling [1.46, 1.49]. An array of metal nanowires can be used as a nanoelectrode array for many electrochemical applications [1.50]. For this purpose, a large array of nanowires with long-range hexagonal order fabricated with the anodic alumina templates is particularly attractive.

1.3.5. Chemical Sensors

Penner, Handley, and Dagani et al. exploited hydrogen sensor applications using arrays of Pd nanowires [1.50,1.52]. Unlike the traditional Pd-based hydrogen sensor that detects a drop in the conductivity of Pd upon exposure to hydrogen, the Pd-nanowire sensor measures an increase in the conductivity. The reason is because the Pd wire consists of a string of Pd particles separated with nanometer-scale gaps. These gaps close to form a conductive path in the presence of hydrogen molecules as Pd particles expand in volume. The volume expansion is well known, which is due to the disassociation of hydrogen molecules into hydrogen atoms that penetrate into the Pd lattice and expand the lattice. Although macroscopic Pd-based hydrogen sensors are

readily available, they have the following two major drawbacks. First, their response time is between 0.5 s to several minutes, which is too slow to monitor gas flow in real time. Second, they are prone to the poisoning of a number of gas molecules, such as methane, oxygen, and carbon monoxide, which adsorb onto the sensor surfaces and block the adsorption sites for hydrogen molecules. The Pd nanowires offer remedies to the above problems. They have a large surface-to-volume ratio, so the response time can be as fast as 20 ms. The large surface-to-volume ratio also make the nanowire sensor less prone to the poisoning by common contaminations.



1.4 Reference

- [1.1] F. Keller, M. S. Hunter, and D. L. Robinson, *J. Electrochem. Soc.* 100, 411 (1953).
- [1.2] J. P. O'Sullivan and G. C. Wood, *Proc. R. Soc. London, Ser. A* 317, 511 (1970).
- [1.3] C. R. Martin, *Acc. Chem. Res.* 28, 61 (1995).
- [1.4] O. Jessensky, F. Muller, and U. Gosele, *Appl. Phys. Lett.* 72, 1173 (1998).
- [1.5] H. Masuda and K. Fukuda, *Science* 268, 1466 (1995).
- [1.6] A. R. Despic, *J. Electroanal. Chem. Interfacial Electrochem.* 191, 417 (1985).
- [1.7] R. C. Furneaux, W. R. Rigby, and A. P. Davidson, *Nature* 337, 147 (1989).
- [1.8] D. Crouse, Y.-H. Lo, A. E. Miller, and M. Crouse, *Appl. Phys. Lett.* 76, 49 (2000).
- [1.9] H. Masuda, H. Yamada, M. Satoh, H. Asoh, M. Nakao, and T. Tamamura, *Appl. Phys. Lett.* 71, 2770 (1997).
- [1.10] H. Masuda and M. Satoh, *Jpn. J. Appl. Phys.* 35, L126 (1996).
- [1.11] A.-P. Li, F. Muller, A. Birner, K. Nielsch, and U. Gosele, *Adv. Mater.* 11, 483 (1999).
- [1.12] L. S. Van Dyke and C. R. Martin, *Langmuir* 6, 1123 (1990).
- [1.13] G. Che, B. B. Lakshmi, C. R. Martin, E. R. Fisher, and R. R.S., *Chem. Mater.* 10, 260 (1998).
- [1.14] M. Wirtz, M. Parker, Y. Kobayashi, and C. R. Martin, *Chem. Eur. J.* 8, 353 (2002).
- [1.15] G. Yi and W. Schwarzacher, *Appl. Phys. Lett.* 74, 1746 (1999).
- [1.16] Y. H. Huang, H. Okumura, and G. C. Hadjipanayis, *J. Appl. Phys.* 91, 6869 (2002).
- [1.17] C. Z. Wang, G. W. Meng, Q. Q. Fang, X. S. Peng, Y. W. Wang, Q. Fang, and L. D. Zhang, *J. Phys. D* 35, 738 (2002).
- [1.18] D. H. Qin, C. W. Wang, Q. Y. Sun, and H. L. Li, *Appl. Phys. A-Mater.* 74, 761 (2002).
- [1.19] M. S. Sander, A. L. Prieto, R. Gronsky, T. Sands, and A. M. Stacy, *Adv. Mater.* 14, 665 (2002).
- [1.20] C. K. Preston and M. J. Moskovits, *J. Phys. Chem.* 97, 8495 (1993).
- [1.21] K. Liu, K. Nagodawithana, P. C. Searson, and C. L. Chien, *Phys. Rev. B* 51, 7381 (1995).

- [1.22] K. H. Lee, H. Y. Lee, W. Y. Jeung, and W. Y. Lee, *J. Appl. Phys.* 91, 8513 (2002).
- [1.23] P. Forrer, F. Schlottig, H. Siegenthaler, and M. Textor, *J. Appl. Electrochem.* 30, 533 (2000).
- [1.24] S. Valizadeh, J. M. George, P. Leisner, and L. Hultman, *Electrochim. Acta* 47, 865 (2001).
- [1.25] C. Schonenberger, B. M. I. van der Zande, L. G. J. Fokkink, M. Henny, C. Schmid, M. Kruger, A. Bachtold, R. Huber, H. Birk, and U. Staufer, *J. Phys. Chem. B* 101, 5497 (1997).
- [1.26] T. Thurn-Albrecht, J. Schotter, G. A. Kastle, N. Emley, T. Shibauchi, L. Krusin-Elbaum, K. Guarini, C. T. Black, M. T. Tuominen, and T. P. Russell, *Science* 290, 2126 (2000).
- [1.27] B. R. Martin, D. J. Dermody, B. D. Reiss, M. M. Fang, L. A. Lyon, M. J. Natan, and T. E. Mallouk, *Adv. Mater.* 11, 1021 (1999).
- [1.28] T. M. Whitney, J. S. Jiang, P. C. Searson, and C. L. Chien, *Science* 261, 1316 (1993).
- [1.29] L. Piraux, J. M. George, J. F. Despres, C. Leroy, E. Ferain, R. Legras, K. Ounadjela, and A. Fert, *Appl. Phys. Lett.* 65, 2484–2486 (1994).
- [1.30] S. Dubois, J. M. Beuken, L. Piraux, J. L. Duvail, A. Fert, J. M. George, and J. L. Maurice, *J. Magn. Magn. Mater.* 165, 30 (1997).
- [1.31] S. Pignard, G. Goglio, A. Radulescu, and L. Piraux, *J. Appl. Phys.* 87, 824 (2000).
- [1.32] C. L. Chien, *J. Appl. Phys.* 69, 5267 (1991).
- [1.33] T. Thurn-Albrecht, J. Schotter, C. A. Kastle, N. Emley, T. Shibauchi, L. Krusin-Elbaum, K. Guarini, C. T. Black, M. T. Tuominen, and T. P. Russell, *Science* 290, 2126 (2000).
- [1.34] H. Zeng, R. Skomki, L. Menon, Y. Liu, S. Bandyopadhyay, and D. J. Sellmyer, *Phys. Rev. B* 65, 13426 (2002).
- [1.35] P. R. Evans, G. Yi, and W. Schwarzacher, *Appl. Phys. Lett.* 76, 481 (2000).
- [1.36] K. Liu, C. L. Chien, P. C. Searson, and Y. Z. Kui, *Appl. Phys. Lett.* 73, 1436 (1998).
- [1.37] K. Hong, F. Y. Yang, K. Liu, D. H. Reich, P. C. Searson, C. L. Chien, F. F. Balakirev, and G. S. Boebinger, *J. Appl. Phys.* 85, 6184 (1999).

- [1.38] Y. M. Lin, S. B. Cronin, J. Y. Ying, M. S. Dresselhaus, and J. P. Heremans, *Appl. Phys. Lett.* 76, 3944 (2000).
- [1.39] M. Tanase, L. A. Bauer, A. Hultgren, D. M. Silevitch, L. Sun, D. H. Reich, P. C. Searson, and G. J. Meyer, *Nano Lett.* 1, 155 (2001).
- [1.40] M. Tanase, D. M. Silevitch, A. Hultgren, L. A. Bauer, P. C. Searson, G. J. Meyer, and D. H. Reich, *J. Appl. Phys.* 91, 8549 (2002).
- [1.41] B. D. Reiss, J. N. K. Mbindyo, B. R. Martin, S. R. Nicewarner, T. E. Mallouk, M. J. Natan, and C. D. Keating, *Mate. Res. Soc. Symp. Proc.*, in press (2001).
- [1.42] J. S. Yu, J. Y. Kim, S. Lee, J. K. N. Mbindyo, B. R. Martin, and T. E. Mallouk, *Chem. Commun.* 2445 (2000).
- [1.43] S. R. Nicewarner-Pena, R. G. Freeman, B. D. Reiss, L. He, D. J. Pena, I. D. Walton, R. Cromer, C. D. Keating, and M. J. Natan, *Science* 294, 137 (2001).
- [1.44] J. J. Mock, S. J. Oldenburg, D. R. Smith, D. A. Schultz, and S. Schultz, *Nano Lett.* 2, 465 (2002).
- [1.45] J. K. N. Mbindyo, T. E. Mallouk, J. B. Mattzela, I. Kratochvilova, B. Razavi, T. N. Jackson, and T. S. Mayer, *J. Am. Chem. Soc.* 124, 4020 (2002).
- [1.46] N. I. Kovtyukhova, B. R. Martin, J. K. N. Mbindyo, T. E. Mallouk, M. Cabassi, and T. S. Mayer, *Mater. Sci. & Eng. C* 19, 255 (2002).
- [1.47] I. Kratochvilova, M. Kocirik, A. Zambova, J. Mbindyo, T. E. Mallouk, and T. S. Mayer, *J. Mater. Chem.* 12, 2927 (2002).
- [1.48] I. Kratochvilova, A. Zambova, J. Mbindyo, B. Razavi, and J. Holakovsky, *Modern Phys. Lett. B* 16, 161 (2002).
- [1.49] N. I. Kovtyukhova and T. E. Mallouk, *Chem. Euro. J.* 8, 4355 (2002).
- [1.50] K. Uosaki, K. Okazaki, H. Kita, and H. Takahashi, *Anal. Chem.* 62, 652 (1990).
- [1.51] F. Favier, E. C. Walter, M. P. Zach, T. Benter, and R. M. Penner, *Science* 293, 2227 (2001).

[1.52] E. C. Walter, F. Favier, and R. M. Penner, *Anal. Chem.* 74, 1546 (2002).

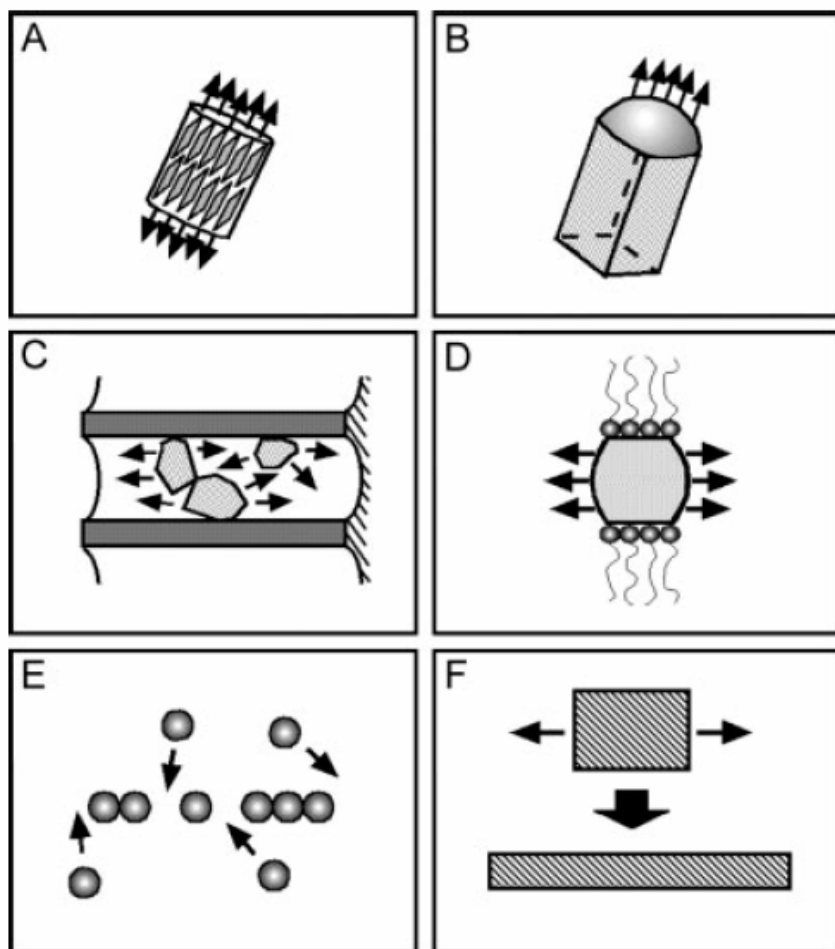


Figure 1.1 schematically illustrates some of six synthetic strategies.

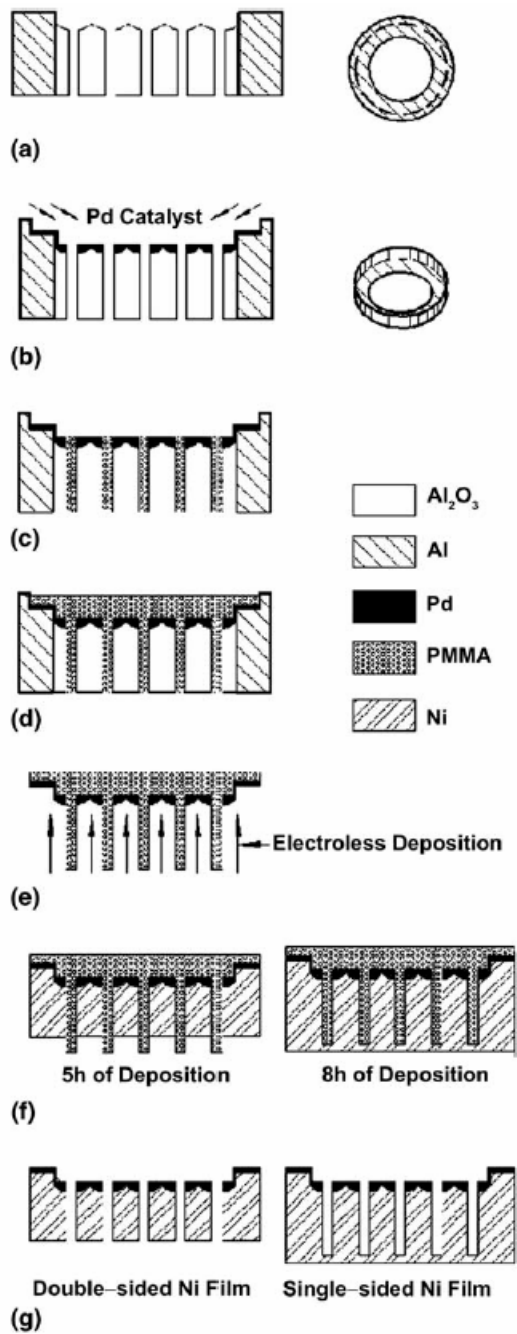


Fig.1.2 Schematic outline of the fabrication of nanoporous Ni film: (a) through-hole alumina membrane, (b) deposition of the Pd catalyst layer, (c) immersion of alumina membrane in MMA and pre-polymerization of MMA, (d) polymerization of MMA, (e) removal of alumina membrane and electroless metal deposition, (f) double-faced and single-faced nanoporous Ni films and (g) removal of PMMA.

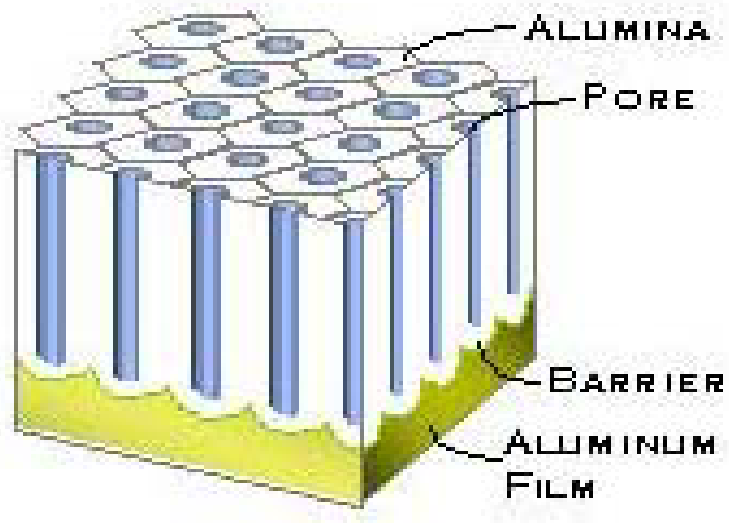


Fig1.3 Schematic drawing of an anodic porous alumina template.



Chapter 2

Characterization and Composition Evolution of Multiple-Phase Nanoscaled Ceramic Powder by Laser Ablation

2.1 Introduction

Particles with nanometer-scale size have large ratio of surface to bulk atoms. Large surface always gives high active behavior and changes both physical and chemical properties. Inorganic nanoparticles having size generally smaller than 100nm provide superior properties for various applications and become important topic in nanomaterials.

Many methods are developed to prepare inorganic nanoparticles during recent year[2.1]. Chemical route includes metal-organic compounds the so-called precursors and reaction through hydrolysis, condensation, catalysis, pyrolysis, etc[2.2,2.3]. Evaporation-condensation is mainly the process in physical route [2.4] and laser ablation is the important method included in this route.[2.5] Nanoparticle of inorganic materials can easily be produced by laser ablation because inorganic materials can easily be evaporated by high energy laser beam and be subsequently condensed into particles. For complex or multiphase material, composition and phase of ablated particle are easily adjustable through composition/phase modification of target [2-6]. However, there will be phase separation occurred when multiphase or complex oxide is used as target. Therefore, modification of target composition is important to recover the composition of nanoparticle and upgrade the properties.

Ceramic particles of complex or multiphase oxide often possess multifunction that have been applied for far-infrared emission ceramic, fiber and many kind of textile. Material owned high efficiency far-infrared emission using transitional element oxide had been reported[2.7,2.8]. In this work, multiphase target composed of Al_2O_3 , ZnO , TiO_2 and ZrO_2 is selected for the study. Target microstructure and processing conditions including laser energy, chamber pressure, and flow rate of carrier gas will be investigated to composition, particle size distribution and phase of ablated

nanoparticles. In addition, The far-infrared emissivity characteristic of nanoparticles based on $ZrTiO_4$ -- $ZnAl_2O_4$ system was investigated as functions of nanoparticle size, composition and formation phase.

2.2 Experimental

Targets for the physical process of nanoparticle synthesis are made from conventional ceramic process. Oxides chosen from ZrO_2 , TiO_2 , ZnO and Al_2O_3 (all purity>99.5%) micropowders were used as raw materials. The mixtures with the ratio of ZrO_2 : TiO_2 : ZnO : Al_2O_3 = 1:1: 2: 2(ZAT1,mole ratio) and 2: 2:1:1(ZAT2) were mixed and then compressed into 30mm diameter green compaction. After calcination at 1100°C, disk-type sample was press-formed and then sintered at 1300°C for 2h to make dense target for laser ablation.

Excimer laser (248nm) power is varied to study the ablation efficiency for different materials. The laser irradiation conditions of 0~4 J/cm² were used in this work. Three gases, air, oxygen and nitrogen, were used for carrier gas (set up flow rate 2L/min) with remained ambient atmospheres around 1 atm.

Transmission electron microscope (TEM, JEM2010&EDS) was used to characterize composition and image of nanoparticles at 200keV. The semi-quantitative EDS analysis of nanoparticles determined the atomic ratio of element Zr, Ti, Zn and Al. Crystal phase were identified by X-ray diffraction and selected area electron diffraction pattern. Surface image and mapping analysis were obtained from field emission scanning electron microscope (FESEM, LEO1530). Far-infrared emissivity characterization of nanoparticles were investigated by using infrared spectrophotometer with black body furnace as reference beam source. Sample were prepared for emissivity test by coating on glass plate with 3cm diameter.

2.3 Results and discussion

2.3.1 Microstructure evolution of ablated target

Figure 1 show the XRD patterns of the target after thermal treatment. Only $ZrTiO_4$, $ZnAl_2O_4$ and residual ZrO_2 was detected (Fig.2.1.a). The microstructure of target ZAT1 and ZAT2 were primarily composed of granular $ZnAl_2O_4$ crystal about (2 μm) and submicro prismatic $ZrTiO_4$ crystal. In order to investigate the relationship between laser fluence and nanoparticles composition, phase transition of microstructure of ZAT1 and ZAT2 target under different laser fluence was examined. As shown in Fig.2.2 show surface evolution. It was observed that the surface evolution changes from relief structure to smooth structure while the applied laser fluence increases. Figure 2.3 shows the surface element mapping for ZAT1 under 0.34 J/cm^2 . Mapping result disclosed prominent area contains Zr-rich and concave area has Zn-rich. It means that Zr-rich area was subjected to a lower ablation rate but a higher ablation rate was applied at Zn-rich area under 0.34 J/cm^2 fluence. That is the reason why the generated fine nanoparticles contain higher Zn content and lower Zr content. In addition, Al element distribution is similar to Zn element, and Ti element could be found at the whole area. As increasing the fluence over threshold value, all oxide compounds or elements could be laser-ablated to generate nanoparticles with homologous microstructure and compositions other than Zn content.

2.3.2 Morphology of ablated nanoparticle

Prior to laser ablation for multiphase oxide, single oxide compound was first studied. I was found that ZrO_2 has a higher threshold energy density of 3~5 J/cm^2 and TiO_2 is 1~1.5 J/cm^2 . The nanoparticles with an average particle size of 20~40 nm under threshold fluence can be obtained by laser ablation process. On the other hand, both ZnO and Al_2O_3 have lower threshold of 0.4 - 0.6 J/cm^2 , but 5~20 nm finer nanoparticles were generated. According to the ablation model for single oxide ceramic, it reveals that many parameters such as bonding strength, absorption property and wavelength will influence the threshold energy density. Therefore, for multiphase oxide compound, it would become more complicated because of different bonding strength or threshold fluence. According to laser-ablation experiment for ZAT1 and ZAT2, 0.34 J/cm^2 fluence only obtains

ablation rate of 0.3~0.7 $\mu\text{g}/\text{shot}$ at air atmosphere that was below threshold . As increasing the fluence to 1 J/cm^2 and 4 J/cm^2 , the ablation rate of 1.9~3.2 $\mu\text{g}/\text{shot}$ and 2.3~3.4 $\mu\text{g}/\text{shot}$, respectively, can be reached that is near the saturated ablation condition. Therefore, three fluences of 0.34, 1 and 4 J/cm^2 would be used for the laser ablation process .

Nanoparticles produced by 0.34~4 J/cm^2 laser fluence at air atmosphere show amorphous-like structure [Fig. 2.1b and c] and exhibit two kind of particle size distribution with fine nanoparticles of 5~20 nm (70~90%) and large spherical nanoparticles of 40~100 nm (10~30%) as shown in Fig.2.4.a,b,c). While stronger laser fluence was applied, the number of large spherical particles becomes more (is increased). According to static method, average particle size of 8.2 nm, 10.7 nm and 11.6 nm was obtained under 0.34, 1 and 4 J/cm^2 of laser fluence, respectively. The influence of laser power on the crystallization evolution of nanoparticle is also observed in Fig. 2.5 for ZAT1 and ZAT2 where both exhibit different phase evolution. However, The phase crystallization increases with a stronger fluence. The electron diffraction pattern shows better crystalline particle for high laser power (1 J/cm^2) but lower laser power gives amorphous-like particle. These results may explain both gas and liquid phases existed in the ablated agglomeration. The higher laser power digs out larger particle with liquid phase on its surface. Good crystallization is also found for these large particles. When the low laser power is applied, the only excited particle is gas-like phase and will be consolidated into amorphous phase because of the quench effect of flow gas or atmosphere. Therefore, fine particle with amorphous phase is found (see Fig.2.4.b). The amorphous fine particle can be crystallized by electron beam during TEM observation or temperature treatment. Therefore, it can be summarized. The higher laser power gives larger particles with wide size distribution, while the lower ones provides fine particles with narrow size distribution. Compromise between laser power and temperature treatment can produce fine particle with narrow size distribution and good crystallization.

As the nanoparticles were synthesized in nitrogen atmospheres, the nanoparticles in Fig. 2.4.d appeared wilder particle distribution than that synthesized in air atmospheres. On the other hand, in

oxygen atmospheres, some hollow nanoparticles as shown in Fig.2.4.e.f.appear in this condition. Gas flow to bring out particle from surface changes ablation rate. Increasing flow rate carries out more particles and makes the surrounding environment easier for the following particle generation. The ablation rate varies with the change of atmosphere condition because gas flow to bring out particle from surface occurs during laser ablation and changes with atmosphere condition. It was found that oxygen has a larger density and viscosity ($1.43 \times 10^{-3} \text{g/cm}^3$ and $2.08 \times 10^{-5} \text{g/s} \cdot \text{cm}$, Poise) than air ($1.32 \times 10^{-3} \text{g/cm}^3$ and $1.86 \times 10^{-5} \text{g/s} \cdot \text{cm}$, Poise) and nitrogen ($1.25 \times 10^{-3} \text{g/cm}^3$ and $1.79 \times 10^{-5} \text{g/s} \cdot \text{cm}$, Poise). Therefore, in oxygen atmospheres, the laser-induced plume become small due to the short mean free path because of high viscosity and thus it causes more probability for the laser beam to irradiate the agglomerated nanoparticles to generate large hollow nanoparticles

2.3.3 Phase separation of ablated nanoparticle

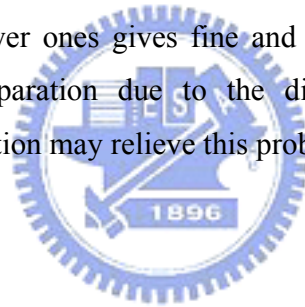
Composition of the generated nanoparticles from both targets of ZAT1 and ZAT2 were inspected by TEM and EDS analysis based on a normalized molar ratio of atoms with $\text{Zr}+\text{Ti}+\text{Zn}+\text{Al}=100\%$. Fig.2.6 show element evolution of three types of nanoparticles under different fluences in air atmosphere. Both ZAT1 target have similar result as ZAT2, but element show more close value under 1 and 4 J/cm^2 laser fluence for fine nanoparticles. For fine nanoparticles (5~20nm) generated from ZAT2 target, it was found that Zn content decreases but Zr content increases while the laser fluence rises. In addition, both Al and Ti content present similar trend to Zr but littler irregular. However, in the case of large spherical nanoparticles (40~100nm), the Zn content was apparently decreased but the others increase with an increase of laser fluence. It was believed that because Zn content was easier evaporated into gas phase than the others as the fine nanoparticles were condensed from vapor phase, more Zn content would be trapped. In addition, as the larger crystalline particles were formed, the EDS shows that it was primarily composed of Zr over 70 % with little Zn.

2.3.4 Far-infrared ray emissivity characteristion

The far-infrared ray emissivity characterization of nanoparticles based on $\text{ZrTiO}_4\text{-ZnAl}_2\text{O}_4$ system was investigated with black body furnace as a reference of 1. Table 2.1 summarized the average emissivity of more than 80% fine nanoparticles (wavelength in the range of 4 to 12 μm) under different condition. The average emissivity were as function of the synthesized nanoparticle size, composition and formation phase and varies upward with increasing large spherical particles and crystal phase ratio .

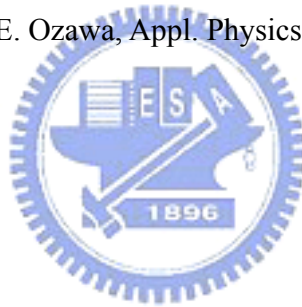
2.4. Summary

Laser ablation is an important and useful method for oxide nanoprcles with single or multiphase. Surface of target will be annealed by laser power and presents nearly constant ablation rate after several shots. Higher laser power creates larger particle with good crystallization, while lower ones gives fine and amorphous particles. Multiphase target suffers from phase separation due to the different laser absorption ability. Modification of target composition may relieve this problem.



2.5 References

- [2.1]M. Choi, J. Nanoparticle Res., 3 (2001) 201-211
- [2.2]K. Landfester, Adv. Mater., 13 (2001) 765-768
- [2.3]Y. C. Kang, S. B. Park and Y. W. Kang, Nanostructured Mater. 5 (1995) 771-791
- [2.4]Z. Paszti, G. Peto, Z. E. Horvath and A. Karacs, Appl. Surface Sci., 168 (2000) 114-117
- [2.5]T. Sasaki, S. Terauchi, N. Koshizaki and H. Umehara, Appl. Surface Sci., 127-129 (1998) 398-402
- [2.6]K. Tanaka and D. Sonobe, Appl. Surface Sci., 140 (1999) 138-143
- [2.7]H. Takashima, Yogyo-Kyokai-Shi 89,[12](1981)655-660
- [2.8]H. Takashima, K. Matsubara, Y. Nishimura and E. Kato, Yogyo-Kyokai-Shi 90,[7](1982)373-379
- [2.9]Y. Kawakami, T. Seto and E. Ozawa, Appl. Physics A69[Suppl.],(1999)249-252



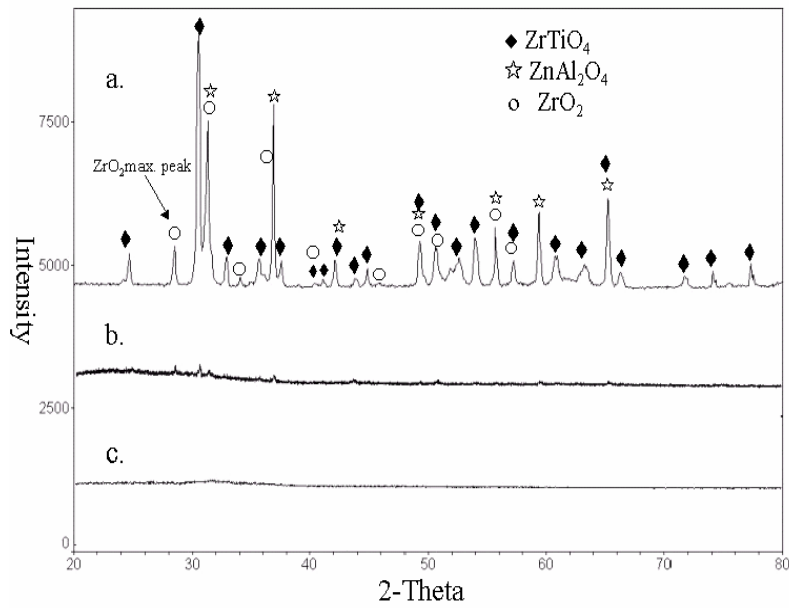


Fig.2.1.a. XRD pattern of crystal phases of ZAT1 target after thermal treatment. b. XRD pattern of nanoparticles produced by 4 J/cm^2 laser fluence at air atmosphere. c. XRD pattern of nanoparticles produced by 0.34 J/cm^2 laser fluence at air atmosphere.

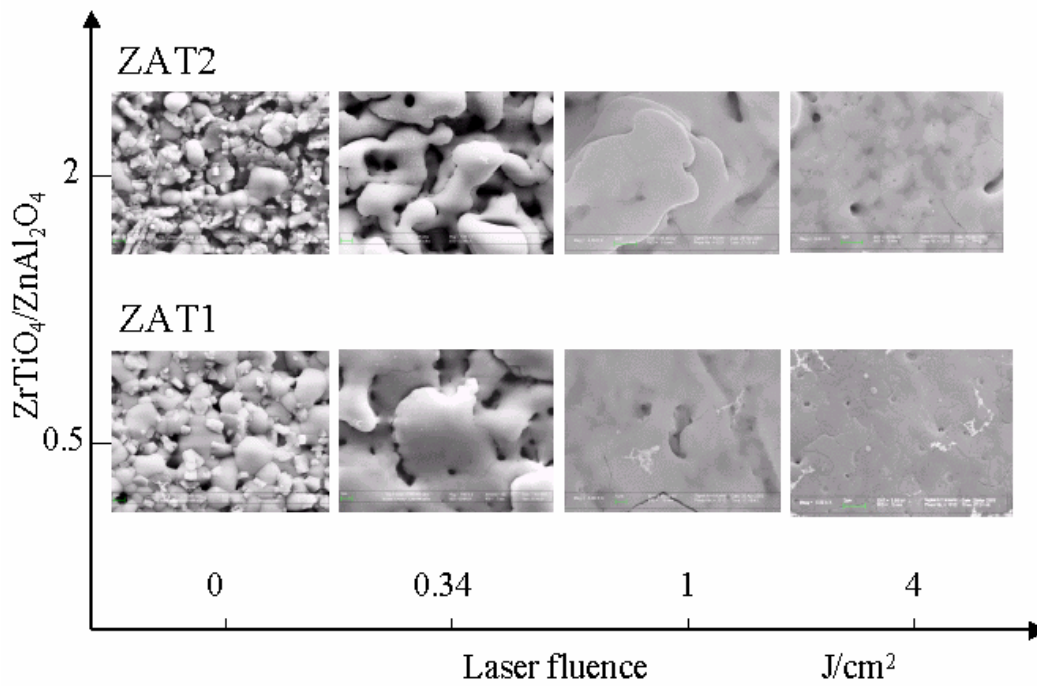


Fig.2.2 Surface evolution of ZAT1 and ZAT2 target

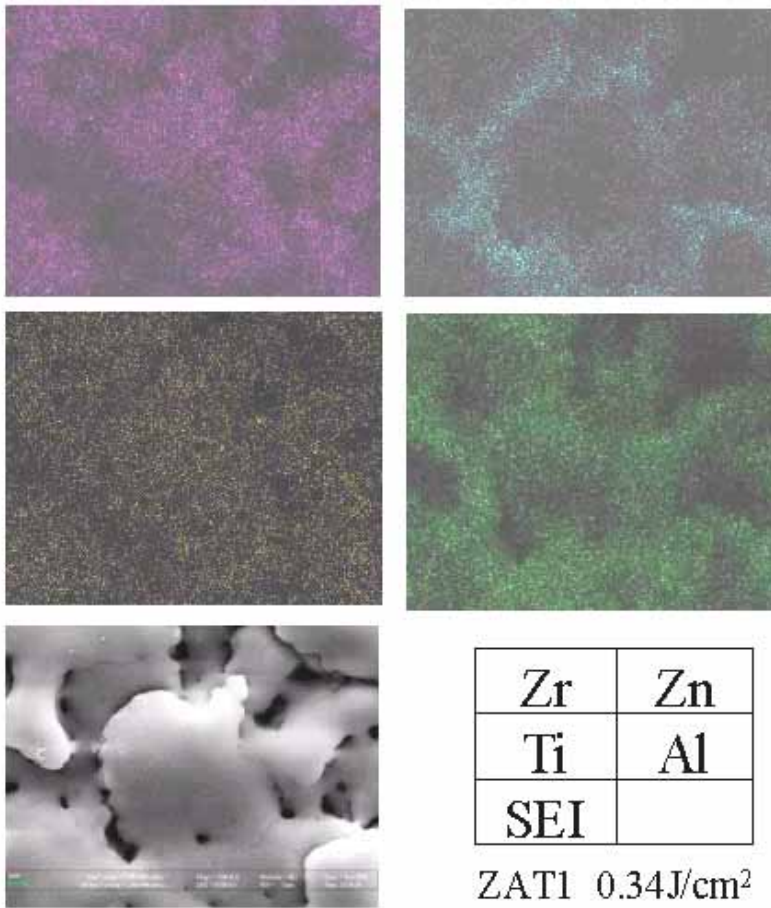


Fig.2.3. Surface mapping for ZAT1 under 0.34 J/cm²

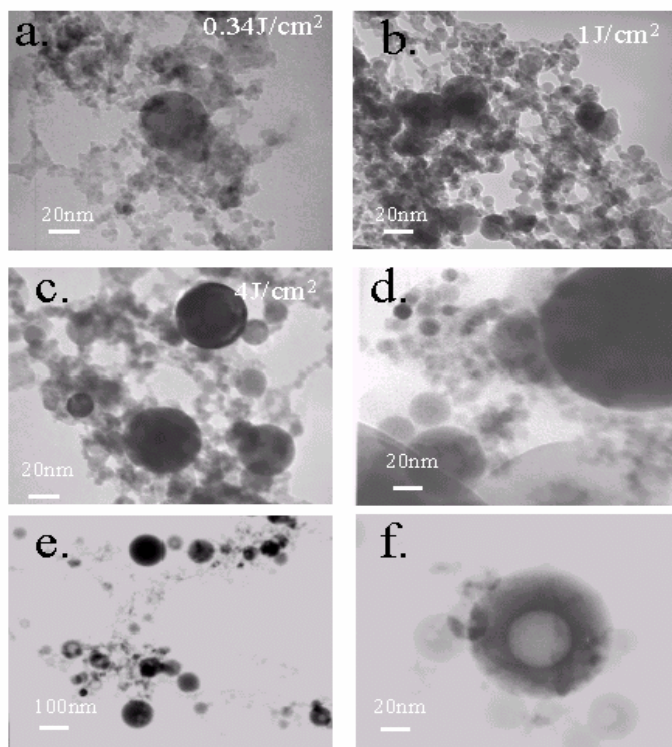


Fig.2.4.a.b.c. Nanoparticles produced by 0.34~4 J/cm² laser fluence irradiating at air atmosphere. 2.4.d . nanoparticles synthesized at nitrogen atmospheres. 2.4..e&f. nanoparticles synthesized at oxygen atmospheres.

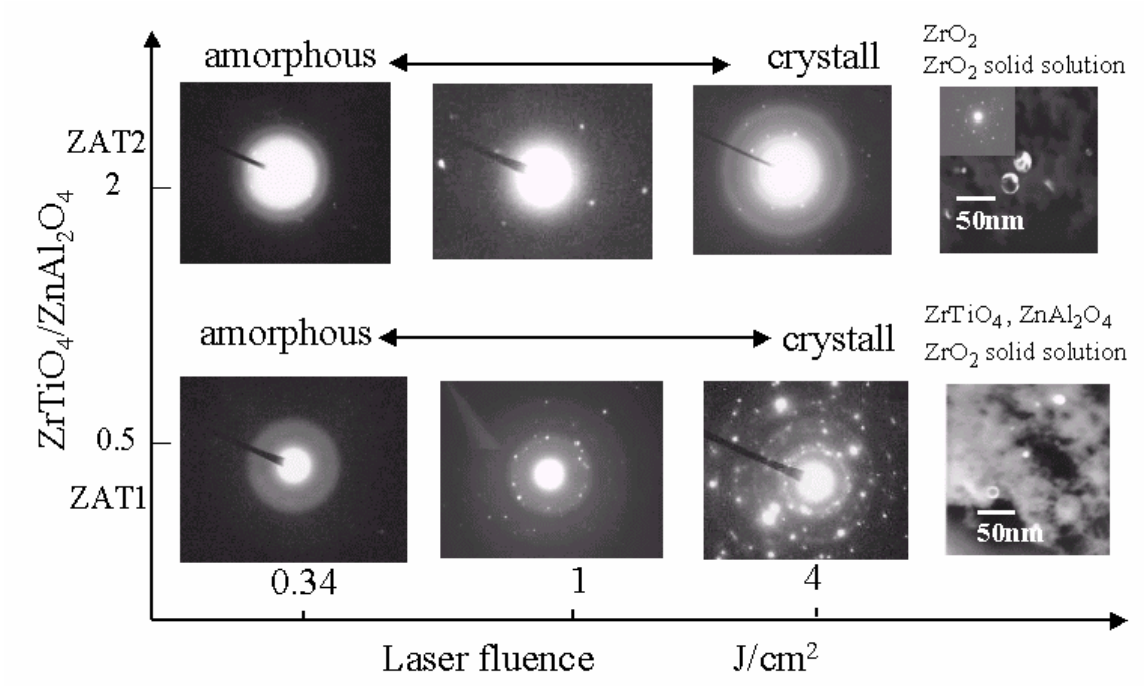


Fig.2.5. The evolution of TEM diffraction pattern of nanoparticles of ZAT1 and ZAT2 under different fluence



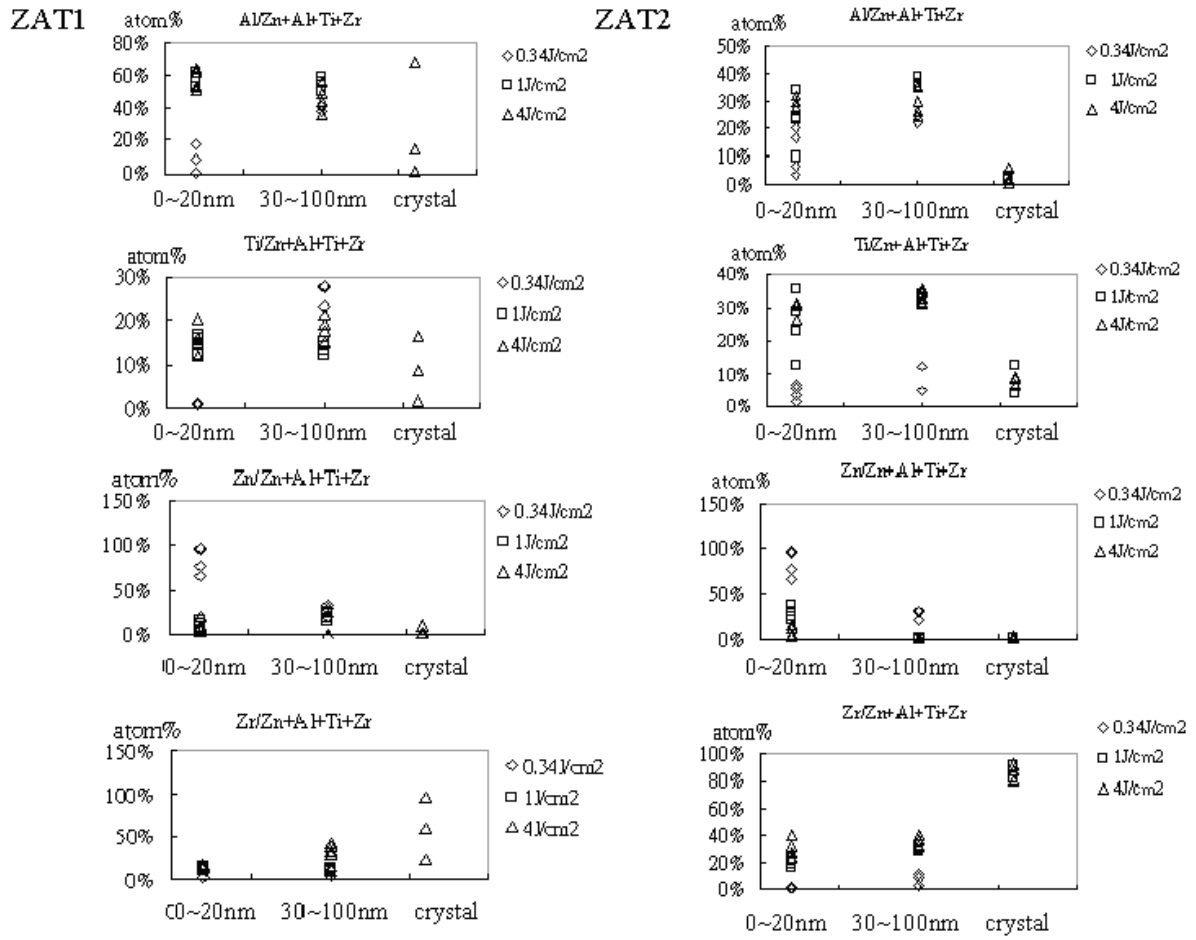


Fig.2.6. element evolution of three type nanoparticles under different fluence and air atmosphere

target	fluence J/cm ²	amorphous-like nanoparticle		crystal phase Vol%	far-infrared average emissivity wavelength range 4~ 12μm	
		fine nanoparticle Vol%	large spherical particles Vol%		test at 36°C	test at 60°C
ZAT1	0.34	80~85%	15~20%	<1%	0.85	0.87
ZAT1	1	70~80%	20~30%	<2%	0.86	0.89
ZAT1	4	70~80%	20~30%	<6%	0.88	0.92
ZAT2	0.34	85~90%	10~15%	<1%	0.83	0.85
ZAT2	1	75~85%	15~25%	<3%	0.85	0.88
ZAT2	4	70~80%	20~30%	<5%	0.86	0.89

Table 2.1 summarized the average emissivity of the nanoparticles that were more than 80 % (wavelength range from 4 to 12μm) under different condition.



Chapter 3

Nanoscaled TiO₂/Ag catalyst and photodecomposition characteristic

3.1 Introduction

The photodecomposition of various pollutants by TiO₂ has been demonstrated to be efficient under ultraviolet light [3.1-3.16]. The photocatalytic activity of TiO₂ can also be enhanced by modifying its surface with noble metals and metal oxides [3.8]. These photocatalysts are utilized in many approaches. For example, TiO₂ photocatalysts anchored on supporting materials with large surface areas have been developed to eliminate the shortcomings of the filtration and the suspension of fine photocatalyst particles [3.5]. TiO₂ photocatalysts anchored on various substrates were prepared using a pasting treatment, an ionized cluster beam (ICB) method or a sol-gel method [3.6]. The sol-gel method is frequently adopted to prepare TiO₂ thin films on supported substrates [3.1-3.7, 3.10-3.13]. However, heat treatment may cause a phase transition of TiO₂ and reduce the photocatalytic activity [3.5].

This study proposes the anchoring of well-dispersed nano TiO₂ on a metal carrier using a binder-free, low temperature process. Well-dispersed nano TiO₂ deposited on a branch-like silver (Ag) carrier, called “nano-TiO₂/Ag catalyst” was synthesized here to overcome the aforementioned shortcomings. This study discusses the preparation, morphology and reaction kinetics of photocatalytic activity of nano-TiO₂/Ag catalyst.

3.2 Experimental

An Ag carrier was prepared based on the reaction, $2\text{Ag}^+ + \text{Cu} \rightarrow 2\text{Ag} + \text{Cu}^{+2}$. The net redox potential of the reaction is 0.5V indicating that the reaction occurs spontaneously. In a pretest, the formation of the branch-like Ag carrier was favored in the acidic solution at high concentration [17]. Bulk copper (Cu) was placed in AgNO₃ solution at a ratio of Cu: AgNO₃: water =5: 3: 100 (wt %), to yield Ag particles. Nitric acid was added to give the solution a pH of 3. The solution temperature was set to 25°C, which was maintained for 2 hrs. Then, the precipitate was rinsed with D.I water to remove residues.

Secondly, an appropriate amount of TiO₂ particles (P25, Degussa) was placed in the solution at various pH values, obtained by adjusting the amount of NH_{3(aq)} or nitric acid

added. The solution was treated ultrasonically for 90mins. No dispersing agent was added to the solution. The experimental design was such that 5 wt % of TiO₂ was mixed with Ag carrier at various pH conditions. A critical coverage ratio of TiO₂ of approximately 5% was identified: exceeding this dosage of TiO₂ may result in aggregation under all test pH conditions. The mixture was stirred for 30 mins to increase the number of opportunities for contact between nano TiO₂ particles and Ag carriers. Finally, a composite of nano TiO₂ particles and Ag carrier was synthesized by washing, filtering and drying, in that order. Table 3.1 presents the characteristics of nano-TiO₂/Ag catalyst used in this study.

Methylene blue (MB) is a representative dye that is commonly adopted to evaluate the catalytic activity of a catalyst. The test conditions were as follow; 1g of catalyst, 30 ml of 100 ppm MB solution, UV light with a wavelength of 254 nm and an illumination intensity of 4mW/cm². The UV lamp was placed 6cm above the test sample. The mixture (MB and catalyst) was stirred gently while being irradiated. A centrifuge was used to separate the mixture after irradiation had been completed. The absorption of the MB supernatant was then determined using a spectrophotometer (Unico UV2102). A blank experiment (without a catalyst) was also performed; the results indicated that irradiation did not significantly change MB absorbance. The photocatalytic activity was defined as

$$\eta = \frac{C_{\text{initial}} - C_{\text{irradiation}}}{C_{\text{initial}}} \times 100\%$$

where C_{initial} and C_{irradiation} are the absorbance of MB before and after irradiation. The morphology of the catalysts is observed by field emission-scanning electron microscopy (FE-SEM, LEO, 1530).

3.3 Results and discussion

The SEM images of the Ag nanoparticles are shown in Figure 3.1. Figure 3.1a~3.1d shows the typical SEM images of the product obtained by self-reducing the solution with concentration from 0.1wt% to 1.5wt% AgNO₃. It is apparent that Ag nanoparticles display dendritic growth while concentration>0.5wt%. We believe that the excess of silver in the solution may be favorable for the aggregation and growth into the dendritic structures of the Ag cluster. It is found that the concentration of AgNO₃ plays a significant role in the formation and growth of the silver nanoparticles. When the concentration of AgNO₃ is decreased to 0.2wt%, the flake-like Ag can

also be observed as shown in Fig 3.2c, 3.2d. Rather, the Ag nanoparticles display irregular flake shapes with the size of about 1 μ m in diameter. It is found that the concentration of AgNO₃ also plays a key role in the formation of Ag nanoparticles.

Fig. 3.2 is the XRD patterns of the as-prepared 1.5wt% AgNO₃ sample, in which five strong peaks can be indexed to diffraction from the (1 1 1), (2 0 0), (2 2 0), (3 1 1) and (2 2 2) of face-centered cubic (fcc) Ag, and no impurity peaks from silver oxide were detected. Fig. 3.3a shows the SEM images of well-defined silver dendrites with pine-like shape. It is found that the side branches are well symmetric and the angles of them to the main branches are all about 60°, which implies that all side branches grow along the same direction. With careful observation (Fig. 3.3b and 3.3c), the side branches of these dendritic Ag are constructed by lots of well-crystallized small nanorods with diameter of 50–60 nm and length up to 200nm. The inset SAED pattern from one of the left side branch (in Fig. 3.3d) reveals that the Ag dendrite has single crystal nature with cubic phase and the side branch direction assembles along [0 1 1] direction. It may suggest that the large dendrites grow from small clusters and in many places the dendrites lack corners and arms.

In the catalyst preparation, TiO₂ nanoparticles were initially suspended in solution. The corresponding zeta potentials of the TiO₂ solution at pH 11, pH 6.2 and pH 3 were measured to be -55, -2.5 and 28 mV, respectively. These results revealed that TiO₂ particles tended to be negatively charged by the excess bonding of hydroxyl ion (OH⁻) in the alkaline solution (pH 11), and positively charged by the excess bonding of hydrogen ion (H₃O⁺) in the acidic solution (pH 3), suggesting that the electric repulsion between TiO₂ nanoparticles was very strong in both alkaline and acidic solutions, causing their “effective-dispersion”.

When the Ag particles were mixed with TiO₂ particle solution at pH 11, pH 6.2 and pH 3, the resultant composite was as shown in Fig 3.4. 1a~1c, respectively. A composite of well-dispersed nano TiO₂ anchored on Ag carrier was formed in alkaline solution (pH 11, Fig. 3.4a), while nano-TiO₂ aggregated in the neutral solution (pH 6.2, Fig. 3.4b). Almost no TiO₂ particles were deposited on the Ag carrier in acidic solution (pH 3, Fig. 3.4c). The results indicated that the pH status significantly affects the combination of nano TiO₂ and Ag carriers. The surface of the Ag carrier is preferentially oxidized because of its extreme activity if the size of the Ag particles is reduced to the nano-scale [17]. Accordingly, the positively oxidized Ag surface spontaneously attracted negative

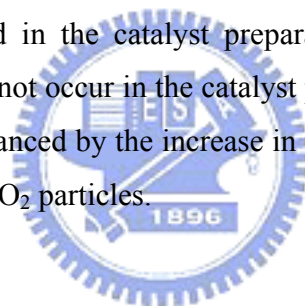
TiO₂ particles in the alkaline solution, yielding the composite, “well-dispersive ” TiO₂ anchored on Ag carriers, as shown in Fig. 3.4a. In neutral solution (pH=6.2), the repulsive force between the nano TiO₂ particles was very weak, because neutral pH was very close to the isoelectric point [18]. H₂O molecules provide a “bridge” between nano TiO₂ particles via hydrogen bonding, resulting in the aggregation of TiO₂ particles, as shown in Fig. 3.4b. Positive TiO₂ particles could not be easily anchored on positive Ag carrier, because of the electric repulsion, as shown in Fig. 3.4c. Consequently, the effective dispersion of nano TiO₂ and Ag carriers is governed by electrostatic attraction, achieved by adjusting the pH status of solution.

The prepared catalysts, as shown in Fig. 3.4 at various pH values were then examined to determine the photocatalytic activity. As seen in Fig. 3.5, gradual changes in the absorbance of MB were observed from its characteristic absorption at 250nm, 290nm and 666 nm. The absorbance decreased in the order Cat. pH 11, Cat. pH 6.2 and Cat. pH 3 with an irradiation period of 20mins. This result indicates that the “pH status in the catalyst preparation” not only affects the dispersion between nano-TiO₂ particles but also significantly influences the photocatalytic activity, and can be clearly distinguished from the results in Figs. 3.4 and 3.5. Cat. pH 6.2 has a higher MB-absorbance (and thus a lower photocatalytic activity) than Cat. pH 11, even though both nano-TiO₂ particle loadings were identical. The photocatalytic activity was evidently reduced by the aggregation of nano-TiO₂ particles. Larger aggregated nano TiO₂ particles correspond to less surface area exposed to UV irradiation. Therefore, the enhancement of the photocatalytic activity of nano-TiO₂/Ag catalyst depends on effective dispersion and an appropriate proportion of nano-TiO₂, and can be achieved in this approach without adding a dispersive agent or binder.

Figure 3. 6 plots photocatalytic activity as a function of reaction time. The photocatalytic activity also followed the order Cat. pH 11, Cat. pH 6.2 and Cat. pH 3 for various periods of irradiation. Cat. pH 11 and Cat. pH 6.2 reached a decomposition efficiency of over 90% after an irradiation time of 2hrs. Cat. pH 11 was associated with the near complete decomposition of MB after irradiation for 1 hr. Notably, the MB concentration (100ppm) tested herein is much higher than the 10ppm tested in the literature [3, 5, 10]. A high initial MB concentration was removed completely in a short period, indicating that

the well-dispersed nano-TiO₂/Ag catalyst exhibited outstanding catalytic activity. Cat. _{pH 3} comprised mainly the Ag carrier, which still had a decomposition efficiency of 40% after irradiation for 2hrs, suggesting that the Ag carrier also exhibited photocatalytic activity.

Table 3.2 presents the rate constant calculated from the results in Fig. 3.6. The rate constant of all nano-TiO₂/Ag catalysts was determined for a first-order reaction, and was consistent with the results found in the literature [3, 5, 10]. However, the reaction rate constant of Cat. _{pH 11} obtained herein clearly exceeded those in the literature [3, 5, 10]. Zainal et al. [5], prepared TiO₂ thin film using a typical sol-gel method, and the catalysts was accomplished by a heat treatment at 600°C for 6hrs. The TiO₂/glass treated at 600°C contained a rutile phase TiO₂. Unfortunately, the calcination period was usually several hours, to ensure strong adhesion on the substrate. The amount and crystallinity of the formed rutile increased with the calcination temperature. In this study, well-dispersed nano TiO₂ particles were combined with Ag carriers in the alkaline solution. No further thermal annealing was applied in the catalyst preparation. The aggregation or phase transition of TiO₂ particles did not occur in the catalyst preparation herein. Therefore, the photocatalytic activity was enhanced by the increase in the effective reactive surface area of the “well-dispersed” nano TiO₂ particles.



3.4 Summary

A highly dispersed nano-TiO₂/Ag catalyst is synthesized in an alkaline solution. Nearly all of the dimethy-blue target pollutant at high concentration was removed when the photoreaction was performed in a short period. This novel nano TiO₂ photocatalyst exhibits excellent photocatalytic activity because it is well dispersed. Since no dispersant or organic binder was used, this synthetic process has the advantages of low cost and convenience.

3.5 Reference

- [3.1]C. H. Kwon, H. Shin, J. H. Kim, W. S. Choi, K.H. Yoon: *Mater. Chem. Phys.*, **86**, 78 (2004).
- [3.2]M. Inagaki, T. Imai, T. Yoshikawa, B. Tryba: *Appl. Catal. B-Environ.*, **51**, 247 (2004).
- [3.3]S. Senthilkumaar, K. Porkodi, R. Vidyalakshmi: *J. Photoch. Photobio. A*, **170**, 225 (2005).
- [3.4]P. Fu, Y. Luan, X. Dai: *J. Mol. Catal. A-Chem.*, **221**, 81 (2004).
- [3.5]Z. Zainal, L. K. Hui, M. Z. Hussein, Y. H. Taufiq-Yap, A. H. Abdullah, I. Ramli: *J. Hazard. Mater. B*, **125**, 113 (2005).
- [3.6]S.-Y. Lu, C.-H. Chang, C.-H. Yu, H.-L. Chen, Y.-H. Lo: *J. Mater. Res.*, **20**, 1523 (2005).
- [3.7]X.-Y. Chuan, M. Hirano, M. Inagaki: *Appl. Catal. B-Environ.*, **51**, 255 (2004).
- [3.8]M. I. Litter: *Appl. Catal. B-Environ.*, **23**, 89 (1999).
- [3.9]L. Zhang, J. C. Yu, H. Y. Yip, Q. Li, K. W. Kwong, A.-W. Xu, P. K. Wong: *Langmuir*, **19**, 10372 (2003).
- [3.10]S. Senthilkumaar, K. Porkodi, R. Gomathi, A. G. Maheswari, N. Manonmani: *Dyes. Pigments.*, **69**, 22 (2006).
- [3.11]C. He, Y. Yu, X. Hu, A. Larbot: *Appl. Surf. Sci.*, **200**, 239 (2002).
- [3.12]X. You, F. Chen, J. Zhang, M. Anpo: *Catal. Lett.*, **102**, 247 (2005).
- [3.13]J. Yu, J. Xiong, B. Cheng, S. Liu: *Appl. Catal. B-Environ.*, **60**, 211 (2005).
- [3.14]C.-H. Wu, C.-L. Chang, C.Y. Kuo: *React. Kinet. Catal. Lett.*, **86**, 37 (2005).
- [3.15]H. Liu, L. Gao: *Chem. Lett.*, **133**, 730 (2004).
- [3.16]L. Adamcikova, K. Pavlikova, P. Sevcik: *React. Kinet. Catal. Lett.*, **69**, 91 (2000).
- [3.17]Y.H. Cheng, S.Y. Cheng: *Nanotechnology*, **15**, 171 (2004).
- [3.18]Y. Zhao, Y. Zhang, W. Xing, N. Xu: *Desalination*, **177**, 59 (2005).

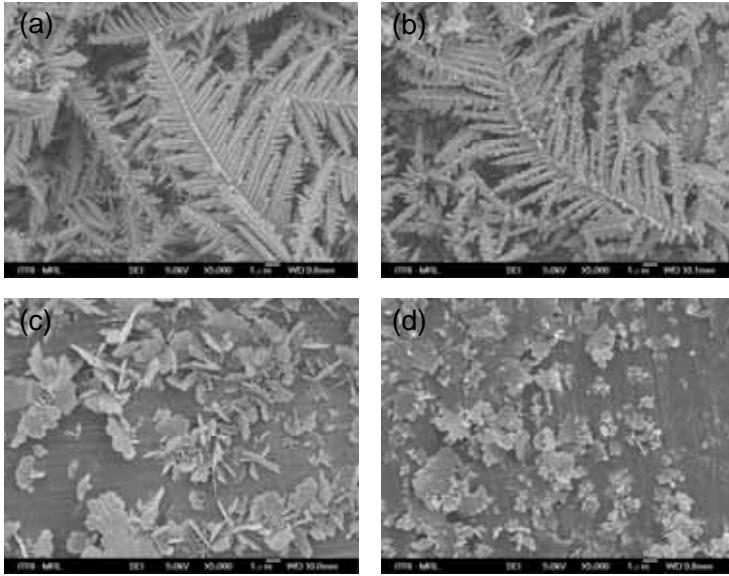


Fig.3.1. The SEM images of the Ag nanoparticles

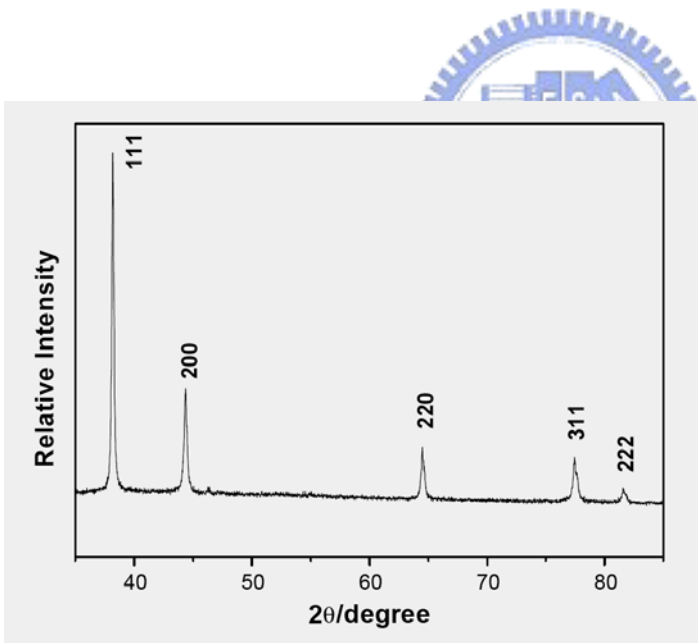


Fig.3.2 XRD patterns of the as-prepared 1.5wt% AgNO₃ sample

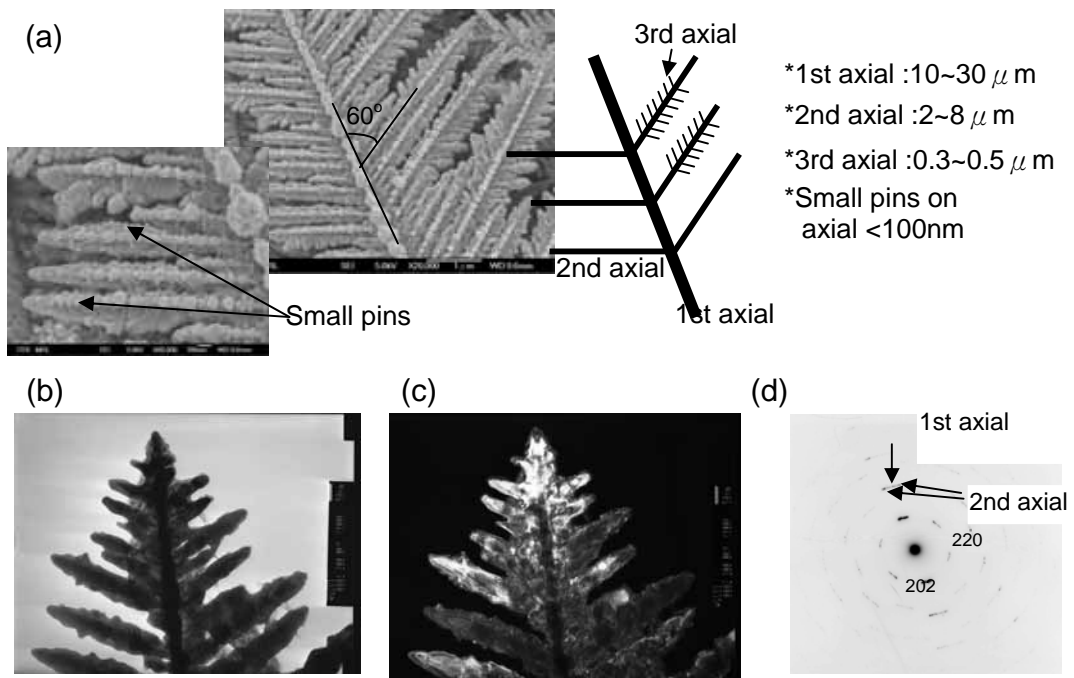


Fig.3.3 The images of well-defined silver dendrites with pine-like shape.



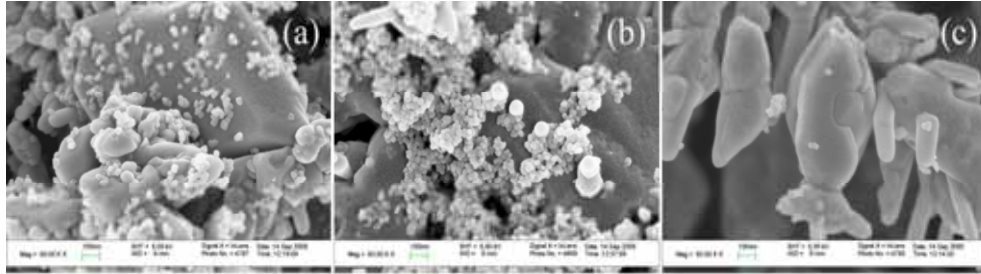


Fig. 3.4 Influence of pH status on the morphology of nano-TiO₂/Ag photocatalyst. (a): pH 11, (b): pH=6.2. (c): pH=3



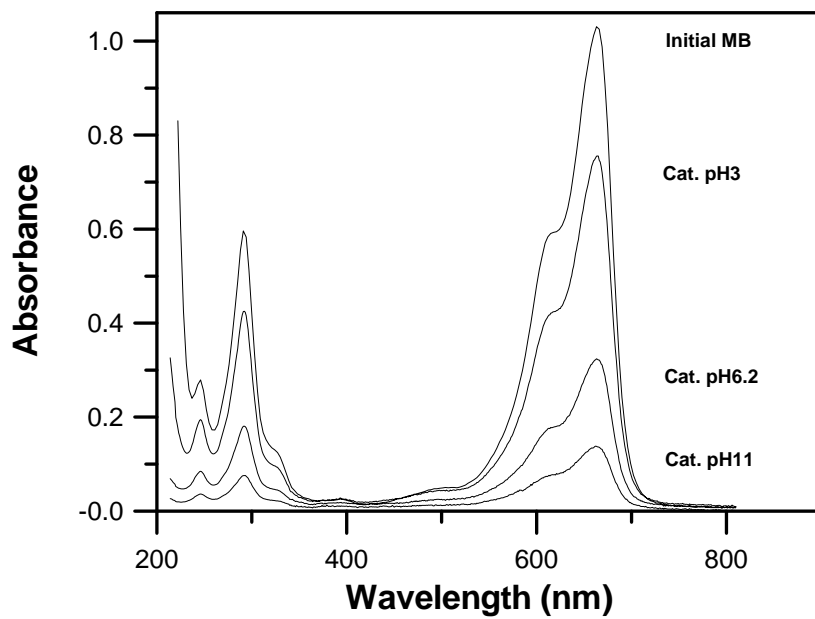


Fig. 3.5 MB absorbance of nano TiO_2/Ag catalysts used in this study. The data was obtained after an irradiation of 20mins.



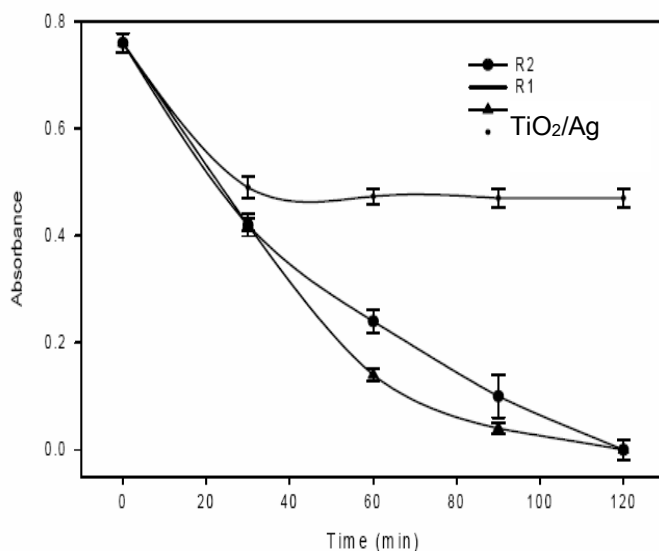
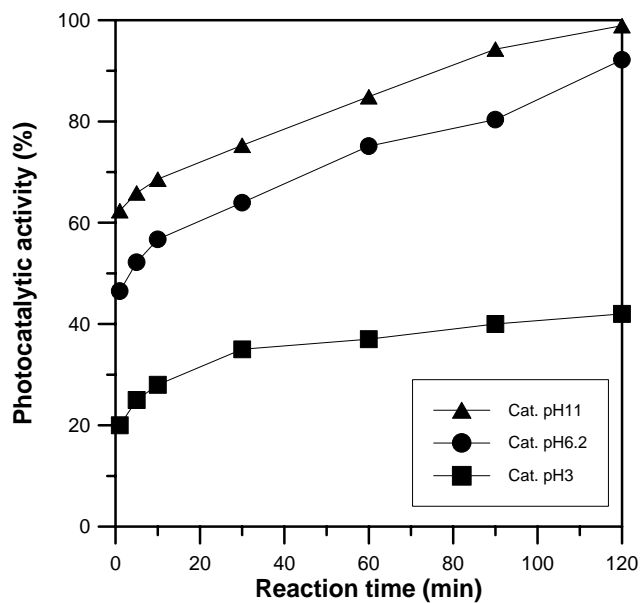


Fig.3.6(1) Photocatalytic activity of catalyst as a function of irradiation time. Experimental conditions: 1g catalyst weight, 30ml of 100ppm MB solution.
 (2) Compare methylene blue degradation in sunlight over the TiO₂/Ag catalysts R1(Ishihara) and R2(Degussa), with 0.4 g of catalyst/100 ml of 10⁻⁴ M dye solution, duration 120 min

Table 3.1. Characteristics of nano-TiO₂/Ag catalyst used in this study.

Catalyst name	TiO ₂ nanoparticle content (wt%)	TiO ₂ phase
Cat. pH 11	4.7	80%anatase ¹
Cat. pH6.2	4.8	80%anatase ¹
Cat. pH 3	0.2*	80%anatase ¹

*: TiO₂ nanoparticles content of Cat. pH 3 was synthesized at pH 3, the positive TiO₂ was difficult to adhere to the surface of positive Ag carrier.

¹: TiO₂ nanoparticles were purchased from Ultra Fine Chemical Technology Corporation (Degussa P-25).



Table 3.2. Reaction constants of nano-TiO₂/Ag catalysts for the photodecomposition of methylene blue.

Type	Reaction constant of decomposing rate, k ($\frac{1}{\text{min}}$)	R-square
Cat. pH 11	0.0269	0.93
Cat. pH 6.2	0.0142	0.95
Cat. pH 3	0.0024	0.86



Chapter 4

Synthesis and magnetic properties of highly arrayed nickel-phosphate nanotubes

4.1. Introduction

Magnetic film and nanowires have been the most interesting and intensely investigated fields of material in recent year[4.1-4.5]. The fabrication of magnetic metal arrays has not only the fundamental worth in these materials but also their potential utilization in magnetic recording. For high density storage media, one single nanosized pattern, ordered nanodots or nanotubes is a single domain structure and denotes one bit signal. Magnetic period nano-structure arrays as an ultra-high-density magnetic storage can achieve recording densities of more than 100Gbit/in², which is more than the continuous magnetic film of 40Gbit/in²[4.6-4.8]. Arrays of ferromagnetic nonodots, nanowires or nanotubes may be fabricated by several methods such as e-beam lithography, imprint technology or template. The porous template can be considered as one quicker and cheaper method to prepare highly perpendicular magnetic anisotropy structure [4.9-4.12] because AAO(anode alumina oxide) has high oriented porous structure with uniform and nearly parallel pores that can be organized the pseudo ordered nanowire or nanotube arrays. Such structure also shows high magnetic anisotropy phenomena with the shape axis parallel to the nanowire arrays.

On the other hand, it is well known that transition metals such as Fe, Co, Ni and their alloy have higher saturation magnetization as well as Curie temperature, and lower crystalline anisotropy. Furthermore, magnetic properties are strongly influenced by the dimension and crystal properties, which also depend on the physical structure of templates and growth mechanism of wires or tubes. Recently, magnetic properties of nickel nanowires have been investigated by several groups because nickel nanowires show important applications in magnetic recording[4.13-4.14].

Compared with the electrodepositing method, electroless deposition needs neither power nor

smooth interface. In this study, it was found that there exist some variation in nucleation rate from heterogeneities process and some defects are also induced in this process. By adjusting deposition, we have fabricated uniform size nanotube and nanowire arrays by autocatalytic electroless deposition in AAO. Furthermore, the effect of experimental conditions on the morphology of nanostructure will be discussed. The preliminary results of their magnetic properties are also reported.

4.2. Experimental procedure

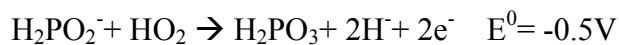
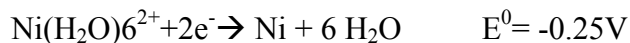
High ordered AAO templates with pore diameter of about 50~200nm were used from commercial porous alumina templates (Whatman 6809 7013). The electrolyte solution was prepared from NiSO₄, NaH₂PO₂, NaC₂H₃O₂ and Na₃C₆H₅O₇. One side of AAO templates was sputtered with 200nm Au film as catalytic layer. The coated template was first immersed in an aqueous solution and kept at low vacuum environment to enhance the solution into the pores. Subsequently, Ni-P nanowire arrays were deposited in the the pores from the electrolyte solution at 80~95°C and pH 3~6 adjusted by sulfuric acid and ammonia. For obtaining the isolated Ni-P nanowire arrays, the Ni-P deposited AAO was dissolved in 5 wt% NaOH solution at 25 °C for 20 min and then slightly washed several time to remove the original AAO template.

The microstructure and morphology were characterized by transmission electron microscopy (TEM) and scanning electron microscopy (SEM). The magnetic properties were measured by magnetometer. X-ray diffraction (XRD) and energy dispersive spectra (EDS) are employed to study the morphology and chemical composition of nanotubes. The magnetic property of Ni nanotubes is characterized using a vibrating sample magnetometer (VSM).

4.3. Results and discussion

The redox reactions would take place spontaneously in electroless bath if total electrochemical potential ΔE^0 value is positive. The autocatalytic redox reactions of Ni-P nanotube arrays in an acid

medium are shown in the following equations:



The E^0 represents the single electrode potential. If the E^0 value of a reducing reaction is lower than that of oxide reaction, the Ni-P deposited reaction will possibly take place in electrolytic solution. According to the E^0 value, Ni and P could be reduced by $\text{NaH}_2\text{PO}_2(\text{aq})$. However, as a rule, these reaction could not proceed without catalyst. Therefore, Au film usually acts as a catalyst in the reaction.

Fig.4.1 shows pH-Potential of Ni-H₂O group and P-H₂O group at room temperature. Three stable regions of Ni²⁺, Ni and NiO are illustrated in Ni-H₂O group : Ni keeps stable at low potential for any pH values. If potential increases (>-0.25V), Ni will be oxidized as Ni²⁺ (at pH<6) or NiO (at pH>6). In pH-Potential of P-H₂O group, it can be found that H₂PO₂-H₂PO₃ group appears at pH<6 in acid regions and H₂PO₂-HPO₃ group appear at pH>6 in alkaline regions. It is clear to understand that Ni could be formed regardless of at acid and alkaline electrolytic bath. However, precipitated NiO is much easily formed in alkaline electrolytic bath so that it would be better to control the bath at the pH<6. Besides, while changing temperature and complex agent, pH-Potential will be shifted but the tendency remains similar.

After removing the AAO in aqueous NaOH, Fig. 4.2 shows the SEM image of Ni-P nanotube arrays formed in an electrolytic bath at 90°C and pH=4.5. The nanotubes were estimated with the average dimension of 200~300nm and length of about 2µm. The TEM image of Ni-P nanotubes in Fig. 4.2c further shows that these nanotubes are uniform with the wall thickness about 40nm and the corresponding electron diffraction pattern indicates it is an amorphous structure. So far, most of the investigations in the literature have demonstrated the solid nanowires structure can be developed via AAO template. However, in this work, the formation of the tube structure could be

explained as follows. As the Au was sputtered into the pores, hollow structure could be formed as show in Fig. 4.2d. Next, the deposited Ni-P could cause preferring growth on the pore wall to form nanotubes. The energy disperse spectrometry analysis indicates that the nanotubes are composed of Ni and P (Fig.4.3).

The XRD patterns of Fig.4.4a further indicate that the Ni-P nanotubes exhibit amorphous structure with ~5 nm ultra-fine grains. However, as the nanotubes were heated up to 500°C in 95%N₂/5%H₂ atmosphere, Nickel HCP phase was detected as shown in Fig.4.4b. The grain size in the Ni-P nanotubes increases with increasing temperature. At 700 °C, the average grain size was estimated as 35 nm.

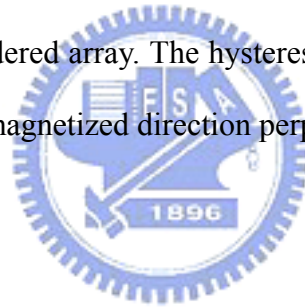
Moreover, it was found that different solution pH values in electrolytic bath result in the morphology change of the nano-structure. The wall of the nanotubes becomes thinner while increasing pH to 6 because the deposited rate will decrease under high pH value. Fig.4.5a shows this kind of structure where many sheet residues appear due to the deposition of NiO. On the other hand, at lower pH value, i.e., 3, both reduction and deposition rate of metal ions in the electrolytic bath become faster at the bottom of the pore. Therefore, nanowires instead of nanotubes were grown along the pore channel to form a solid structure (Fig.4.5b).

Fig.4.6 shows the hysteresis loop of the Ni-P nanotubes array measured at room temperature. The $H_{(pl)}$ and $H_{(pd)}$ represent external magnetic field parallel to Ni-P nanotubes and perpendicular to Ni-P nanotubes, respectively. While the sample was heated less than 300°C, no clear hysteresis loop of Ni-P nanotubes array was detected as shown in Fig. 4.6a that might be related to the amorphous structure. As heating the sample up than 500°C, a distinct hysteresis loop (Fig.4.6b) begins to appear and this suggests the formation of crystalline structure. It would be also found that both saturation magnetization (B_s) and remanence (B_r) of $H_{(pl)}$ are larger than those of $H_{(pd)}$. However, the coercive field (H_c) for $H_{(pl)}$ and $H_{(pd)}$ orientation are similar about 200Oe. As compared with the H_c of Co-P nanowires (800~1300Oe), the Ni-P nanotubes array are more suitable for magnetic recording.

The hysteresis loop also shows different magnetic anisotropy and this indicates that the easily magnetized direction is perpendicular to the nanotubes axis. Moreover, the arrays appear very low remanent magnetization less than 20% B_s . However, while continually increasing heat-treatment temperature up to 900°C, both coercive field and saturation of remanent magnetization of the nanotube arrays become much lower. This indicates that magnetic anisotropy of the nanotube arrays gradually disappears under overmuch thermal effect.

4.4. Summary

Electroless deposition with Au catalyst can be applied to fabricate Ni-P magnetic nanotube arrays by controlling electrolytic bath at 90°C and pH=4.5~6. The studies indicate that the highly ordered array nanotubes are amorphous structure with the average diameter of 200~300 nm and length of 2 μm and form a highly ordered array. The hysteresis loop of the array nanotubes shows magnetic anisotropy with the easily magnetized direction perpendicular to the nanotubes axis.



4.5 References

- [4.1] C.A. Ross, M. Hwang, M. Shima, H.I. Smish, M. Farhoud, T.A. Savas, W. Schwarzacher, J. Parrochon, W. Escoffier, H. Neal Bertram, F.B. Humphrey, M. Redjda, J. Magn. Magn. Mater. 249 (2002) 200.
- [4.2] A.J. Bennett, J.M. Xu, Appl. Phys. Lett. 82 (2003) 3304.
- [4.3] M. Shima, M. Hwang, C.A. Ross, J. App. Phys. 93 (2003) 3440.
- [4.4] X.Y. Yuan, G.S. Wu, T. Xie, Y. Lin, L.D. Zhang, Nanotechnology 15 (2004) 59.
- [4.5] X.Y. Yuan, G.S. Wu, T. Xie, Y. Lin, G.W. Meng, L.D. Zhang, Solid State Communications 130 (2004) 429–432.
- [4.6] R.M. White, R.M.H. New, R.F.W. Pease, IEEE Trans. Magn. 33(1996) 990.
- [4.7] D. Routkevitch, A.A. Tager, J. Haruyama, D. Almawlawi, M. Moskovits, J.M. Xu, IEEE Trans. Electron Devices 43(1996) 1646.
- [4.8] P.L. Lu, S.H. Charap, IEEE Trans. Magn. 30(1994) 4230.
- [4.9] S. Park, S. Kim, S. Lee, Z.G. Khim, K. Char, T. Hyeon, J. Am. Chem. Soc. 22 (2000) 8581.
- [4.10] A.J. Yin, J. Li, W. Jian, A.J. Bennett, J.M. Xu, Appl. Phys. Lett. 79 (2001) 1039.
- [4.11] Y.W. Wang, G.W. Meng, C.H. Ling, G.Z. Wang, L.D. Zhang, Chem. Phys. Lett. 343 (2001) 174.
- [4.12] W. Chen, S.L. Tang, M. Lu, Y.W. Du, J. Phys.: Condens. Matter 15 (2003) 4623.
- [4.13] G. Sauer, G. Brehm, S. Schneider, K. Nielsch, R.B. Wehrspohn, J. Choi, H. Hofmeister, U. Gosele, J. Appl. Phys. 91 (2002) 3243.
- [4.14] Yong Lei, Wai-Kin Chim, Zhongping Zhang, Tiejun Zhou, Lide Zhang, uowen Meng, Fritz Phillip, Chemical Physics Letters 380 (2003) 313–318.

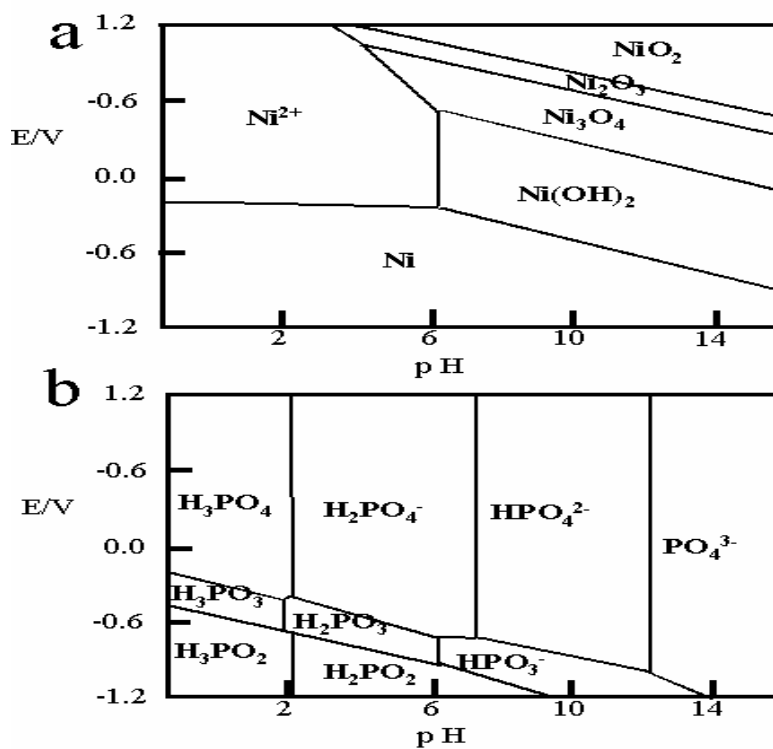


Fig.4.1(a) The diagram of pH-Potential of Ni-H₂O group and (b) P-H₂O group at room temperature.

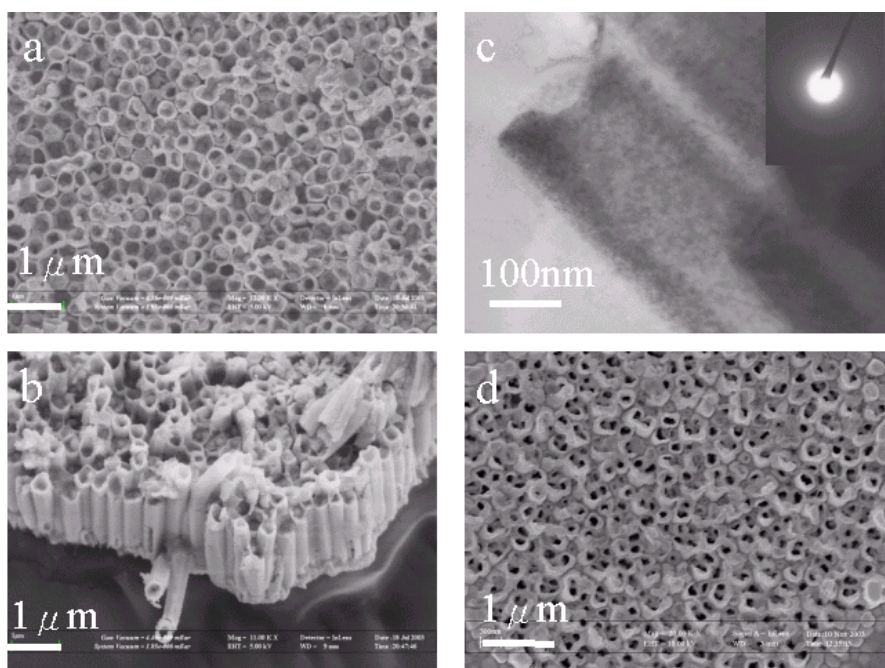


Fig.4.2 (a)(b) Up view and side view of the SEM image of Ni-P nanotube arrays controlling electrolytic bath at 90°C and $\text{pH}=4.5$. (c) TEM image and diffraction pattern of Ni-P nanotubes. (d)The hollow structure of catalyst Au film after removing the AAO in $\text{NaOH}(\text{aq})$.

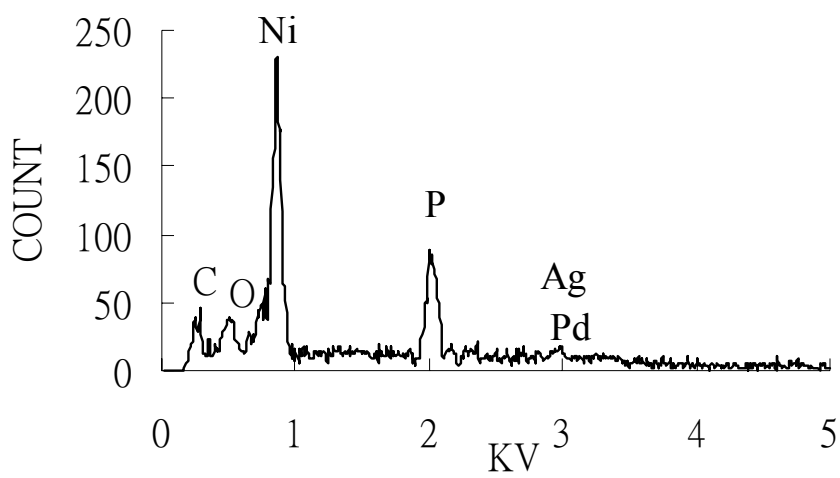


Fig.4.3 A energy disperse spectrometry analysis of nanotubes. The conductor film is the composition of Ag and Pd.

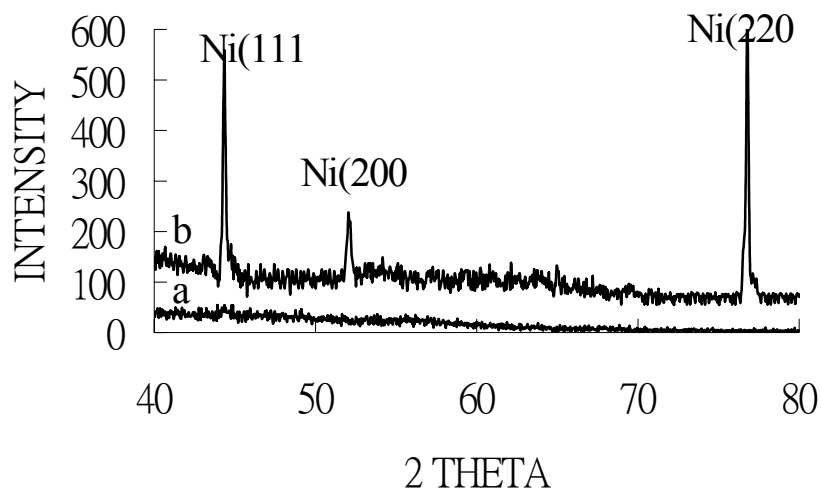


Fig.4.4 XRD diagram of Ni-P nanotubes (a) As-deposited sample reveals amorphous structure and (b) heated up to 500 °C sample at 95%N₂/5%H₂ atmosphere appears as Nickel HCP phase.

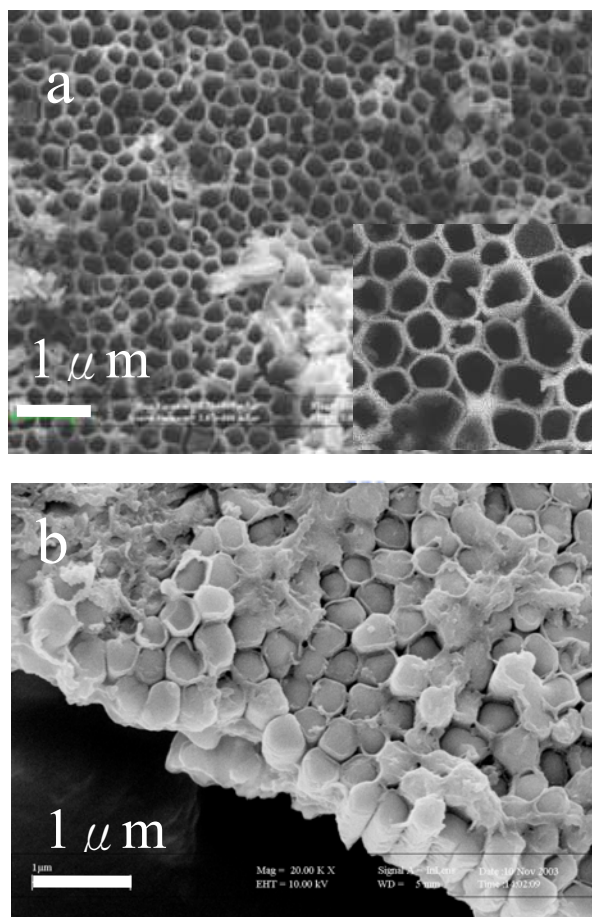


Fig.5 (a) The SEM image of thinner wall nanotubes are obtained while increasing pH to 6. (b) The solid nanowires structure is generated at pH=3.

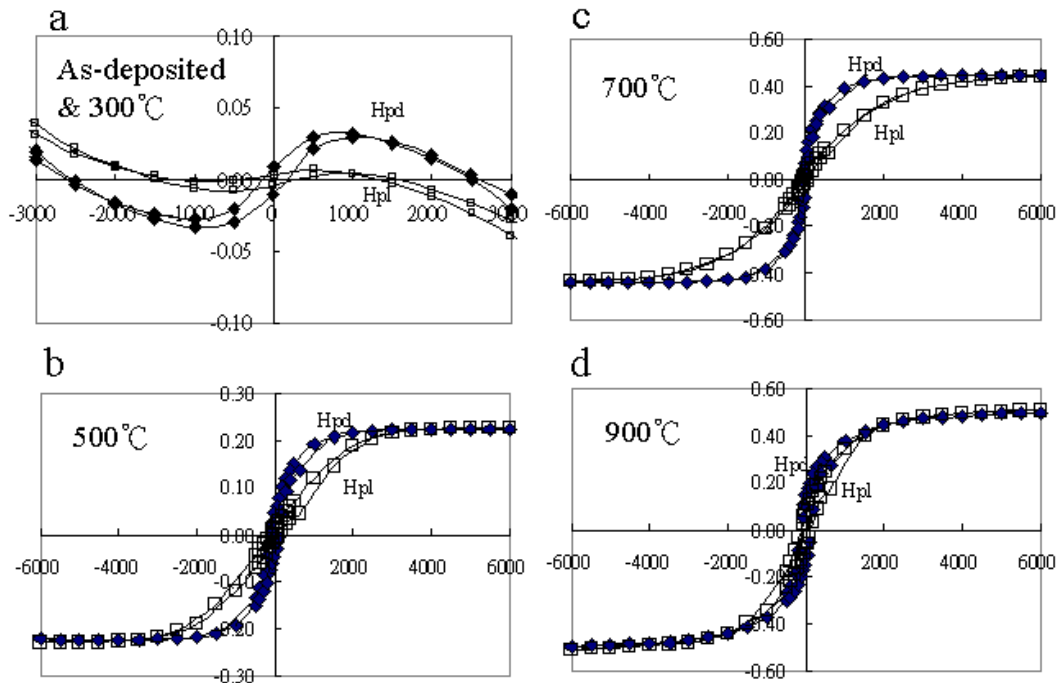


Fig.

6. The hysteresis loop of Ni-P nanotubes array measured at room temperature, 300°C, 500°C, 700°C and 900°C.

Chapter 5

Electrochemical fabrication and magnetic properties of highly ordered silver-nickel core-shell nanowires

5.1. Introduction

The fabrication of magnetic metal arrays has been intensely investigated recently because they shows potential utilization in magnetic recording[5.1-5.5]. It was reported that magnetic period nano-structure arrays as an ultra-high-density magnetic storage can achieve recording densities of more than 100Gbit/in², which is more than the continuous magnetic film of 40Gbit/in² [5.6-5.8]. Arrays of ferromagnetic nanodots, nanowires or nanotubes may be fabricated by several methods such as e-beam lithography, imprint technology or template. However, the porous template can be considered as one quicker and cheaper method to prepare highly perpendicular magnetic anisotropy structure [5.9-5.12] because AAO(anode alumina oxide) has high oriented porous structure with uniform and nearly parallel pores that can be organized for the pseudo ordered nanowires or nanotubes array.

On the other hand, it is well known that the ferromagnetic element such as Fe, Co, Ni and their alloy have higher saturation magnetization as well as Curie temperature, and lower crystalline anisotropy. Furthermore, magnetic properties are strongly influenced by the dimension and crystal properties, which also depend on the physical structure of templates and growth mechanism of wires or tubes.

However, these ferromagnetic element or alloy exhibits a lower magnetic anisotropy because these materials were usually polycrystalline and possessed random magnetic domain. Thus, one new structure and process was proposed in order to obtain higher magnetic anisotropy in this study. The silver-nickel core-shell nanowires arrays by electrodepositing in AAO templates were

synthesized and their magnetic properties were characterized. Furthermore, the effect of experimental conditions on the morphology of the core-shell nanostructure will be also discussed.

5.2. Experimental procedure

Highly ordered AAO templates with pore diameter of about 200nm were used from commercial porous alumina templates (Whatman 6809 7013). In the first stage, the silver electrolyte solution was prepared from $\text{Ag}(\text{NO}_3)_2$ (0.005M~0.02M) and $\text{Ac}(\text{NH}_3)$ (0.4M). One side of AAO templates was sputtered with 200nm Au film as electrode layer. The coated template was first immersed in an aqueous solution and kept at low vacuum environment to enhance the solution into the pores. Subsequently, silver nanowire arrays were deposited in the pores from the electrolyte solution under constant current of 4 mA and voltage of 0.6~1.5 V at room temperature. For obtaining the isolated silver nanowire arrays, the sample was dissolved in 5 wt% NaOH solution at 25 °C for 20 min and then slightly washed several time to remove the original AAO template.

In the second stage, nanoscale nickel layer was coated on the silver nanowire surface by nickel ions electrodepositing. The electrolyte solution was prepared from $\text{NiSO}_4 \cdot \text{H}_2\text{O}$ (0.8M), $\text{NiCl}_2 \cdot \text{H}_2\text{O}$ (0.48M), H_3BO_3 (0.6M) and H_2O_2 (30%, 0.01M) and named as Watts bath which is one kind of typical nickel plating bath. The $\text{NiSO}_4 \cdot \text{H}_2\text{O}$, $\text{NiCl}_2 \cdot \text{H}_2\text{O}$ were used as the source for the major Nickel hydrated ions and H_3BO_3 worked as buffer agent in this bath with the pH value controlled between 2.0 and 5.2. The applied potential varied from 1.6V to 2.6V and the temperature was controlled at 60 °C as electrodepositing. Then, silver-nickel core-shell nanowires were obtained.

The microstructure and morphology were characterized by transmission electron microscopy (TEM, JEOL JEM-2010F) and scanning electron microscopy (SEM, LEO 1530). X-ray diffraction (XRD, PW1700) and energy dispersive spectra are employed to study the morphology and

chemical composition of silver-nickel core-shell nanowires. Atomic force microscope (AFM, SEIK SPA 300HV) and magnetic force microscope (MFM, SEIK SPA 300HV) imaging of nanowires exhibited surface morphology and magnetic domain state. The magnetic properties of silver-nickel core-shell nanowires were characterized using a vibrating sample magnetometer (VSM, DMS MODEL-1660).

3. Result and discussion

Silver nanowires grew up directly by electrodepositing into self-ordered nanopores AAO templates in acid silver ionic electrolyte with silver concentration from 5×10^{-3} to 2×10^{-2} M. The electrodeposition was carried out with constant current of about 4 mA under the voltage in the range of 0.6~1.5V. The scanning electron microscope (SEM) image of the wires are shown in Figure 5.1a. Most wires are about 200 nm in diameter and 23 μ m in length perpendicularly on 2 μ m thick bottom gold electrode within the pores, indicating all silver nanowires remain similar growth rate during the electrodeposition process so that more uniform and equal length silver nanowires can be obtained. The obtained nanowires were independently parallel with each other and the aspect ratio was estimated about 115. The gap among the synthesized nanowires was estimated from few nm to several 10 nm. The crystal structure of silver nanowires array were investigated by x-ray diffraction pattern as shown in Fig.5.1b. The x-ray diffraction pattern show that Ag face-centered cubic structure was indexed according to JCPDS card.

The formation of nickel coated layer or core-shell structure can be elucidated based on the reduction effect of nickel ions by electrodeposition. When the electron field was applied along the wires during deposition, the Ni^{2+} ions were first moved into the gap between nanowires and reduced on the surface of the silver nanowires. Furthermore, it was found that the surface condition and composition of the nanowires varied with electrodepositing time from 3 mins to 30 mins at 60 °C under an applied potential of 1.6 V, as shown in the SEM images of Fig.5.1c~g. In a short

period of electrodeposition, i.e., 3mins and 6mins, it was observed that surface condition of nanowires does not change obviously and remains smooth and flat, implying that the coated Ni layer is very uniform. A more detail micrograph of the Ag-Ni core-shell structure can be observed in the TEM images of Fig.5.2. The thickness of the nickel layer coated on silver nanowire surface was approximately to 15 nm. However, as it was electrodeposited for 30 min, Fig. 5.2c shows that the deposited Ni layer contains many 5~7nm nickel grains of different crystalline orientations. As the electrodeposition was kept for 30 min, as illustrated in Fig. 5.1f, many different type wires were formed and the surface becomes rougher. It could be deduced that several silver nanowires were covered to form capsular structure. In other words, the shell is nickel layer and the core contains several silver nanowires.

Moreover, as various electrodepositing potentials were applied, different structure could be found. Fig. 5.3a shows the SEM image of the Ag-Ni nanowires under an applied potential of 2.1V for 6min. The surface becomes rougher than that electrodeposited at 1.6 V. Besides, some small spherical nickel grains in the size of 50~100 nm were generated on the nanowire surface. As further increasing the potential to 2.6 V, more spherical particles were developed on the nanowire surface as shown in Fig. 5.3b. Energy dispersion x-ray spectra in Fig. 5.3c confirm the presence of pure spherical nickel corresponding to TEM image in Fig. 5.2c that it is a polycrystalline structure. The AFM image of the core-shell nanowires in Fig. 5.3d indicates the spherical nickel particles coated on the nanowires. Furthermore, MFM image in Fig. 5.3e exhibits many discrete magnetic nanoscale domain, as shown in bright contrast part, on silver nanowire surface.

On the other hand, Zhu reported that the easy magnetization axis is perpendicular to the membrane and enhanced coercivity has been observed for nanowire arrays of cobalt-nickel alloy (atom ratio Co:Ni = 2:1) by co-depositing the two corresponding materials into the nanometer sized pores of the porous alumina templates. Therefore, in this study,

The cobalt ions were added into the Watts bath by using $\text{CoSO}_4 \cdot 7\text{H}_2\text{O}$ and relative ion ratio of

$\text{Ni}^{2+}:\text{Co}^{2+}$ was adjusted to be 2:1 and 1:2. The electrodeposition was carried out at an applied potential of 1.6 V. It was observed that it exhibits a special structure, distinguished from that of pure nickel type. Fig. 5.4a show the irregular cobalt-nickel alloy with scrap-like shape obtained on silver nanowire surface in the condition of $\text{Ni}^{2+}:\text{Co}^{2+} = 2:1$. In contrast, for $\text{Ni}^{2+}:\text{Co}^{2+} = 1:2$, cobalt-nickel alloy sheets were formed on the surface of the Ag nanowires as shown in Fig. 4(b). The morphology transition from scrap to sheet that may be related to the change of crystal structure because nickel and cobalt belong to FCC and HCP, respectively. A detailed analysis and comparison is under investigation.

The magnetic properties of the core-shell nanowire arrays were investigated with vibrating sample magnetometer. Fig. 5.5 shows the hysteresis loop of the silver-nickel core-shell nanowires array measured at room temperature. The $H(\text{pl})$ and $H(\text{pd})$ represented external magnetic field parallel to nanowires and perpendicular to nanowires, respectively. While the silver nanowires was not yet coated with nickel, no clear hysteresis loop was detected as shown in Fig.5.5a, indicating that silver does not show magnetic characteristics.

In contrast, as the silver-nickel core-shell was fabricated under an applied potential of 1.6 V, distinct hysteresis loop (Fig.5.5b) appears and this responds again the formation of nickel crystalline structure. It was also found that both saturation magnetization (B_s) and remanence (B_r) of $H(\text{pl})$ were larger several times than those of $H(\text{pd})$. However, the coercive field (H_c) for both $H(\text{pl})$ and $H(\text{pd})$ orientations are similar about 180Oe. As compared with the H_c of pure Ni or Co nanowires (about 300~1300Oe), the core-shell array are more suitable for magnetic recording. As the silver-nickel core-shell was synthesized at a higher applied potential of 2.6 V, it was observed that the B_s and B_r values of both $H(\text{pl})$ and $H(\text{pd})$ are nearly equal as evidenced from Fig. 5(c). However, both hysteresis loops of the silver-nickel core-shell fabricated at 1.6V and 2.6V show different magnetic anisotropy and this indicates that the easily magnetized direction was parallel to the nanowires axis. In other words, nickel layer could generate larger magnetic domain in parallel

direction than that in perpendicular direction according to their structure. Therefore, it can be concluded that the strong magnetic anisotropy exists in silver-nickel core-shell structure.



5.4. Summary

A two-stage process including AAO process and electrodeposition was applied to fabricate the ordered silver- nickel core-shell nanowire arrays. Transmission electron microscopy (TEM) observation reveals that a 15 nm thick nickel film was coated on the surface of the silver nanowires with about 200 nm in diameter. The magnetic properties of silver nanowires with nickel coated can be much enhanced compared to that of pure silver one. The Magnetic Force Microscope (MFM) image of silver- nickel core-shell nanowires exhibits magnetic domain state. The hysteresis loop of the array exhibited strong magnetic anisotropy with the easily magnetized direction perpendicular to the core-shell nanowires axis.



5.5 References

- [5.1] C.A. Ross, M. Hwang, M. Shima, H.I. Smish, M. Farhoud, T.A. Savas, W. Schwarzacher, J. Parrochon, W. Escoffier, H. Neal Bertram, F.B. Humphrey, M. Redjidal, J. Magn. Magn. Mater. 249 (2002) 200.
- [5.2] A.J. Bennett, J.M. Xu, Appl. Phys. Lett. 82 (2003) 3304.
- [5.3] M. Shima, M. Hwang, C.A. Ross, J. App. Phys. 93 (2003) 3440.
- [5.4] X.Y. Yuan, G.S. Wu, T. Xie, Y. Lin, L.D. Zhang, Nanotechnology 15 (2004) 59.
- [5.5] X.Y. Yuan, G.S. Wu, T. Xie, Y. Lin, G.W. Meng, L.D. Zhang, Solid State Communications 130 (2004) 429–432.
- [5.6] R.M. White, R.M.H. New, R.F.W. Pease, IEEE Trans. Magn. 33(1996) 990.
- [5.7] D. Routkevitch, A.A. Tager, J. Haruyama, D. Almawlawi, M. Moskovits, J.M. Xu, IEEE Trans. Electron Devices 43(1996) 1646.
- [5.8] P.L. Lu, S.H. Charap, IEEE Trans. Magn. 30(1994) 4230.
- [5.9] S. Park, S. Kim, S. Lee, Z.G. Khim, K. Char, T. Hyeon, J. Am. Chem. Soc. 22 (2000) 8581.
- [5.10] A.J. Yin, J. Li, W. Jian, A.J. Bennett, J.M. Xu, Appl. Phys. Lett. 79 (2001) 1039.
- [5.11] Y.W. Wang, G.W. Meng, C.H. Ling, G.Z. Wang, L.D. Zhang, Chem. Phys. Lett. 343 (2001) 174.
- [5.12] W. Chen, S.L. Tang, M. Lu, Y.W. Du, J. Phys.: Condens. Matter 15 (2003) 4623.

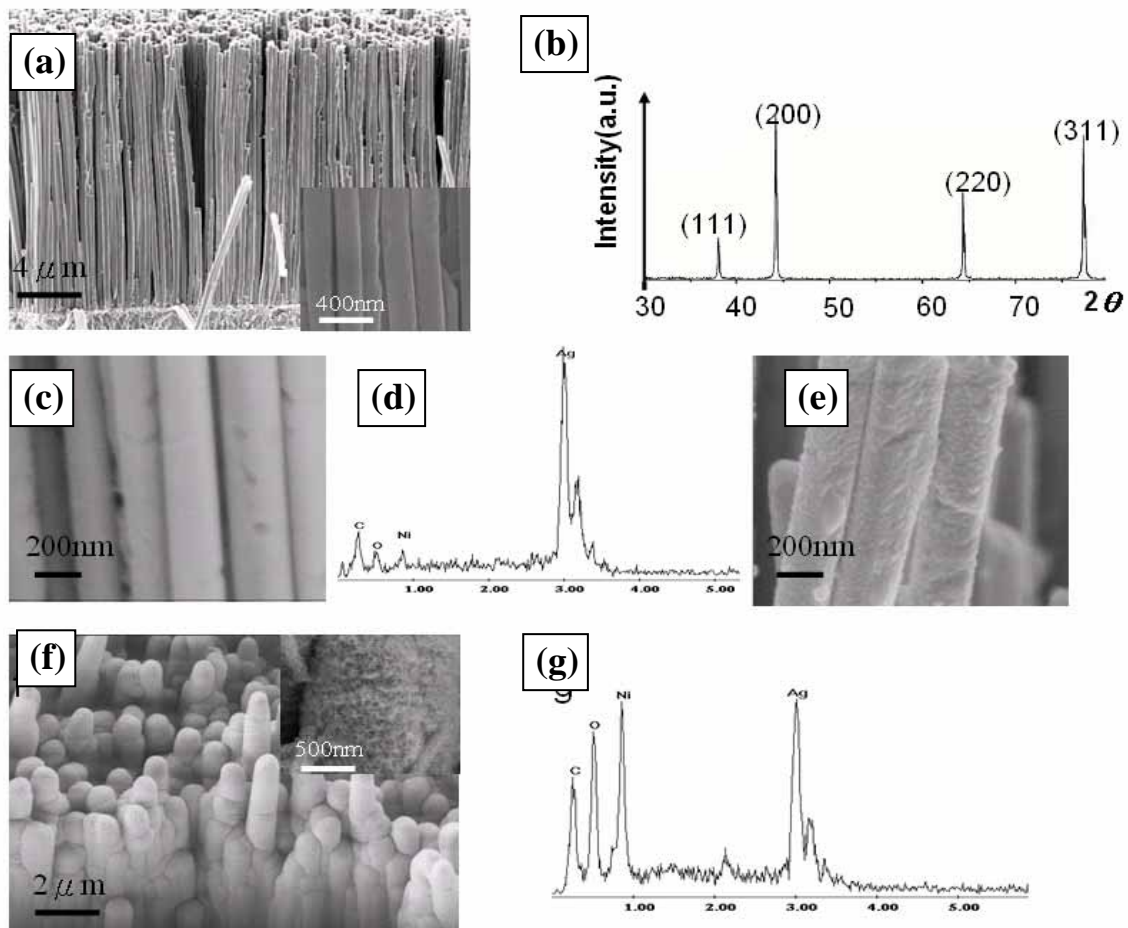


Fig.5.1(a).SEM image of silver nanowires array with 23 μm long and diameter of 200nm stood perpendicularly on 2 μm thick bottom gold electrode. Fig.5.1(b). XRD analysis of silver nanowires at Fig.5.1(a). Fig.5.1(c) and 5.1(d). Appearance, surface condition and composition of nanowires under nickel electrodepositing 1.6V and 3mins. Fig.5.1(e). Appearance and surface condition of nanowires under nickel electrodepositing 1.6V and 6mins. Fig.5.1(f) and 5.1(g). Appearance, surface condition and composition of nanowires under nickel electrodepositing 1.6V and 30mins.

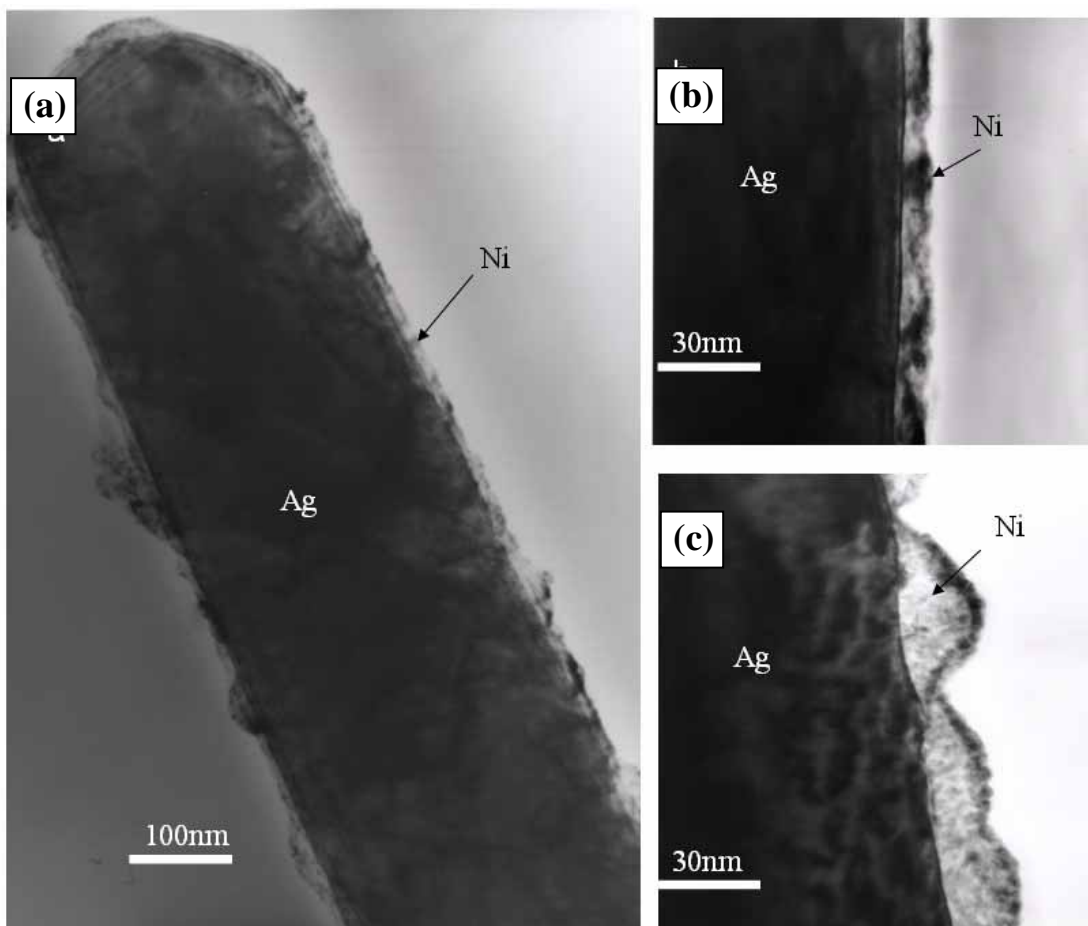


Fig.5.2a and 5.2b. TEM images of nickel electrodeposition time at 1.6V, 3mins. Fig.5.2c. TEM image of nickel electrodeposition time at 2.6V, 3mins.

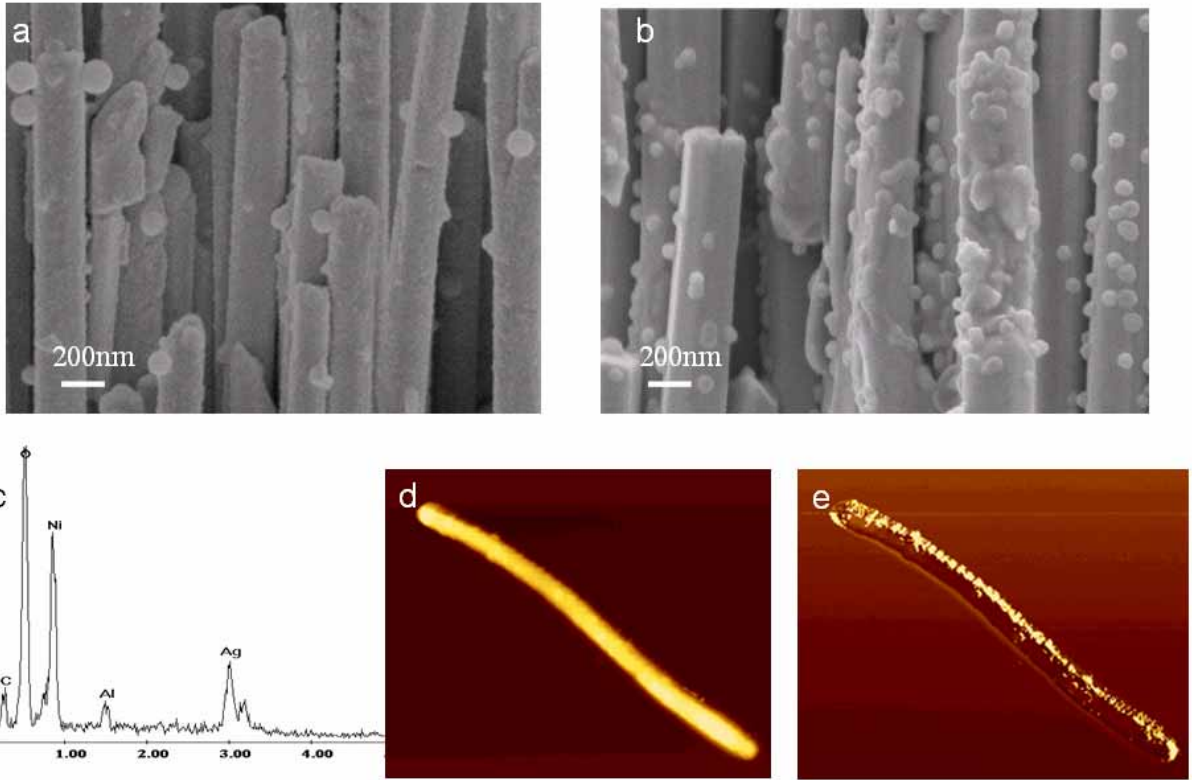


Fig. 5.3a. SEM image of nickel electrodeposition at 2.1V, 3mins. Fig.5.3b and 5.3c. SEM image and EDS analysis of nickel electrodeposition at 2.6V, 3mins. Fig.5.3d. SPM image of nickel electrodeposition at 2.6V, 3mins. Fig.5.3e. MFM image of nickel electrodeposition at 2.6V, 3mins.

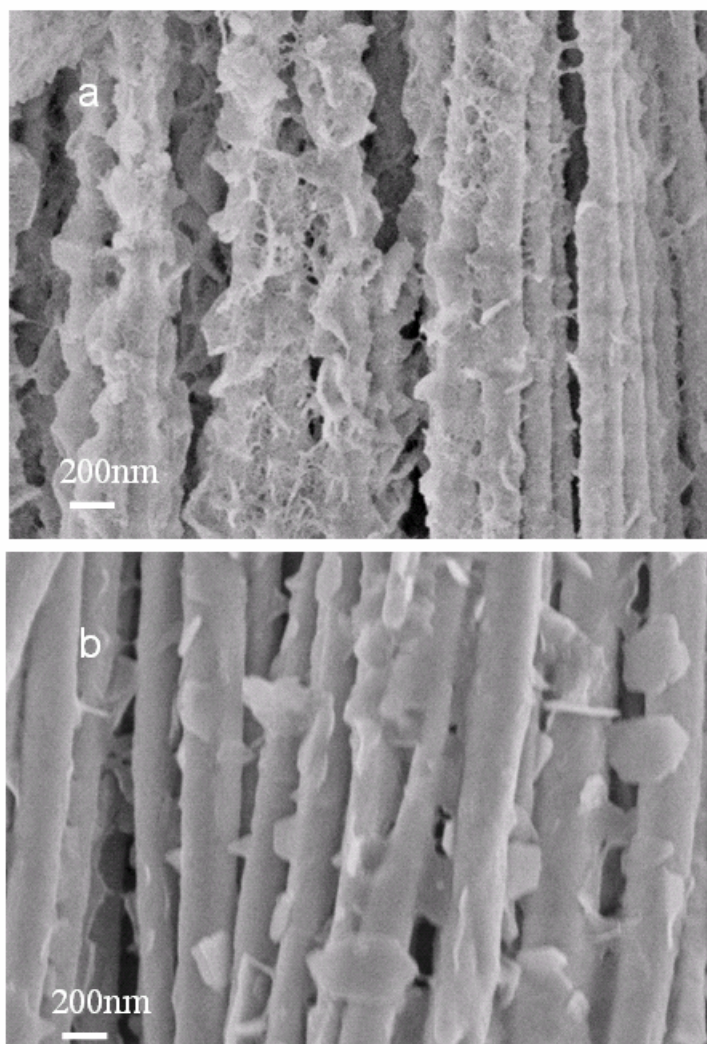


Fig.5.4a. SEM image of nickel-cobalt electrodeposition of $\text{Ni}^{2+}:\text{Co}^{2+} = 2:1$ at 2.1V, 3mins.

Fig.5.4b. SEM image of nickel-cobalt electrodeposition of $\text{Ni}^{2+}:\text{Co}^{2+} = 1:2$ at 2.1V, 3mins.

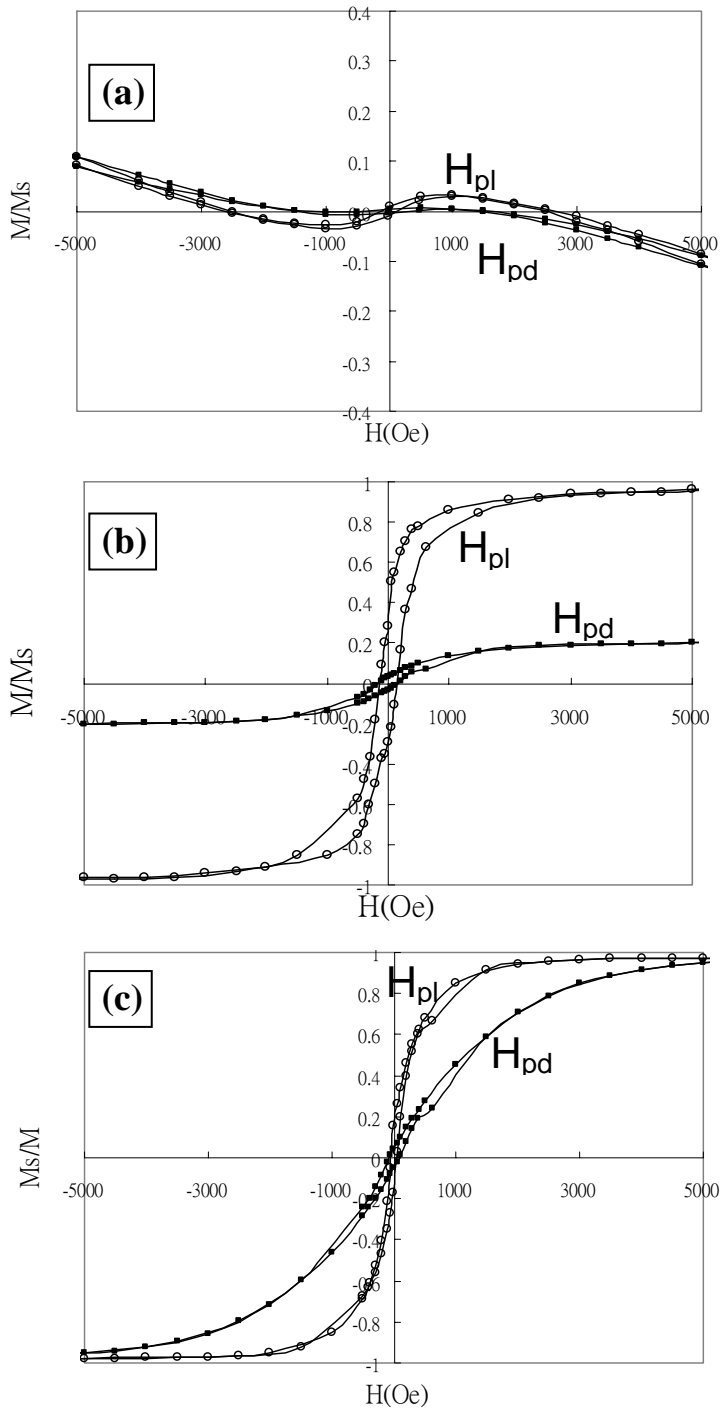


Fig.5.5a.The hysteresis loop of pure silver nanowire array measured at room temperature. Fig.5.5b.The hysteresis loop of silver-nickel core-shell nanowire array under nickel electrodeposition 1.6V and 3mins measured at room temperature. Fig.5.5c.The hysteresis loop of silver-nickel core-shell nanowire array under nickel electrodeposition 2.6V and 3mins measured at room temperature.

Chapter 6

Synthesis of Ag/Co magnetic nanowires with multi-layered structure

6.1 Introduction

Synthesis and study of nano materials attract much attention in recent years. One-dimensional nano structure including nanowire, nanorod, and nanotube has many amazing properties such as high density, high aspect ratio, low threshold voltage in field-emission and so on. On the other hand, the application of giant magnetoresistance (GMR) effect found in 2-D metallic multi-layers[6.1] has also been rigorously investigated for application in magnetic industry such as information storage and magnetic sensors[6.2~6-3]. The development of high-density perpendicular magnetic recording encourages the trend to investigate new kind of magnetic structure as the media. With the combination to take advantage of nanowires and multilayered structures, multilayered nanowires will show special characteristics compared to conventional magnetic materials.

For the synthesis of magnetic nanowires, we selected hard template containing nanometer-sized cylindrical pores to be the membrane and filled the pores with designed elemental segments. The most usually used templates for the template-synthesized metallic nanowire arrays [6.4] are ion track etched polycarbonate [6.5], anodic aluminum oxide (AAO)[6.6~6.7] and mica[6.8].

Electrochemical synthesis utilizing multi-bath or single bath method was usually adopted for depositing multi-metal segments into a template for its efficiency to prepare in large area, faster and cheaper processes[6.9]. Multi-bath electrodeposition was not considered in this research for the difficult of removing residual electrolyte containment in nanometer channels [6.10-6.11]. Recently, a few researches on magnetic multilayered nanowires, including Co/Cu [6.12~6.14], Cu/Ni [6.15], Au/Co [6.16], and Ag/Co [6.17] have been reported to adopt single-bath electrodeposition technique, that is to say two kinds of metallic ions coexisted in the electrolyte

during the deposition.

Due to the immiscibility of Ag and Co, Ag/Co multi-layer structure [6.18~6.19] should possess more distinguished interface than other sets of multi-layer magnets to benefit its industry application such as perpendicular storage.

In this research, we have developed a new electrolyte combining with stepped- potential controlled system for the synthesis of Ag/Co multilayered nanowires using a single-bath method, and it will also be interesting to compared magnetic hysteresis loops with these of pure Co nanowires.

6.2 Experimental

For the aim of obtaining multi-layer nanowires, the metal segments must be electrodeposited within the channel of AAO in sequence. After dissolving the template by NaOH, we can get the structure as schematically shown in Fig.6.1.

Commercially available nano-porous alumina membranes (AAO) with a thickness of 60 μ m and nominal pore diameters of 100nm (real range: 100 nm~200 nm) were used. The pore density of the AAO is 1×10^{10} and the pore inter-distance is about 50~70 nm which was confirmed by SEM analysis.

The electrolyte used in the experiment contained $\text{CH}_3\text{COONH}_4$, AgNO_3 , and $\text{CoSO}_4 \cdot 7\text{H}_2\text{O}$ developed by our group.

The major reactions are listed as follows:



The solubility product of Ag (CH_3COO), $K_{\text{sp}} = 2.3 \times 10^{-29}$, is much lower than that of Ag (NH_3) $^{2+}$ ($K_{\text{sp}} = 6.3 \times 10^{-8}$), so we observed the results of precipitation during the first few minutes when the binary-electrolyte system was prepared in $\text{CH}_3\text{COONH}_4$. Finally, the formation of complex ion Ag (NH_3) $^{2+}$ would gradually substitute

Ag (CH₃COO) to form clear electrolyte solution.

From the Nernst equation and kinetic theory, we know that the oxidation potentials and electro-deposition rate could be altered by altering the ion concentrations like Ag⁺ and Co²⁺,

$$E = E^0 - \frac{2.3 RT}{nF} \log Q$$

where Q is the reaction quotient; R is the gas constant (8.314 J mol⁻¹ K⁻¹); n is number of electrons involved in reaction; F is Faraday constant number (96485 C) and T is temperature (in K).

Cyclic-voltammetry and competing rate analysis of Ag/Co electrodeposition were applied to refine and optimize the electrodeposition conditions for the need of the single-bath electrodeposition. Cyclic-voltammetry was measured by CHI 604A electrochemical analyzer (CH Instrument, USA) with a scanning rate 0.1V/sec. Glassy carbon and Pt wire were used to be the working and counter electrodes respectively, while Ag/AgCl was used to be the reference electrode.

The automatic control system was then set up as shown in Fig.6.2 containing power supply such as a source-meter (Keithly 2400, Keithly USA) connected with a PC-based program to precisely control parameters of each step such as apply voltage, deposition time and so on, during the multi-step electrodeposition. Not only the step electrodeposition method was used but also a special design of potential segments was adopted such as decreasing segment time and off-potential time to overcome the charging problem.

Anodic aluminum oxide (AAO) was adopted to be the template for deposition to accommodate the post annealing process. DC sputtering of Au layer about 200 nm in thickness was used to be the conducting bottom layer of the AAO.

For the convenience of characterization, the AAO membrane was dissolved by 5% NaOH after electro-deposition. X-ray diffraction (XRD) and electron microscopy such as Field emission scanning electron microscope (FESEM) and transmission electron microscope (TEM) were applied to identify nanowires' composition and structure of nanowires. The magnetic behaviors of

Ag/Co multi-layered nanowires within AAO were also investigated by a vibrating sample magnetometer VSM.

6.3 Results and Analysis

6.3.1 Electrochemical analysis

Shown in Figs.6.3 to 6.5 are the results of cyclic-voltammetry and electrodeposition rates. It is observed that the concentration of $[Ag^+]$ concentration plays a more important role than is $[Co^{2+}]$. The difference in the electrodeposition rate at various voltages could be examined by the energy dispersive spectroscopy (EDS) analysis of the deposition layer and the result is shown in Fig. 6.5. With two different $[Ag^+]$ equal to 1 mM and 10 mM, respectively, the deposition of Co layer will not start until 0.7 V and the stacking rate of Ag and Co is drastically increased simultaneously with increasing voltage. When the applied voltage is high enough to force reduction of Co^{2+} ions, the ratio Co/Ag will be increased. However, electrolysis of water will also occur at higher voltage to break competition balance of the ions and the effective current density will be decreased hence the reduction of these two metal ions will be lowered. As a result, almost pure Co layer (Co= 98.83 %, Ag= 1.07 %) was resulted when applied voltage is 1.1 V vs. Ag/AgCl at the ratio concentration Co/Ag = 150. In cyclic-voltammetry analysis shown in Fig.6.6, the ion concentration ratio between $[Co^{2+}]$ and $[Ag^+]$ is Co/Ag = 150. Reduction of Ag^+ begins at about 0.3 V (vs. Ag/AgCl) and not until 0.8V does Co begin to appear.

Although pure Ag segment could be obtained when the applied voltage was below 0.6V, the deposition rate was however too slow to finish the experiments within acceptable time. And besides, the reduction effect will also strongly dissolve the cobalt layer deposited earlier; therefore, the design of deposition sequence of Co and Ag will be considered with two factors: applied potential and deposition time. Fig.6.7 shows the design of the whole deposition sequence. Co layer was deposited at 1.0 V and Ag layer 0.65 V which is close to the beginning point of Co reduction. The time segments were set that Co: 50 sec; Ag: 100 sec; off-potential time: 30 sec.

Within the nano-scale channel, immediate change in potential within a few seconds will accompany the problems such as charging resulting from electric double layer and concentration unbalance of these two metal ions near the interface of metal deposition layer and electrolyte. Applying stair-shape periodical potential design like fig.6.7 effectively avoids micro bubbles and over electrolyzing.

6.3.2 Structure analysis

With optimized deposition conditions and program setting as in Table 6.1, the Ag and Co segments were deposited in the AAO template in turn with 30 rounds. After dissolving AAO template with 5% NaOH solution for 30min, the micrographs result of nanowires was shown in Fig.6.8-6.10. We can easily observe that both Co (Fig. 6.8) and Ag (Fig. 6.9) nanowires have a homogenous diameter about 200 nm but the surface of Co nanowires was rougher for the main reason of stacking faults resulting from higher deposition rate.

Fig. 6.10 is the result of multi-layer nanowires observed by SEM which shows that the nanowires' surface morphology is not smooth but not rougher than the Co nanowire shown in Fig. 6.8. In the TEM bright field image Fig. 6.11.1, we can see obvious image contrast on the two nearby segments representing Ag and Co. The dark and shorter part was verified to contain mainly Ag. Both diffraction patterns and TEM-EDS were used to identify and confirm the segment's composition along the wire axis. It is successfully demonstrated that the multi-layer nanowires are composed of two kinds of segment: [Co] and [Ag₈₀Co₂₀] and are formed a homogenous and period structures. Moreover, it has an indistinct interface shown in TEM bright image. The result could be explained by our original stage-potential design in program and the appearance of Co-Ag⁺ interface redox reaction. To accurately increase and get clearer interface between two metals, annealing at 200°C for 1hr was done. Fig.6.11.2 shows the TEM image after annealing, revealing better and clearer segments of Co_{99.57}/Ag₁₀₀ multi-layer nanowires. Fitting with TEM pattern (Fig.6.11-(c)), it also shows the difference of crystalline degree that the Ag segment was deposited

with a single crystal structure and the Co segment is likely amorphous-polycrystalline structure. XRD analysis (Fig. 6. 12) of the $\text{Co}_{99.57}/\text{Ag}_{100}$ multi-layer nanowires shows Ag with (111), (220) and (222) peaks while Co layer with f.c.c structure accompanying with (100), (002), and (101) peaks.

6.3.3 Magnetic analysis

For the storage application, it is interesting to compare the magnetic hysteresis loops between pure Co nanowire and Ag/Co multilayered nanowires. In the Fig. 6.13 and Fig. 6.14, the measurement of hysteresis loop respectively proceed upon magnetic field parallel and perpendicular to the nanowire axis along nanowires. Pure Co nanowire has an H_c of 300Oe when the measuring field is parallel to the long axis of the nanowires comparing to H_c 225 Oe upon a perpendicular field. Ag/Co multi-layer nanowires have almost the same coercivity H_c 210 Oe but more obvious magnetic anisotropy and lower saturation magnetization (M_s) than do pure Co nanowires. For the pure Co nanowire, axis along the nanowire is the easier orientation (easy axis). For the Ag/Co multilayered nanowires, the easy axis changes to the orientation perpendicular to the axis of the wire.

6.4 Summary

In this study, accompanying with electrochemical experiments and analysis, we successfully worked out the optimized conditions to synthesize Ag/Co multi-layer nanowires, 100nm diameter, respectively by a single-bath electrodeposition using the AAO template. The segment composition of the nanowires was $[\text{Co}]/ [\text{Ag}_{80}\text{Co}_{20}]$ that is not stable and homogeneous all through the whole nanowire. By annealing process, we could attain better results of almost pure Co/Ag nanowires $\text{Co}_{99.57}/\text{Ag}_{100}$ which shows different magnetic properties such as more obvious anisotropy and change of easy axis compared with those of pure Co nanowires.

6.5. References

- [6.1] M.N. Baibich, J.M. Broto, A. Fert, F. Nguyen Van Dau, F. Petroff, P. Etienne, G. Creuzet, A. Friederich, J. Chazelas. *Phys. Rev. Lett.* 61 (1988) 2472.
- [6.2] T. Valet, A. Fert, *Phys. Rev. B* (1993), 48, 7099.
- [6.3] L. Piraux, J.M. George, J.F. Despres, C. Leory, E. Ferain, R. Legras, K. Ounadjela, A. Fert, *Appl. Phys. Lett.* (1994), 65, 2484.
- [6.4] C.R. Martin, *Science* 266 (1994) 1961.
- [6.5] K. Ounadjela, R. Ferre, L. Louail, J. M. George, and J. L. Maurice, *J. Appl. Phys.* 81, 5455 (1997).
- [6.6] D. Aimawiawi, N. Coombs, M. Moskovits, *J. Appl. Phys.* (1991), 70, 4421.
- [6.7] H. Schwanbeck, U. Schmidt, *Electrochimica Acta.* 45 (2000) 4389–4398.
- [6.8] L. Sun, C. L. Chien, P.C. Searson, *J. Mater. Sci.* (2000), 35, 1097.
- [6.9] W. Swarzacher, D.S. Lashmore, *IEEE Trans. Magn.* 32 (1996) 3133.
- [6.10] P. Leisner, C.B. Nielsen, P.T. Tang, T.C. Dorge, P. Moller, *J. Mater. Proc. Tech.* 58 (1996) 39-44.
- [6.11] P.E. Bradley, D. Landolt, *Electrochim. Acta.* 45 (1999) 1077.
- [6.12] A. Blondel, B. Doudin, J. –Ph. Ansermet, *J. Magn. Mater.* 165 (1997) 34-37.
- [6.13] E. Gomez, A. Labarta, A. Llorente, E. Valle's. *Surface and Coatings Technology*, 153 (2002) 261-266.
- [6.14] Mingliang Tian, Jinguo Wang, James Kurtz, Thomas E. Mallouk, and M. H. W. Chan. *Nano Lett.* 2003; 3(7); 919-923
- [6.15] Yu-Guo Guo, Li-Jun Wan, Chuan-Feng Zhu, De-Liang Yang, Dong-Min Chen, and Chun-Li Bai, *Chem. Mater.*, 15, (2003), 664-667.
- [6.16] Sima Valizadeh, Lars Hultman, Jean-Marie George, Peter Leisner, *Advanced Functional Materials*, 12 (11-12) (2002), 766-772

- [6.17] S. Valizadeh, J.M. George , P. Leisner , L. Hultman, *Thin Solid Films* 402 (2002) 262-271.
- [6.18] S. Kenane, E. Chainet, B. Nguyen, A. Kadri, N. Benbrahim, J. Voiron, *Electrochem. Commun.* 4 (2002) 167–170.
- [6.19] S. Valizadeh, G. Holmbom, P. Leisner, *Surface and Coatings Technology* 105 (1998) 213–217.



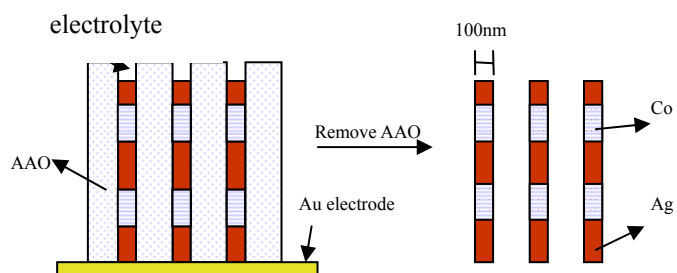


Fig .6.1 Multi-layer nanowires structure

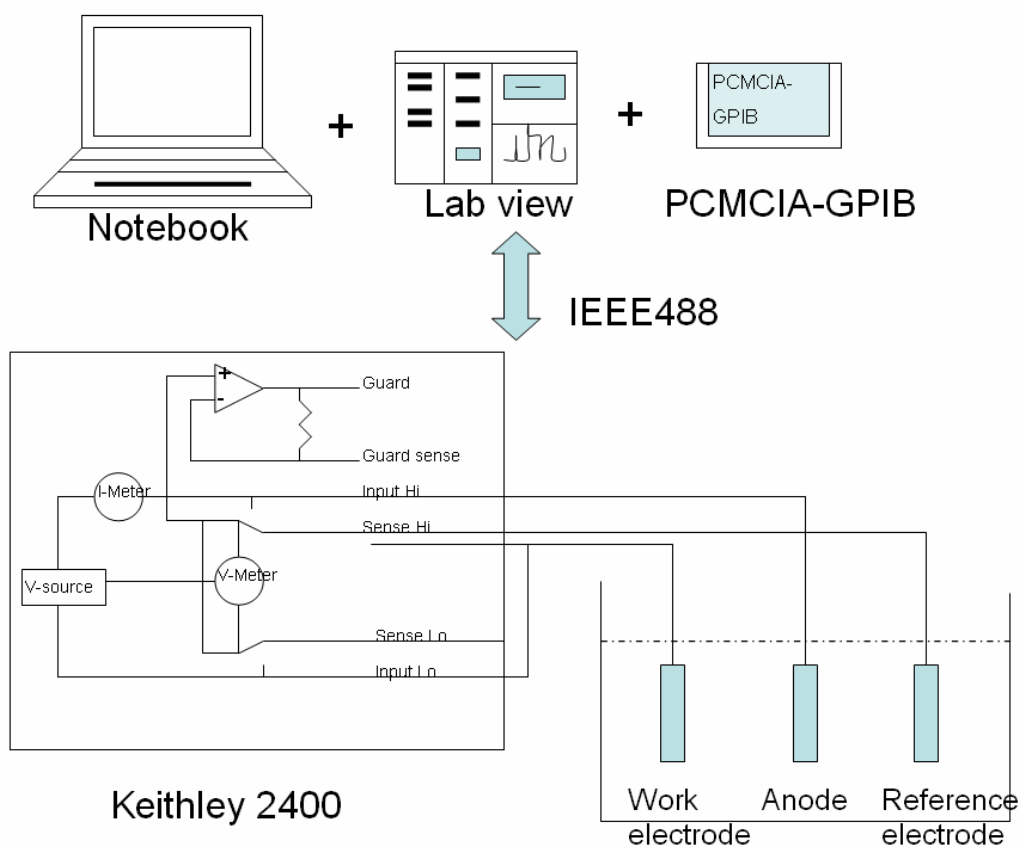


Fig.6.2 The set-up of electro-deposition system, Pt wire was used to be the working

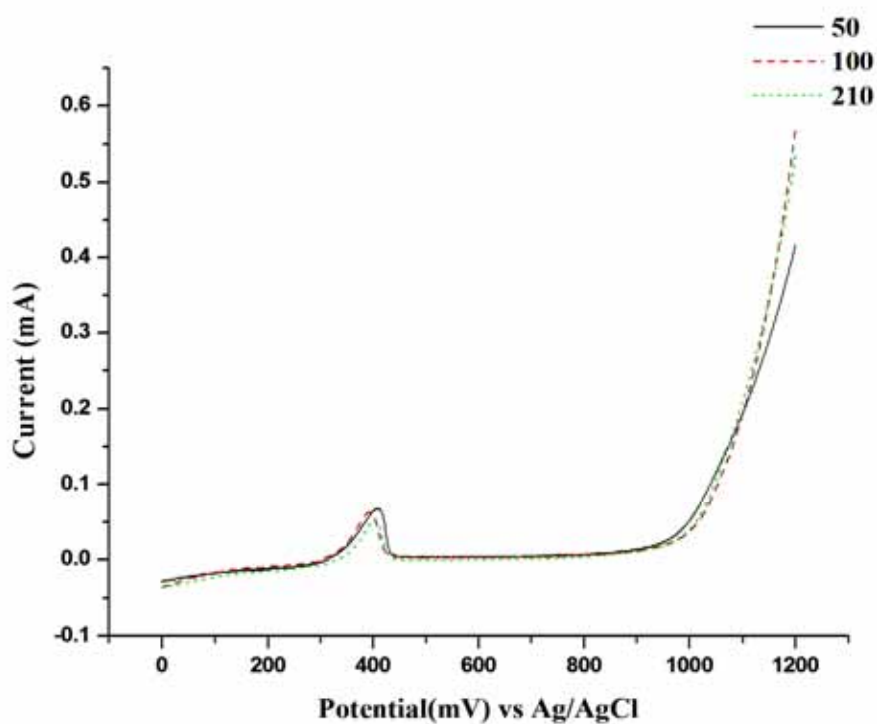


Fig. 6.3 Cyclic-voltammetry analysis by altering $[Co^{2+}] / [Ag^+]$ ratio 50, 100, 210.

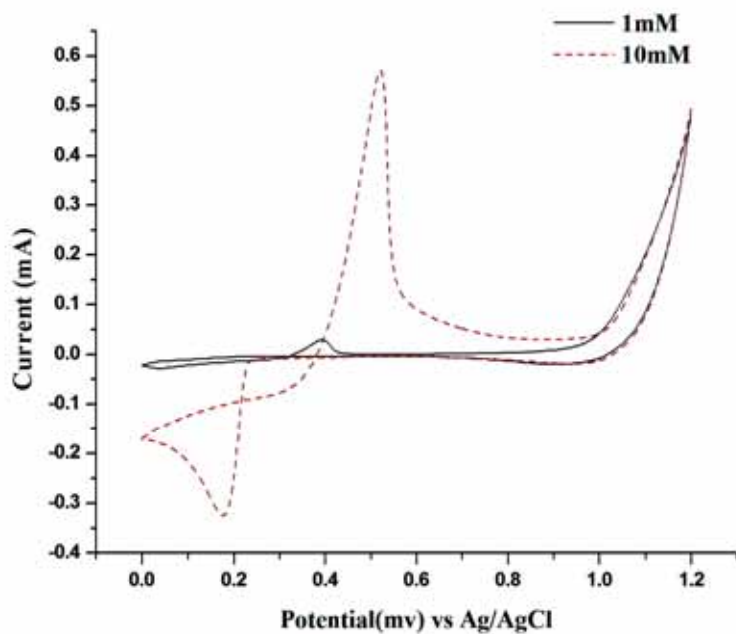


Fig.6.4 Cyclic-voltammetry analysis by altering $[Ag^+]$ with constant $[Co^{2+}] = 0.15M$

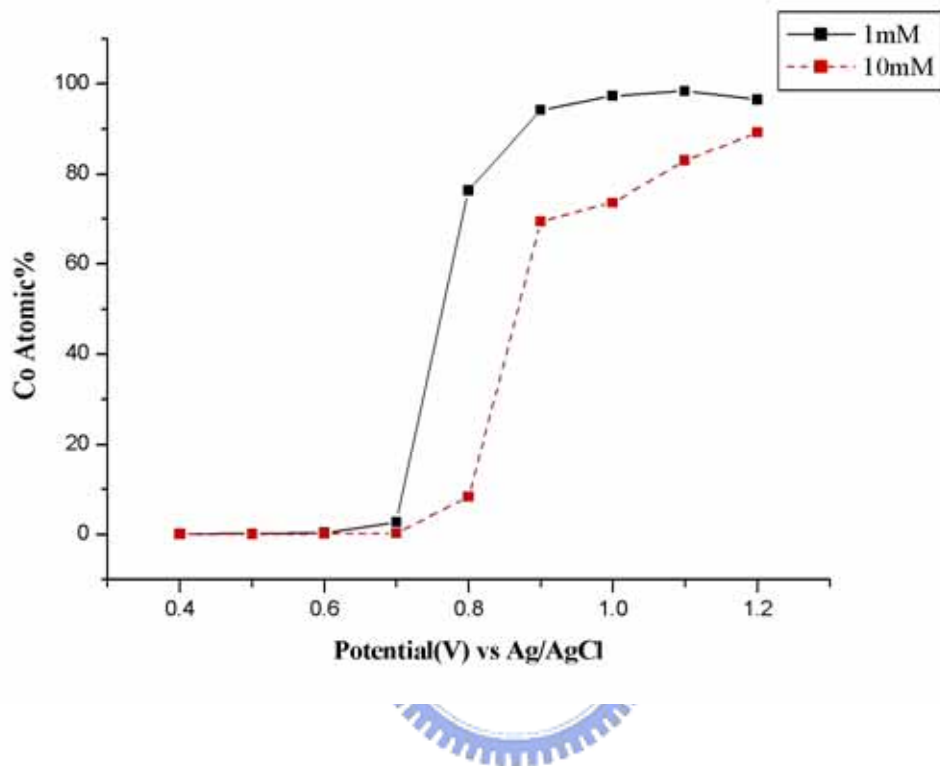


Fig.6.5 Electrodeposition rate upon altering $[Ag^+]$ with constant $[Co^{2+}] = 0.15 M$

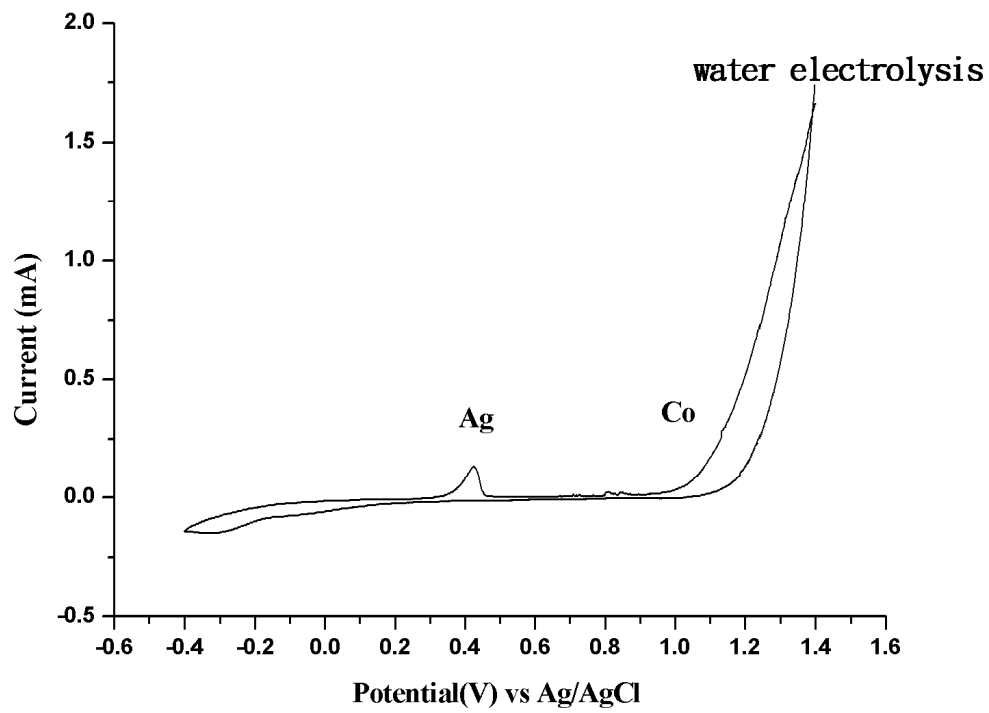


Fig.6.6 Cyclic-voltammetry analysis of the solution with $[\text{Co}^{2+}] / [\text{Ag}^+] = 150$

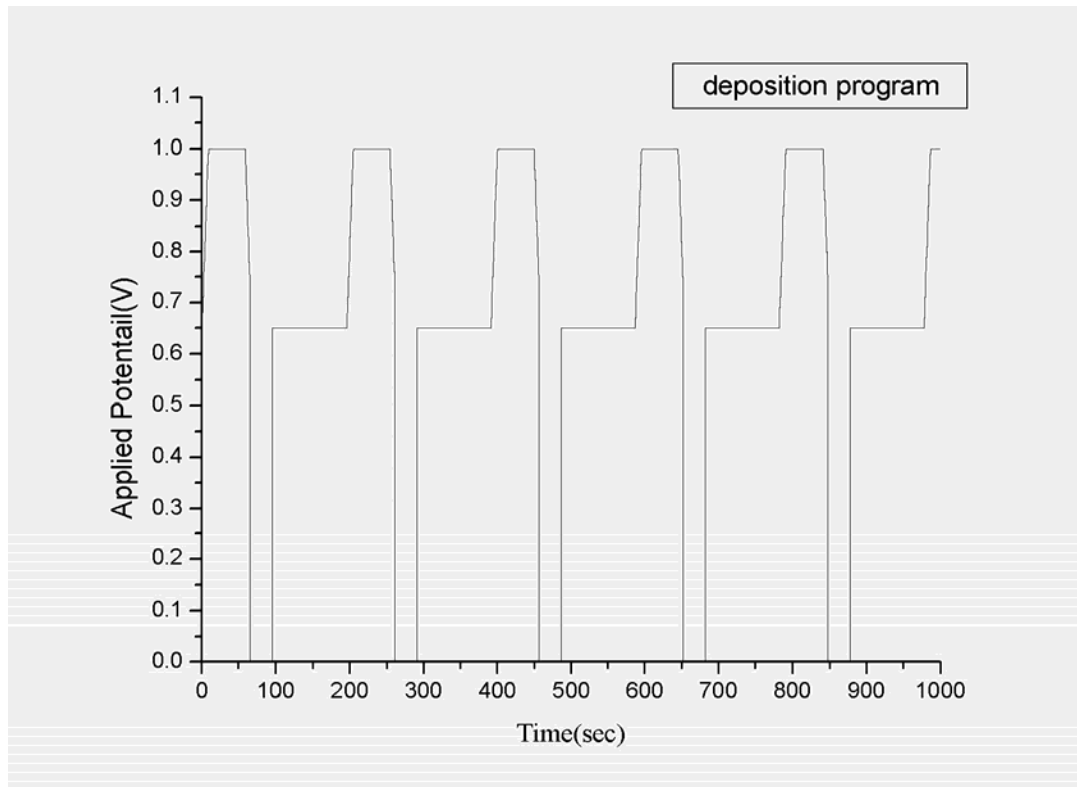


Fig.6.7 Design of the whole deposition sequence

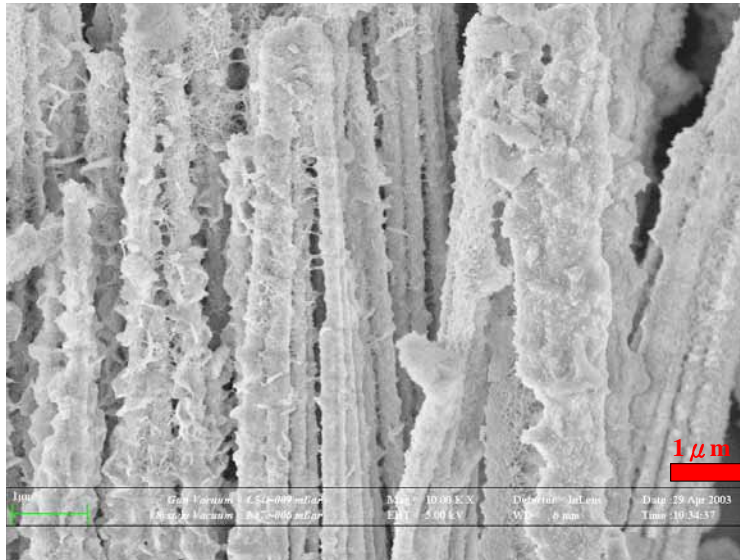


Fig. 6.8 SEM image of pure Co nanowires deposited at 1V

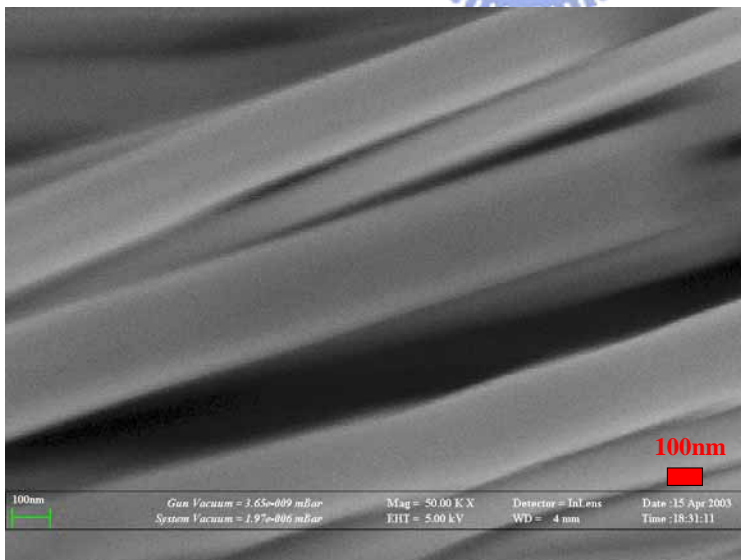


Fig.6.9 SEM image of pure Ag nanowires deposited at 0.65V

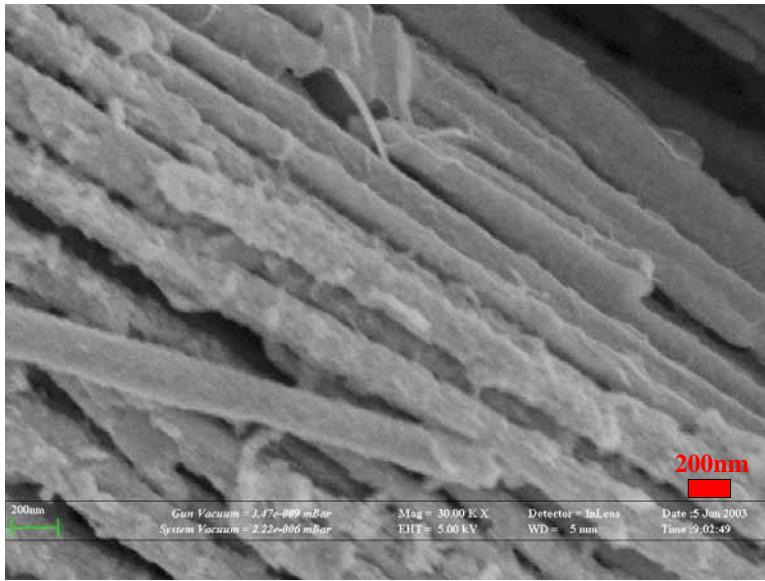


Fig.6.10 SEM image of Ag/Co multi-layer nanowires deposited with parameters shown in Table 6.1

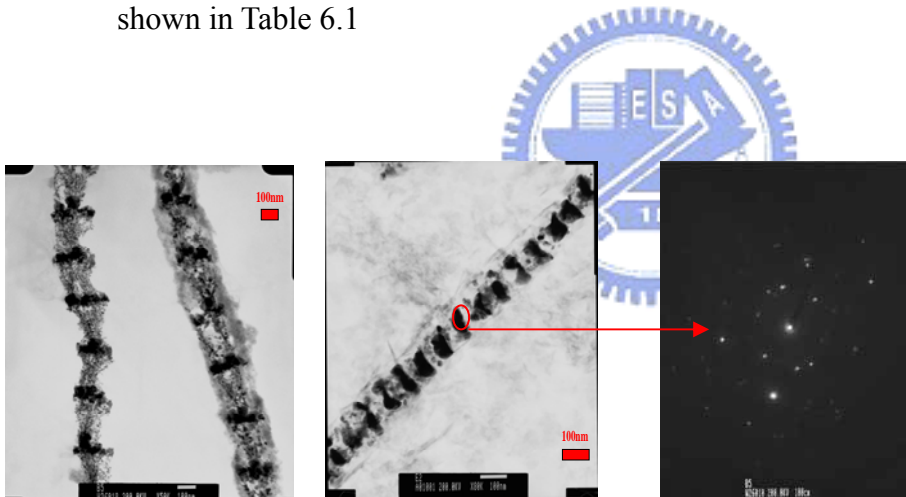


Fig. 6.11-(a)

Fig. 6.11-(b)

Fig. 6.11-(c)

Fig.6.11-(a) TEM bright-field image of $\{[Co]/[Ag_{80}Co_{20}]\}_{30}$ multilayered nanowires, (b) after annealing at 200°C 1hr, (c) Selected area diffraction pattern of $[Co]/[Ag_{80}Co_{20}]$ multilayered nanowires.

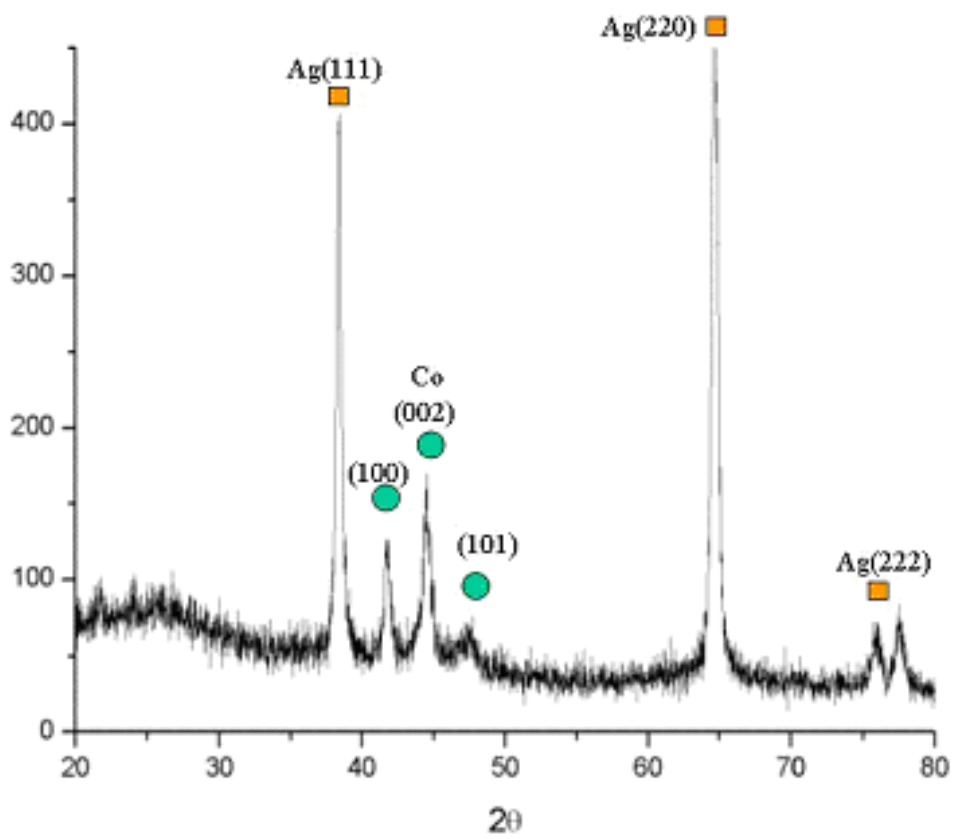


Fig. 6.12 XRD analysis of Co/Ag multilayered nanowires

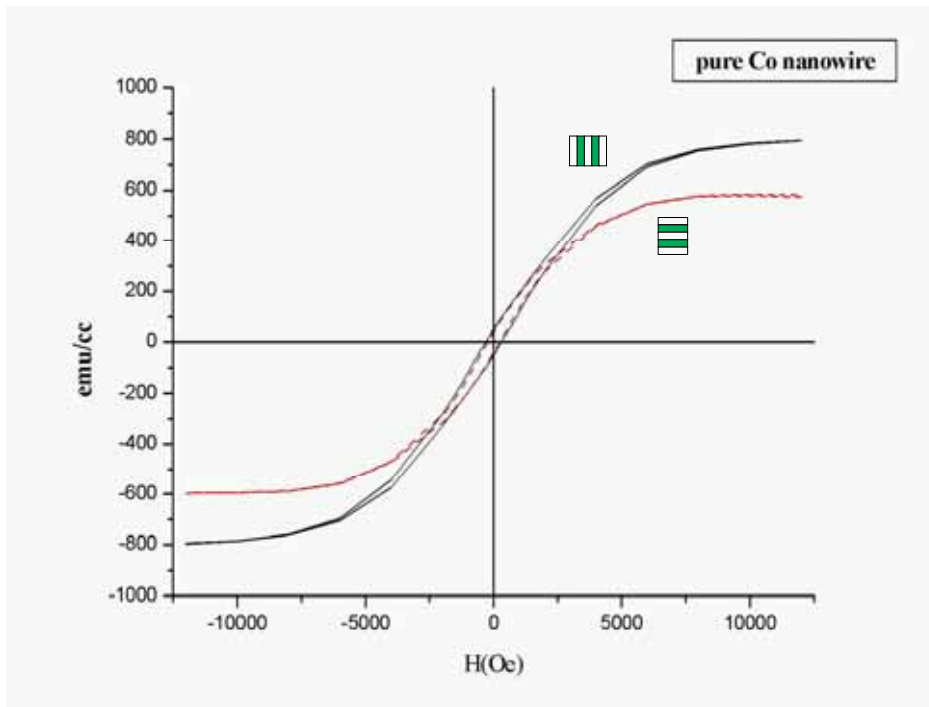


Fig. 6.13 Magnetic hysteresis of pure Co nanowire along two vertical axes

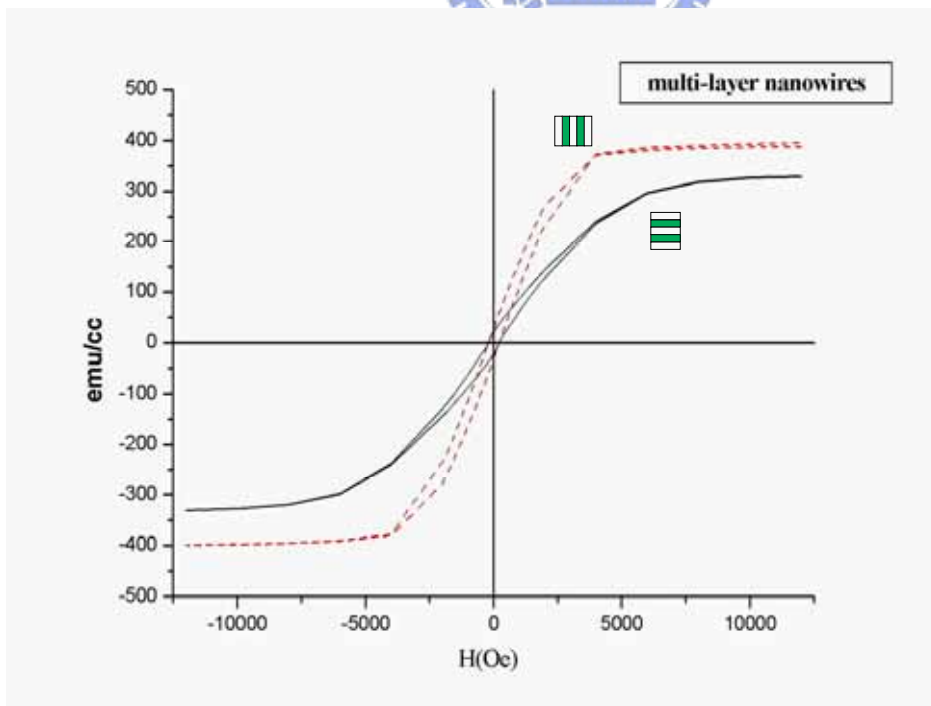


Fig.

6.14 Magnetic hysteresis of $\text{Co}_{99.57}/\text{Ag}_{100}$ multilayered nanowires along two vertical axes

Table 6.1 Parameters of Ag/Co multi-layer nanowires deposited.

	Concentration(M)	Potential	Segment time
CoSO ₄ · 7H ₂ O	0.15	1.0V	100sec
AgNO ₃	0.005	0.65V	200sec
CH ₃ COONH ₄	0.4	Off	Off time:30sec



Chapter 7

Solar cell devices based on Cu-phthalocyanine / nanostructured ZnO hybrid film

7.1. Introduction

Organic-inorganic hybrids for photovoltaic cell have been receiving attention recently. It has become the major purposes to enhance the conversion efficiency of the photovoltaic devices and at same time to reduce production costs. Semiconductor oxide materials in conjunction with photo sensitive organic dyes have extended hybrid materials sensitivity into the visible regions. ZnO is a semiconductor material and possesses special characteristic including high electron mobility[7.1], low temperature synthesis, and the potential for controlling the morphology through simple solution processing. In the past few years, hybrid devices including ZnO/ZnPc[7.2], ZnO/merocyanines[7.3], ZnO/P3HT[7.4] and ZnO/CuPc[7.5~7.7]etc, have been constantly investigated. The obtained hybrid ZnO/ dye devices have an overall efficiency of approximately 0.2-2% and fill factor of greater than 0.3-0.6 and 5~16% of the external quantum efficiency that could be attributed to the increased ZnO /dye interfacial area due to recombination behaviors of high surface ZnO structure. However, the conversion efficiency of these devices have been limited because of difficultly controllable particle boundary, inorganic/dye degradation and high production costs. In recent years, ZnO nanorods or nanowires uniformly grown perpendicular[7.8~7.9] to the substrate are particularly investigated because of slow charge recombination between aligned nanowires and dyes that results in significant improvements in device performance.

In this study, three types of ZnO nanostructures including vertically aligned nanorods, randomly oriented nanorods and nanoparticles were selected to develop p-n junction devices with Cu-phthalocyanine. In addition, Al-doping into ZnO nanostructure was also studied because it causes the absorption spectra to transmit from UV region to visible light and enhances total

absorption efficiency. Moreover, scanning electron microscopy, transient absorption spectroscopy, and photovoltaic device measurements were also used to examine the morphology, charge separation, recombination behavior and device performance of these three types ZnO/CuPc.

7.2. Experimental

0.1M zinc nitrate hydrate and aluminum nitrate hydrate solution were blended and precipitated by ammonia. Pure ZnO 30~60nm nanoparticles and 2~8% Al₂O₃ doping ZnO nanoparticles were synthesized by annealing the precipitates at 700°C in air. The ZnO nanoparticles and Cu-phthalocyanine were mixed in the ratio of 1:2 by weight using methanol as a solvent and remained at 80 °C for 24 h. The hybrid device having structure ITO/ZnO:Cu-phthalocyanine /Al was fabricated by spinning coating the mixture of ZnO:Cu-phthalocyanine over ITO coated glass substrate, and then metal Al was deposited by sputtering. On the other hand, methenamine (C₆H₁₂N₄) and zinc nitrate hexahydrate (Zn(NO₃)₂ · 6H₂O) were used for preparing the solution to grow vertically aligned and randomly ZnO nanorods. The ITO/ Glass substrates were buffered with ZnO film by sputtering. The substrates were then placed in the aqueous solution of 0.01 M zinc nitrate hydrate at 75°C for 10 h to grow the ZnO nanowires. After that, Cu-phthalocyanine solution was coated on the surface of ZnO nanorods and subsequently filled in the intervals of the nanorods. After metal Al was deposited, the hybrid device with ITO/ZnO: Cu-phthalocyanine /Al was completely prepared.

The structural characteristics of the ZnO nanorods were analyzed by scanning electron microscopy (SEM/EDX, JEOL-6500F). The crystal structure was determined using X-ray diffraction (XRD) with CuK α radiation. The absorption spectrum and photon to electron conversion efficiencies test of the device was recorded using fluorescence spectrophotometer. Current–voltage characteristics were investigated using Keithley electrometer (2400) in dark and

under illumination simulated sunlight under AM1.5 ($10\text{mW}/\text{cm}^2$).

7.3 Results and discussion

Fig.7.1 reveals three types of ZnO nanostructures including vertically aligned nanorods, randomly oriented nanorods and nanoparticles. In Fig.7.1a, ZnO nanorods grown on glass/100nm indium tin oxide/ dense ZnO thin film substrate were and intercalated by Cu-phthalocyanine to form Cu-phthalocyanine/nanorod ZnO hybrid device. On the other hand, Fig.7.1b and 7.1c show the SEM image of randomly oriented nanorods and nanoparticles, respectively, that were blended with Cu-phthalocyanine solution and coated on the same glass/100nm indium tin oxide substrate. The nanoparticles have sizes in the range of 30~60 nm but the nanorods are not very uniform in diameter (30-100 nm). Here, organic Cu-phthalocyanine could connect these nanoparticles or nanorods to generate film structure with 0.5~3 μm thickness.

Fig. 7.2 shows X-ray diffraction patterns of three-type ZnO nanostructures. The peak positions in the XRD patterns can be consistent with each other, but the relative peak intensity of aligned nanorods is different from that of the others. The (002) peak of aligned nanorods is relatively stronger than other peaks. This indicates ZnO nanorods were grown along with the preferred orientation (002). In addition, it was also observed that the sample of 5mol% Al_2O_3 doped into ZnO (ZnO:Al) shows similar X-ray diffraction pattern from pure ZnO nanoparticles, indicating that 5mol% Al_2O_3 could be dissolved into wurtzite phase ZnO to form a solid solution.

Pure ZnO is an n-type semiconductor and has band gap energy of 3.27 eV matching to wavelength about 379 nm. Therefore, pure ZnO strongly absorbs light in UV region and is transparent for visible light. Cu-phthalocyanine has been used as photoelectrochemical sensitive material of wide band gap nanocrystalline and p-type semiconductor. It reveals strong π - π^* transition in visible region and is easily to form heterjunction with ZnO. Fig.7.3 shows the strong absorption of pure ZnO that appears in the range of 250~460nm, and at same time Cu-phthalocyanine also exhibits broad absorption behavior of 440-700nm with a maximum

absorption at 630nm. While partial Al was doped into ZnO, the maximum absorption would be transmitted slightly from UV region to visible light which is attributed to the reduction of band gap of ZnO to ZnO:Al. The absorption was shifted to be around 20nm and 40nm while 2mol% and 5mol% Al₂O₃ doping, respectively. However, it was found that no more shift to long wavelength was observed for the sample with 8mol% Al₂O₃ that could indicate the critical point of about 500nm. Furthermore, ZnO nanorods appear stronger absorption shift than nanoparticles. It could be attributed to the uniform structure, less grain boundary and easily electron jumping along c-axis aligned nanorods. The phenomena of absorption shifts from UV to visible light will simultaneously improve absorb intensity of solar energy to cause more charge generation.

Fig.7.4 shows the current–voltage behavior of the three-type hybrid devices in dark and illumination under simulated sunlight AM1.5 (10mW/cm²). The performance of the ITO/ZnO nanoparticles with Cu-phthalocyanine coated /metal Al device was determined and values for the open circuit voltage(Voc), short circuit current density (Jsc), fill factor(F.F.) and efficiency were measured to be about 0.91V, 0.56mA/cm², 0.46, and 0.23%, respectively, as seen in Fig.7.4a. The combination of schottky barrier and ohmic contact at Al–CuPc and ITO–CuPc can be detected in this device, respectively, and p-type semiconductivity of CuPc could cause rectification effect. The hybrid device fabricated from randomly oriented ZnO nanorods showed similar results and the values for Voc, Jsc, F.F. and efficiency were 0.89 mV, 0.55mA/ cm², 0.43, and 0.21%, respectively. However, it was noted that vertically aligned ZnO nanorods device shows comparatively excellent characteristics. The obtained values for Voc, Jsc, F.F. and efficiency were 0.56V, 5.3mA/ cm², 0.44, and 1.32%, respectively. The excellent performance of aligned ZnO nanorods could be attributed to the influence of morphology, connectivity between interfaces, trap density and charge recombination kinetics. Purniamoorthy etc.[7.4,7.10] indicated the structures containing vertically aligned ZnO nanowires or nanorods would lead to easier escape for electrons from interfacial recombination sites and charge between hybrid materials would cause slower recombination by 2 orders of magnitude at low excitation densities.

.Fig.7.5 shows an photo to electron conversion of the hybrid devices with 5%Al₂O₃-doped ZnO with nanoparticles and vertically ZnO aligned nanorods. The maximum incident photon to electron conversion is 0.036mA and appears at around 500 nm. The obtained energy conversion efficiencies under simulated sunlight AM1.5 (10mW/cm²) in aligned ZnO is estimated about 1.32%. In contrast, Vertically aligned ZnO nanorods device can be seen that the maximum value for ZnO nanoparticles device is 0.027mA and appears at around 470 nm. In addition, the aligned ZnO nanorods device exhibit a broader conversion than other two types which is quite consistent with the shift of the absorption as shown in Fig.7.3.



7.4 Summary

The heterojunction photovoltaic devices comprising hybrid p-type organic Cu-phthalocyanine and inorganic vertically aligned ZnO nanorods of n-type semiconductor were fabricated. The strong absorption of ZnO layer appears in range 250~460nm wavelength. Meanwhile, Cu-phthalocyanine exhibits broad absorption behavior of 440-700nm having an absorption maximum at 630nm. Charge recombination in vertically aligned ZnO rods type was more efficient than the conventional randomly oriented rods and nanoparticles. The maximum value of incident photon to electron conversion in aligned ZnO is 0.036mA and lie at around 500 nm and energy conversion efficiencies under simulated sunlight AM1.5 ($10\text{mW}/\text{cm}^2$) of 1.32%.



7.5 Reference:

- [7.1] Makino T.; Segawa Y., Tsukazaki A., Ohtomo A. and Kawasaki M., *Condensed. Matter* 2005, 1-4, 0507009.
- [7.2] Yuki Yoshida , Makoto Nakamura, Senku Tanaka , Ichiro Hiromitsu, Yasuhisa Fujita, Katsumi and Yoshino, *Synthetic Metals*, 156 (2006) 1213–1217
- [7.3] K. Kudo and T. Moriizumi, *Jpn. J. Appl. Phy.* 19 (1980) 2683.
- [7.4] Punniamoorthy Ravirajan, Ana M. Peiro, Mohammad K. Nazeeruddin, Michael Graetzel, Donal D. C. Bradley, James R. Durrant, and Jenny Nelson, *J. Phys. Chem. B* 2006, 110, 7635-7639
- [7.5] G.D. Sharma, Raj Kumar, Shailendra Kumar Sharma and M.S. Roy, *Solar Energy Materials & Solar Cells* 90 (2006) 933–943
- [7.6] F. Cao, G. Oskam and P.C. Searson, *J. Phys. Chem.* 99 (1995) 1707.
- [7.7] U. Bach, D. Lupo, P. Comte, J.E. Moser, F. Weissortel, J. Salbeck, H. Spreitzer and M. Gratzel., *Nature* 395 (1998) 583
- [7.8] Yamabi S. and Imai H., *J. Mater. Chem.* 2002, 12, 3773.
- [7.9] Law M., Greene L. E., Johnson J. C., Saykally R., Yang P., *Nat. Mater.* 2005, 4, 455.
- [7.10] Liu Y., Coakley K. M. and McGehee M. D. *Proc. SPIE Int. Soc. Opt. Eng.* 2004, 5215, 187.

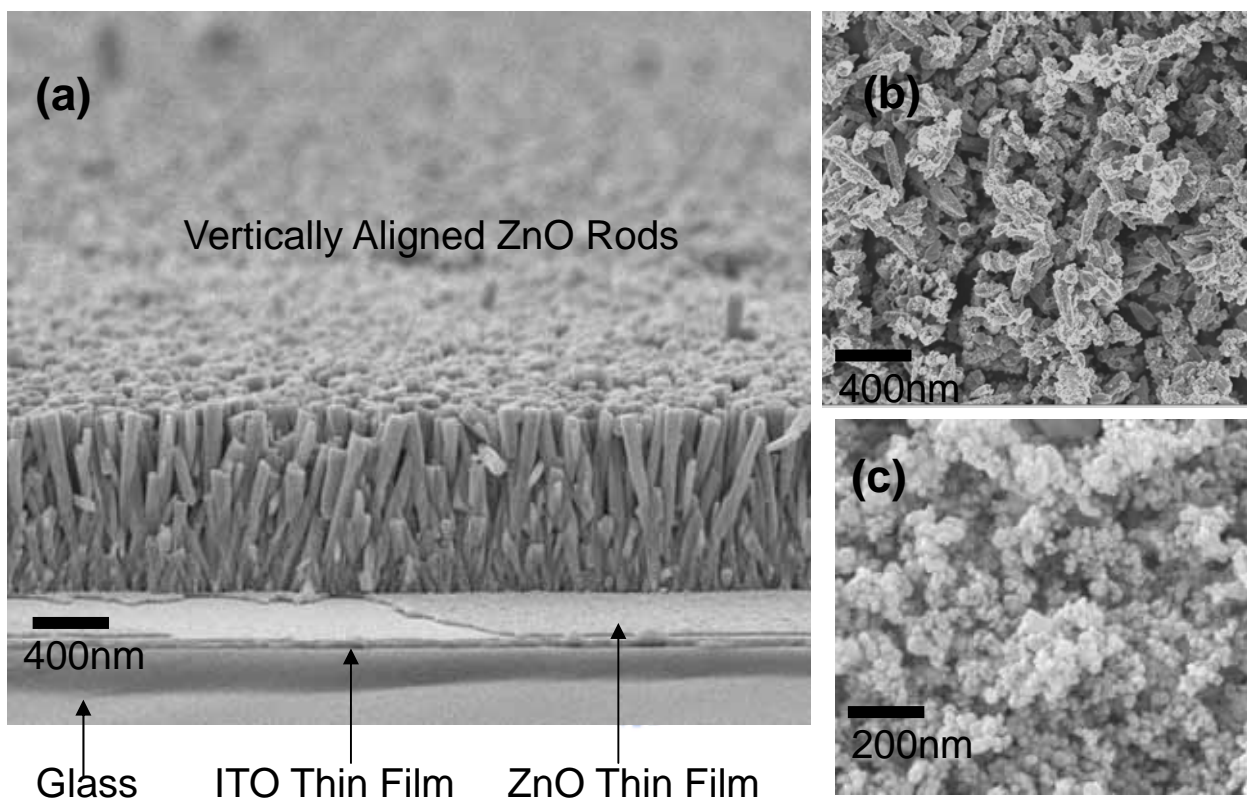


Fig.7.1.a Vertically aligned ZnO nanorods, (b) randomly oriented ZnO nanorods and (c) ZnO nanoparticles grown on glass/100nm indium tin oxide/ dense ZnO thin film substrates.

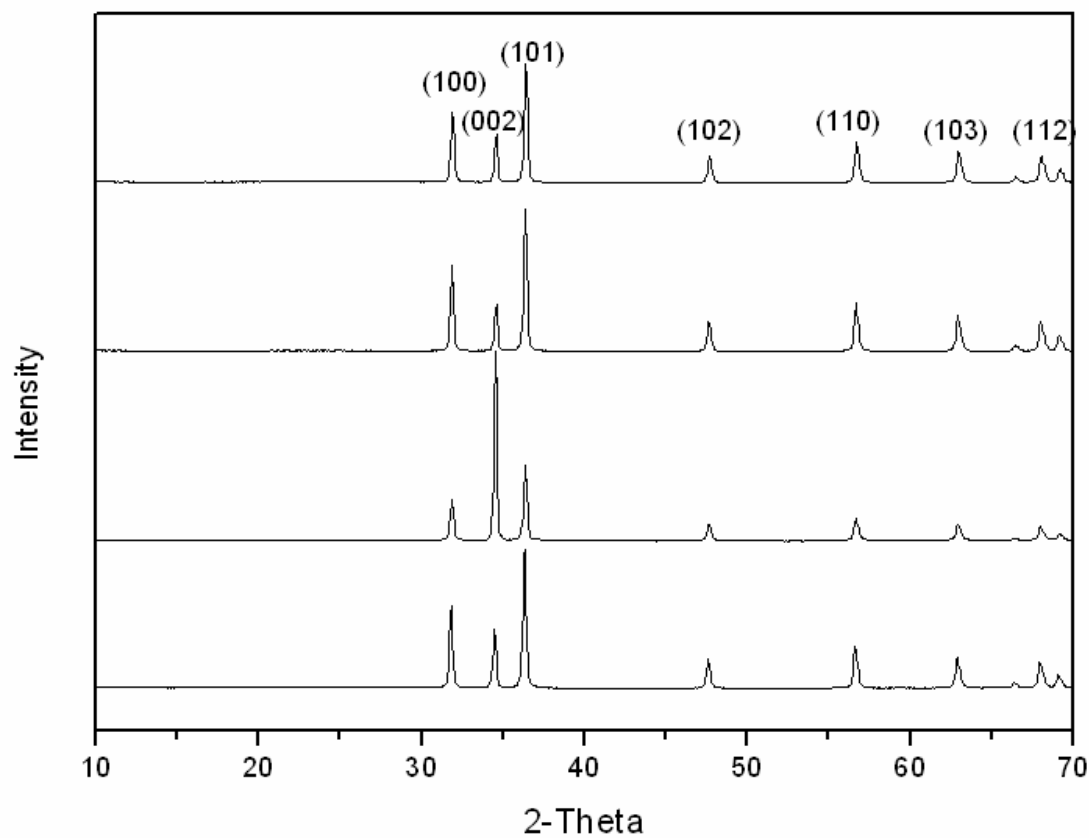


Fig.7.2.a X-ray diffraction patterns of ZnO nanoparticles, (b) randomly oriented ZnO nanorods, (c) aligned ZnO nanowires and (d) ZnO nanoparticles doping with 5%Al₂O₃

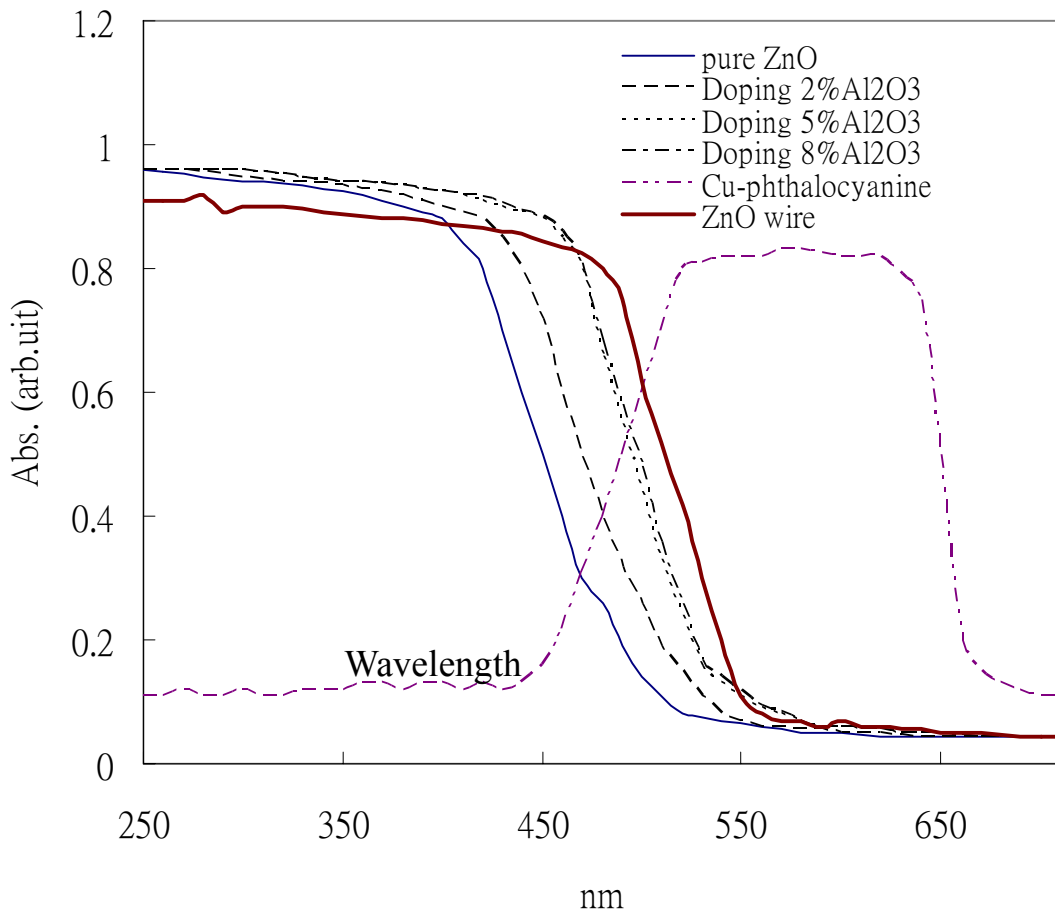
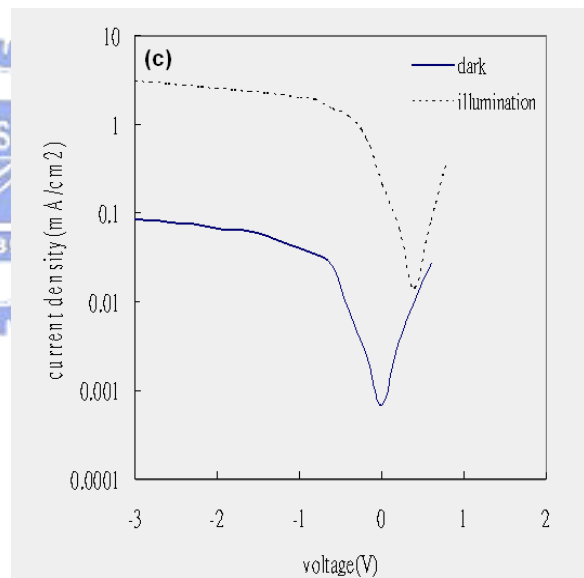
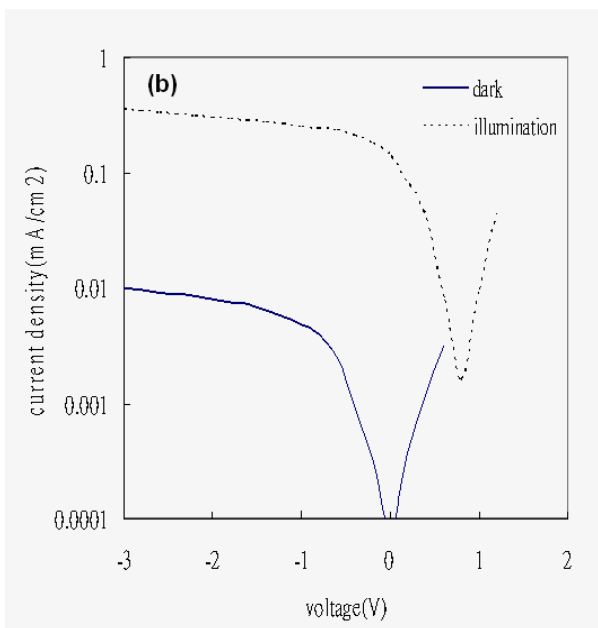
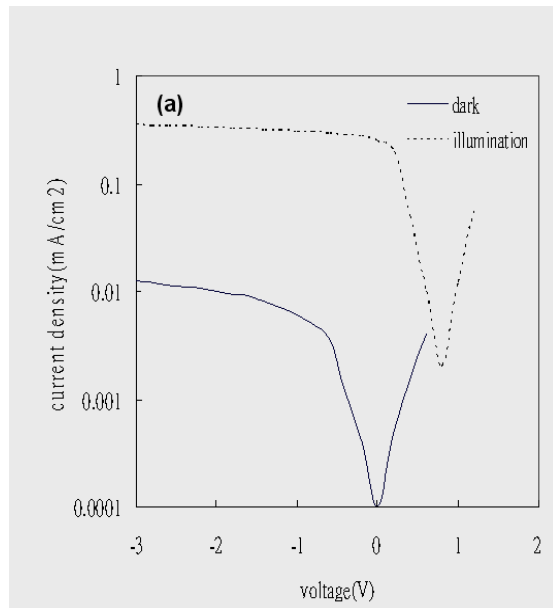


Fig.7.3 The absorption spectrum of pure ZnO, ZnO:Al, and Cu-phthalocyanine



ig.7.4 The current–voltage behavior of hybrid devices fabricated from 5%Al₂O₃–doped (a) ZnO nanoparticles (b) ZnO randomly oriented nanorods (c) vertically ZnO aligned nanorods in dark and illumination.

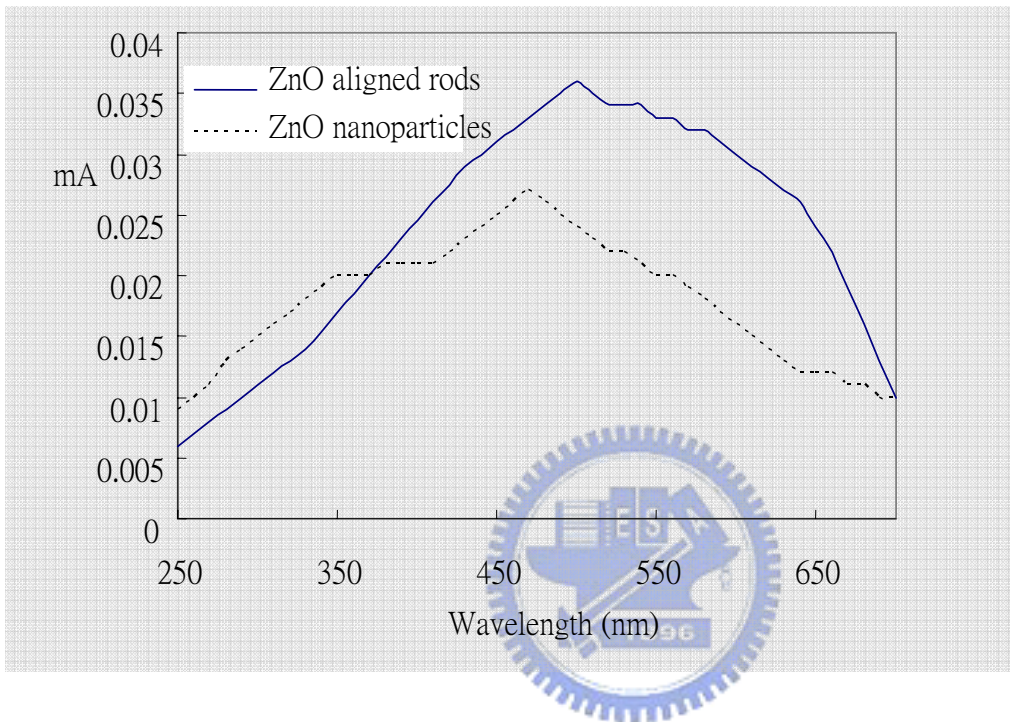


Fig.7.5 An photo to electron conversion of the hybrid devices with 5%Al₂O₃-doped ZnO with nanoparticles and vertically ZnO aligned nanorods.

Chapter 8

1and 2 Dimention Nano Structure Design and Giant-Grain Orientated Polysilicon Study at Low Temperature

8.1 Introduction

Solar cell is very potential and important green energy source because it combines the most clean and free source and will replace currently conventional energy such as oil, coal and nuclear in future. It is well know that TiO_2 p-n junction thin film on silicon wafer is typical structure of solar cell. However, shortage of silicon wafer in market causes total product of solar cell to increase slowly. In order to solve these problem, a new rout for prepared solar cell module have been researched by adopting low cost coated foreign substrate with polysilicon instead of silicon wafer.

A presently widely used method to fabricate polysilicon on foreign substrates is laser crystallization[8.1-8.5]. Laser crystallization is a much faster process than conventional process and can produce large grain size polysilicon with a low defect density [8.6]. The basic principle of laser crystallization is the transformation from amorphous to crystalline silicon by melting the silicon for a very short time. Giant grain polysilicon generated from the subsequent solidification. Laser crystallization of *a*-Si can be performed using a variety of lasers and different techniques [8.7-8.9]. Moreover, excimer laser crystallization is by far the most widely used method at the moment [8.10-8.11].

The excimer laser annealing process is executed very close to the irradiated surface due to the higher absorption coefficient in the UV region and the lower thermal conductivity of the amorphous materials. However, for generating uniform giant-grain crystalline and well orientated crystalline it is necessary to design some special microstructure and to know the melting threshold of the amorphous layer to be crystallized. In this study, a new structure is manufacturded by silicon layer coated glass substrate with thermal conducting layer and thermal isolation layer in order to create more order nucleation seeds. Meanwhile, the temperature gradient could be generated on the

silicon layer and cause the uniform polysilicon growth of 1~2 μ m giant grains and multiple laser fluence method have been executed to increase the crystalline orientation.

8.2 Experimental

The starting material for the crystallization experiments was hydrogenated amorphous silicon prepared by the decomposition of pure silane (SiH_4) with plasma enhanced chemical vapor deposition (PECVD). The samples used in this work were deposited on Corning 1737 glass substrates and photolithographic process is executed to pattern the thermal conducting metal Al layer and form many variable thermal conducting zone beneath silicon layer. Finally, SiO_2 layer was deposited upon silicon layer as a thermal isolation layer.

The laser annealing apparatus consists of a light pass system, homogenizer system, X-Y translation stage, and 50W pulse wave KrF excimer laser (Lambda Physik, LPX-305) operating at wavelength of 248nm and width of 23ns. Crystallization experiments were performed using single shot and multiple shots crystallization. The X-Y translation stage was adjusted depending on the frequency of the laser used in order to ensure an overlap between subsequent laser pulses.

Macro characterization of silicon layer was accomplished by X-ray diffraction (XRD, Philips1700). Surface image and mapping analysis were obtained from field emission scanning electron microscope (FESEM, LEO1530).

8.3 Results and Discussion

Fig.8-1 revealed the diagram of silicon coated glass structure. The important processes to manufacture the unique structure were expressed as follows: 1. Al electrical conducting layer was formed on the glass substrate. 2. Photolithographic process was executed to pattern the thermal conducting layer and form many variable thermal conducting zones. 3. An about 200nm

amorphous silicon film was formed on the patterned thermal conductive layer. 4. A thermal isolation layer such as SiO₂ was deposited for keeping laser annealing temperature. 5. While the pulse excimer laser was injected the structure, the amorphous silicon film could absorb laser energy instantaneously and transform it to crystalline type.

To prevent ablation a conventional furnace annealing was normally performed prior to the laser crystallization. To remove the hydrogen from the starting material the temperature during the annealing had to be 400 - 500°C. About four hours were needed to remove the hydrogen from amorphous Si:H with a film thickness of 200 nm. Moreover, because laser beam could penetrate the thin SiO₂ film and directly heat amorphous silicon, SiO₂ layer could be deposited on silicon layer as a thermal isolation layer for keeping laser annealing temperature.

While laser source of variable energy irradiate the surface of samples, the silicon layer could appear three distinguishable microstructures. Fig.8-2-1,8-2-2, 8-2-3 and 8-2-4 show crystallized silicon microstructures under 300,450,475and 500mJ/cm² laser fluence, respectively. In both high (500 mJ/cm²) and low(300mJ/cm²) laser fluence, there were very much fine recrystalline appeared, but 2µm giant recrystallized grain could be obtained under suitable medial(450 mJ/cm²) laser fluence. To explain the account, because 300mJ/cm² laser fluence just exceeded the critical energy of recrystalline and laser influence could not completely melt the amorphous silicon thin film, it caused the coexistence of solid phase and liquid phase and generated heterogeneous nucleation on boundary. Because abundant seeds appeared, growing grains were limited at horizontal space and, instead, rapidly crystallize at vertical direction. Nano size crystal formed at this process and their size was smaller than the silicon film. Under 500mJ/cm² laser fluence, silicon layer could completely melt total silicon film, then liquid silicon rapidly supercooling and homogeneously recrystallizing, the interface between liquid silicon and glass generated heterogeneous nucleation seeds and recrystallized as super fine grains. Under suitable laser fluence(450~475mJ/cm²), silicon layer would generate nearly completely melting. This could induce lateral giant grain,

because suitable laser fluence make silicon layer form abundant separable nucleation seeds that were generated by patterned thermal conducting zone under the silicon layer.

Fig.8-3 shows relationship between crystallized grain size and laser fluence. The grain gradually enlarged from 350 mJ/cm² to 450 mJ/cm² and the peak value of grain size appeared at 450~475 mJ/cm². While laser fluence >475 mJ/cm², crystallized grain size abruptly decreased.

Fig.8-4 shows the XRD pattern before and after laser annealing process. Original silicon layer belonged to amorphous type according to its boarding pattern. After laser annealing process, it appeared three peaks between 20° and 60° diffraction angle and diffraction crystal face included (111),(220) and (311). During laser annealing, thin film melted then recrystallized and thin film structure transformed to more stable condition. Si(111) growing along surface panel was the most stable, so usually Si(111) had stronger peak intensity than other peaks.

Fig.8-5 reveal Si(111) and (200) peak intensity and 475 mJ/cm² situation could obtain strongest peak intensity. It could be explained that complete recrystallization happen at 475 mJ/cm² and there was only partial recrystallization at 450 mJ/cm² in spite of their similar grain structure. More cracks and defects could be observed in microstructure of 475 mJ/cm² situation and it cause crystalline problem. Table 8-1(a) show the XRD intensity ratio of (111)/(200). The ratio of every laser fluence situation is between 2.11 to 3.07.

Although single laser fluence could achieve giant grain polysilicon, amorphous and nanosize grains existed in boundaries or other microstructures. Multiple laser fluence process have been executed to increase the crystalline of silicon layer. Fig. 8-6 shows the XRD result of multiple laser irradiating samples that assemble medial(one shot) and low (ten shots) laser fluence. The sample to assemble 475mJ/cm² one shot and 350mJ/cm² ten shots, 475(1)-350(10), could obtain weaker (220) peak, therefore, it could be deduced that the (220) orientation grains have been efficiently combined into (111) orientation giant grains. Table 8-1(b) shows the XRD intensity ratio of (111)/(200) of multiple laser fluence process. The ratio of 475(1)-350(10) sample could reach

7.75 that also disclosed high orientation (111) polysilicon formed.

8.4 Summary

A new structure was manufactured by silicon coated glass substrate with thermal isolation layer and thermal conducting layer that are patterned under the silicon layer to enhance the lateral giant grain growth. Meanwhile, laser annealing was used as the unique method to melt primal amorphous silicon thin film and promote it recrystallize under $300\text{-}500\text{mJ/cm}^2$ laser handling. By multiple laser fluence method, the temperature gradient could be generated on the silicon layer and caused the uniform $1\text{-}2\mu\text{m}$ polysilicon to grow and at the same time giant grains appeared and the crystalline orientation increased.



8.5 Reference

- [8.1] Yoo JH, Jeong SH, Mao XL, Greif R, Russo RE.. Appl Phys Lett 2000;76(6):783–5.
- [8.2] Pedraza AJ, Fowlkes JD, Jesse S, Mao C, Lowndes DH. App Surf Sci 2000;168: 251–7.
- [8.3] Mariucci L, Pecora A, Carluccio R, Fortunato G. Thin Solid Films 2001;383:39–44.
- [8.4] Trtica MS, Gakovic BM. Appl Surf Sci 2003;205(1):336–42.
- [8.5] C. Ossadnik, S. Veprek, I. Gregora, Thin Solid Films 337 (1999) 148.
- [8.6] J. B. Boyce, P. Mei, R. T. Fulks, and J. Ho, phys. stat. sol. (a) 166, 729 (1998).
- [8.7] G. Andrä, J. Bergmann, F. Falk, and E. Ose, Thin Solid Films 318, 42 (1998).
- [8.8] C. E. Nebel, S. Christiansen, H. P. Strunk, B. Dahlheimer, U. Karrer, and M. Stutzmann, phys. stat. sol. (a) 166, 667 (1998).
- [8.9] J. R. Köhler, R. Dassow, R. B. Bergmann, J. Krinke, H. P. Strunk, and J. H. Werner, Thin Solid Films 337, 129 (1999).
- [8.10] J. S. Im, M. A. Crowder, R. S. Sposili, J. P. Leonard, H. J. Kim, J. H. Yoon, V. V. Gupta, H. J. Song, and H. S. Cho, phys. stat. sol. (a) 166, 603 (1998).
- [8.11] M. Matsumura, phys. stat. sol. (a) 166, 715 (1998).

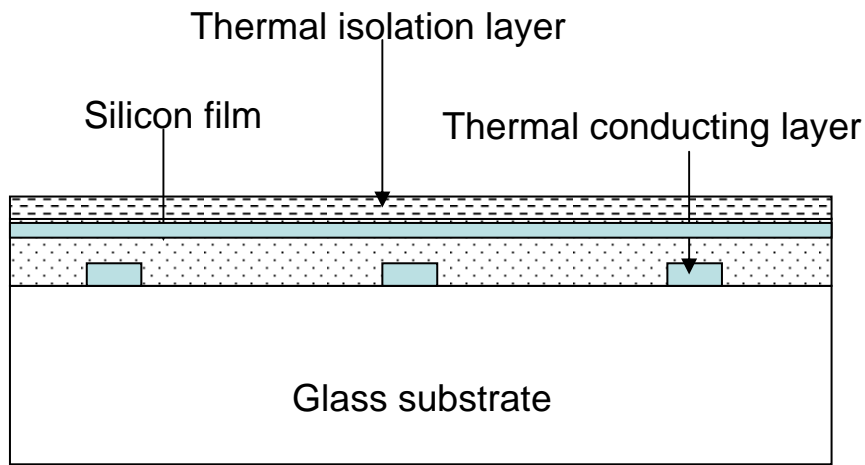


Fig. 8-1 A new structure was manufactured by silicon layer coated glass substrate with thermal conducting layer and thermal isolation layer.



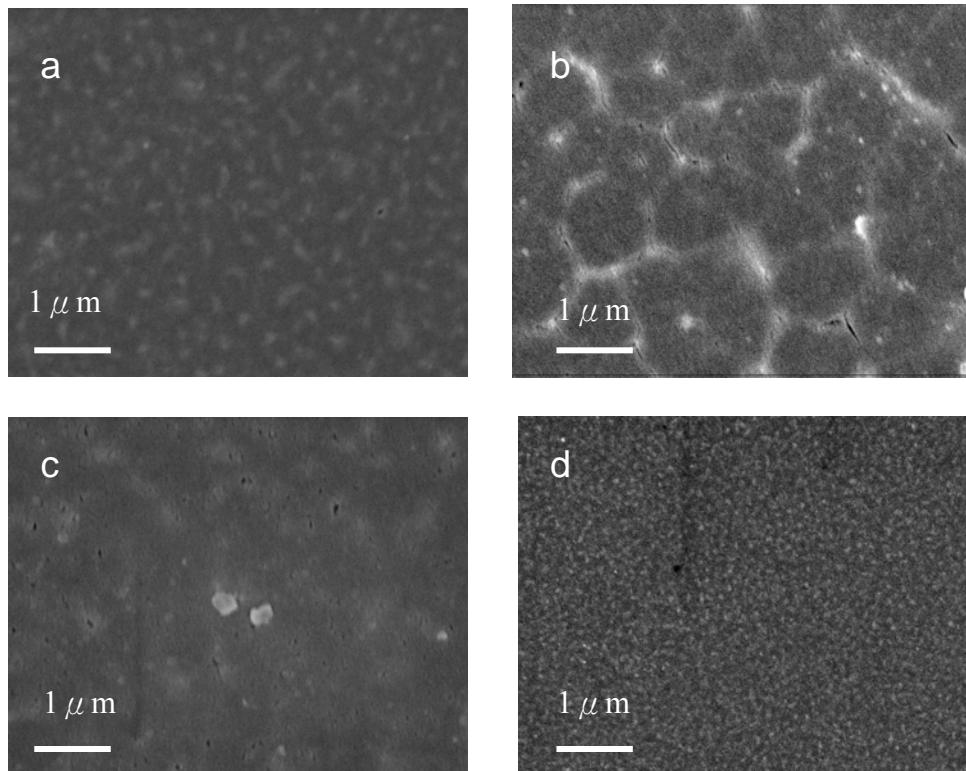


Fig. 8-2 SEM image of silicon film laser crystallized under (a) $300\text{mJ}/\text{cm}^2$ (b) $450\text{mJ}/\text{cm}^2$ (c) $470\text{mJ}/\text{cm}^2$ (d) $500\text{mJ}/\text{cm}^2$.



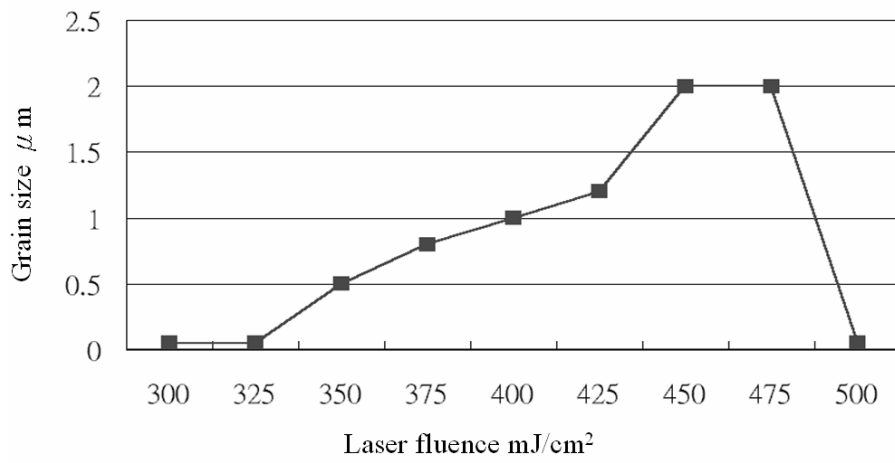


Fig. 8-3 The relative curve between crystallized grain size and laser fluence.



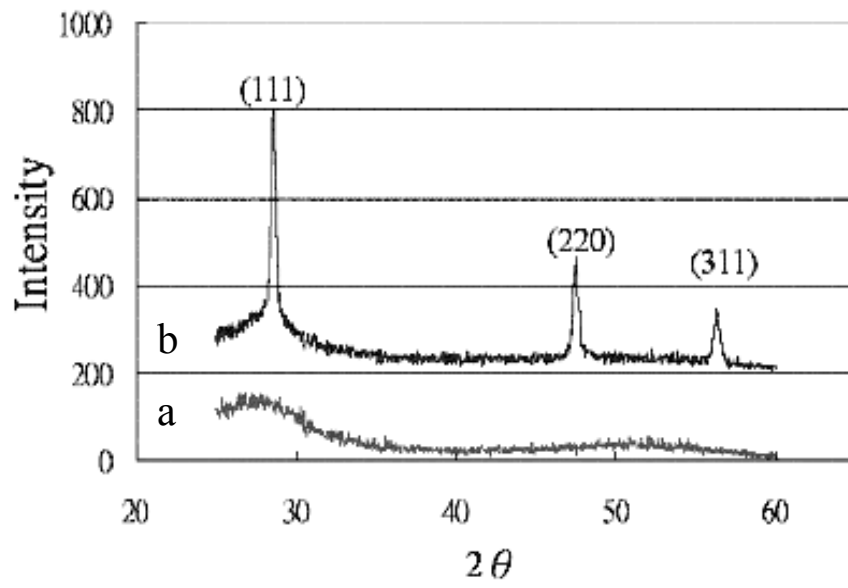


Fig.8- 4 XRD pattern of amorphous silicon thin film(a) before laser annealing and (b) after laser annealing



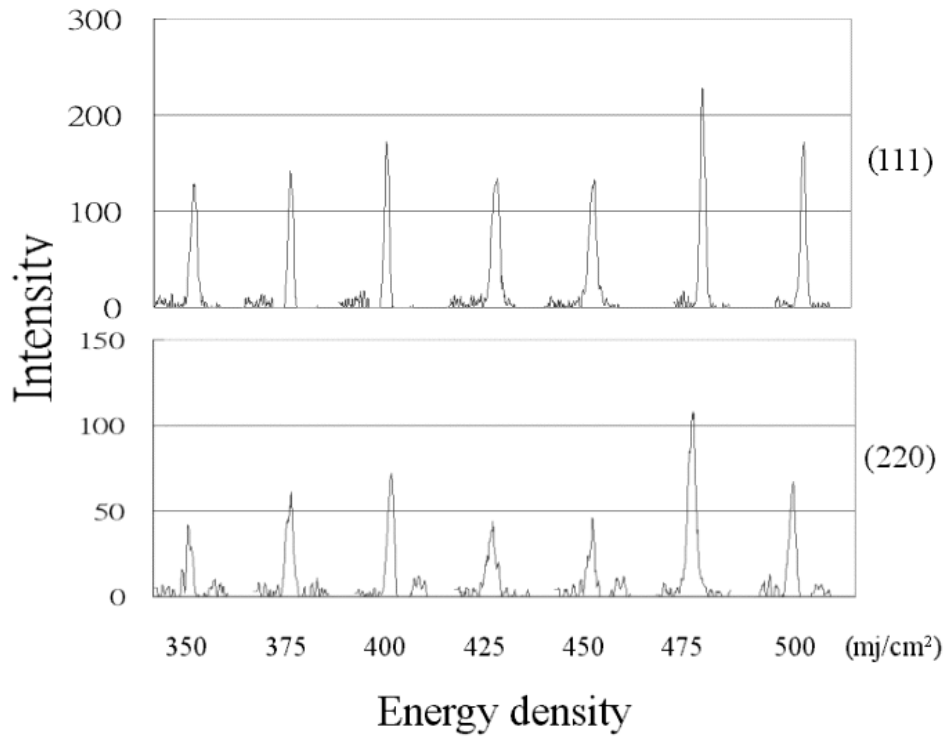


Fig.8-5 XRD peak of Si(111) and Si(220) after different fluence laser irradiating



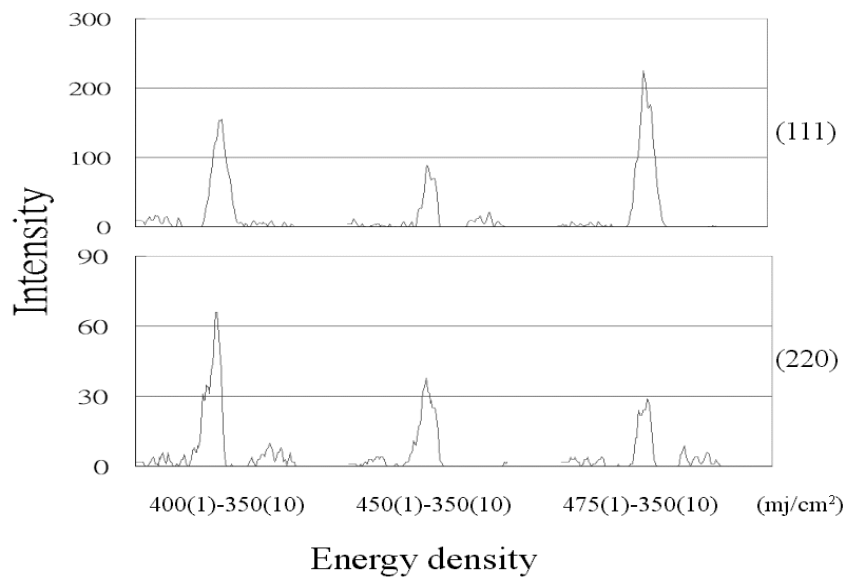


Fig.8-6 XRD peak of Si(111) and Si(220) after multiple fluence laser irradiating



(a)

Energy density	350	375	400	425	450	475	500
(111)intensity	129	142	173	134	133	228	172
(220)intensity	42	61	72	44	46	108	67
ratio (111)/(220)	3.07	2.33	2.40	2.95	2.89	2.11	2.57

(b)

Energy density	400(1)-350(10)	450(1)-350(10)	475(1)-350(10)
(111)intensity	155	89	225
(220)intensity	66	38	29
ratio (111)/(220)	2.35	2.34	7.75

Table 8-1 XRD intensity ratio of Si(111)/Si(200) of (a) single laser fluence and (b) multiple laser fluence process



Chapter 9

Conclusion

1. Laser ablation is an important and useful method for oxide nanoparticles with single or multiphase. Surface of target will be annealed by laser power and presents nearly constant ablation rate after several shots. Higher laser power creates larger particle with good crystallization, while lower ones gives fine and amorphous particles. Multiphase target suffers from phase separation due to the different laser absorption ability. Modification of target composition may relieve this problem.
2. A highly dispersed nano-TiO₂/Ag catalyst is synthesized in an alkaline solution. Nearly all of the dimethyl-blue target pollutant at high concentration was removed when the photoreaction was performed in a short period. This novel nano TiO₂ photocatalyst exhibits excellent photocatalytic activity because it is well dispersed. Since no dispersant or organic binder was used, this synthetic process has the advantages of low cost and convenience.
3. Electroless deposition with Au catalyst can be applied to fabricate Ni-P magnetic nanotube arrays by controlling electrolytic bath at 90 °C and pH=4.5~6. The studies indicate that the highly ordered array nanotubes are amorphous structure with the average diameter of 200~300 nm and length of 2 μm and form a highly ordered array. The hysteresis loop of the array nanotubes shows magnetic anisotropy with the easily magnetized direction perpendicular to the nanotubes axis.
4. A two-stage process including AAO process and electrodeposition was applied to fabricate the ordered silver- nickel core-shell nanowire arrays. Transmission electron microscopy (TEM) observation reveals that a 15 nm thick nickel film was coated on the surface of the silver nanowires with about 200 nm in diameter. The magnetic properties of silver nanowires with nickel coated can be much enhanced compared to that of pure silver one. The Magnetic Force Microscope (MFM) image of silver- nickel core-shell nanowires exhibits magnetic domain state. The hysteresis loop of the array exhibited strong magnetic anisotropy with the easily magnetized

direction perpendicular to the core-shell nanowires axis.

5. Comparing with electrochemical experiments and analysis, we successfully worked out the optimized conditions to synthesize Ag/Co multi-layer nanowires, 100nm diameter, respectively by a single-bath electrodeposition using the AAO template. The segment composition of the nanowires was [Co]/ [Ag₈₀Co₂₀] that is not stable and homogeneous all through the whole nanowire. By annealing process, we could attain better results of almost pure Co/Ag nanowires Co_{99.57}/Ag₁₀₀ which shows different magnetic properties such as more obvious anisotropy and change of easy axis compared with those of pure Co nanowires.
6. The heterojunction photovoltaic devices comprising hybrid p-type organic Cu-phthalocyanine and inorganic vertically aligned ZnO nanorods of n-type semiconductor were fabricated. The strong absorption of ZnO layer appears in range 250~460nm wavelength. Meanwhile, Cu-phthalocyanine exhibits broad absorption behavior of 440-700nm having an absorption maximum at 630nm. Charge recombination in vertically aligned ZnO rods type was more efficient than the conventional randomly oriented rods and nanoparticles. The maximum value of incident photon to electron conversion in aligned ZnO is 0.036mA and lie at around 500 nm and energy conversion efficiencies under simulated sunlight AM1.5 (10mW/cm²) of 1.32%.
7. A new 1 and 2 dimension nano structure for making solar cell or TFT module have been researched by adopting low cost coated glass substrate with polysilicon instead of silicon wafer. Meanwhile, laser annealing is used as the unique method to melt primal amorphous silicon thin film and promote it recrystallize under low temperature. Particularly, the new thermal conducting layers are patterned under the silicon layer to enhance the lateral giant grain growth. The important processes are represented as follows: 1. A electrical conducting layer are formed on the glass substrate. 2. Photolithographic process is executed to pattern the thermal conducting layer and form many variable thermal conducting zone. 3. An about 200nm amorphous silicon film is formed on the patterned thermal conductive layer. 4. A thermal isolation layer such as SiO₂ is deposited for keeping laser annealing temperature. 5. While the pulse excimer laser is

injected the structure, the amorphous silicon film can absorb laser energy instantaneously and transform it to crystalline type. Moreover, the temperature gradient could be generated on the silicon layer and cause the uniform polysilicon growth of 1~2 μm giant grains under about 450-475 mJ/cm^2 laser fluence. A unique method of multiple laser fluence have been executed to increase the crystalline orientation of Si(111)



Publication list

1. Shih-chin Lin, Sanyuan Chen, Suhyuh. Cheng, Jenchieh Lin. Synthesis and magnetic properties of highly arrayed nickel-phosphate nanotubes. *Solid State Sciences*, Volume 7, Issue 7, 1 July 2005, Pages 896-900
2. Shih-Chin Lin, San-Yuan Chen and Syh-Yuh Cheng Characterization and composition evolution of multiple-phase nanoscaled ceramic powders produced by laser ablation. *Powder Technology*, 2004, Volum 148, Numero 1, October, Pages 28-31
3. Shih-chin Lin, San-Yuan Chen, Yun-Tien Chen, Syh-Yuh Cheng. Electrochemical fabrication and magnetic study of highly ordered silver-nickel core-shell nanowires, *Alloy and Compound*, In press)
4. Yun-Tien Chen, Shih-chin Lin, Syh-Yuh Cheng. Temperature dependence on dielectric and piezoelectric properties of PLZT-PZN ceramic tapes. *Alloy and Compound*, In press)
5. Shih-Chin Lin, San-Yuan Chen and Syh-Yuh Cheng, Solar cell devices based on Cu-phthalocyanine / nanostructured ZnO hybrid film, *International Conference of Nanoscience and Technology 2007*
6. Chia-Hsin Lin, Yu-Chih Lin, Chung-Liang Chang, Wen-Chin Chen, Syh-Yuh Cheng, Yi-Hui Wang, Shih-Chin Lin, Shang-Hsiu Lee, Photodecomposition of Methylene-blue by Highly-dispersed Nano TiO₂/Ag Catalyst. *React. Kinet. Catal.Lett.* Vol. 90, No. 2, 267–273 ,2007
7. Shih-chin Lin, San-Yuan Chen, Yun-Tien Chen. Study of Giant-Grain Polysilicon at Low Temperature. *International Conference on Inorganic Materials*, 2006
8. Shih-Chin Lin, Yun-Tien Chen, Syh-Yuh Cheng and Shih-Cheng Lin (2001) Fabrication and Characterization of Silver Coated Nickel Powders, *5th Nano Engineering and Micro System Technology Workshop Proceeding*, P3-67~72
9. Shih-Chin Lin, Yun-Tien Chen, Syh-Yuh Cheng (2001) Structure, Characterization, and Reliability of Thick Film Capacitors Embedded in the Low Temperature Cofired Ceramics. *VLSI*

Multilevel Interconnection Conference 2001 Proceeding, P269~272

10.Houng-Yi Yang, Shih-Chin Lin and Yu-Ting Lin (1997) The Occurrence of Pseudobrookites and Other Minerals in Cavities of Strongly-Oxidized Andesites from The Coastal Range of Eastern Taiwan, Journal of The Geological Society of China, Vol.40, No.4. P.709-722

